FINITE STRAIN CONSTITUTIVE MODELING OF SHAPE MEMORY ALLOYS INCORPORATING TRANSFORMATION-INDUCED PLASTICITY UNDER CYCLIC LOADING

A Dissertation

by

LEI XU

Submitted to the Office of Graduate and Professional Studies of
Texas A&M University
in partial fulfillment of the requirements for the degree of

DOCTOR OF PHILISOPHY

Chair of Committee,	Dimitris Lagoudas
Committee Members,	Raymundo Arroyave
	Theocharis Baxevanis
	James Boyd
	Alan Freed
	Darren Hartl
Head of Department,	Rodney Bowersox

December 2019

Major Subject: Aerospace Engineering

ABSTRACT

Shape Memory Alloys (SMAs), as a subgroup of active materials, provide remarkable advantages working as solid-state actuators in terms of the trade-offs between structure overall weight and functionality, thus gaining tremendous application interests in various industries such as biomedical, aerospace, and civil engineering. However, the majority of constitutive models for SMAs are developed based on small strain theory which are inaccurate in the case of large deformations. Besides, applications involved with cyclic loading require SMAs experiencing repeated phase transformations, during which permanent deformations are developed due to transformation-induced plasticity (TRIP) at an effective stress level much lower than the material yielding point. Moreover, realistic applications also need SMA-based actuators subjected to multiaxial stress state originated from geometry complexities or installment required discontinuities such as notches and holes, where the non-uniform stress field has shown to have a significant impact on the multiaxial TRIP evolution during thermomechanical loading cycles. To meet the above modeling challenges, this work aims to address the following objectives. First, a three-dimensional finite strain constitutive model is proposed for polycrystalline SMAs to account for the large deformations (including large strains and rotations) that SMA components may undertake. Furthermore, the model is extended to incorporate the multiaxial TRIP evolution under non-uniform stress fields. A detailed implementation of the proposed model is presented through a user-defined material subroutine within a numerical environment for solving different bound value problems. Finally, the predicted cyclic pseudoelastic and actuation responses for a wide range of SMA material systems under both uniaxial and multiaxial loading conditions are compared against experimental results to validate the proposed modeling capabilities.

DEDICATION

To my parents, my brother,

and my wife.

ACKNOWLEDGMENTS

Time flies within just the blink of eyes, and now, it approaches the finishing point of my journey as a doctoral student. As the completion of this dissertation constitutes not only the work from myself but also numerous discussions, helps and guidance of many other individuals, I would like to utilize this opportunity to thank all those who have contributed to the accomplishment of it.

There is an old Confucius saying: *Where there are three people walking together, you can always find teachers among them, and learn some good lessons*. Those wisdom words can't be more demonstrated during my life experience as a graduate research assistant at Texas A&M University. First and foremost, I feel very grateful to Dr. Dimitris Lagoudas for providing me the opportunity to work with him, enriching me a classic "Aristotle" philosophy towards research, being critical about granted things. I have benefited tremendously from his high standards of excellence through many of the most fundamental and critical questions during our research interactions. I have also benefited excessively from his experience on how to present research through a succinct yet still scientific and consistent manner. I am also certain that his charisma as a successful administrator would also be a role model for me during my following career path.

I would also like to thank Dr. Theocharis Baxevanis for providing his invaluable knowledge and patience throughout my entire studies as a graduate student. Before Theo left A&M for Houston as a professor, he was technically my direct mentor with whom I had a lot of discussions while I was fresh about shape memory alloys. He was the one who initially inspired me to pick this tough yet rewarding research topic. I still remember we spent multiple afternoons in his office on research discussions and deriving equations. Needless to say, he contributed an indispensable part to the completion of this dissertation.

Over those periods, I appreciated his honesty as a helpful mentor when we have different opinions, at the same time, as a friend I also enjoyed those casual moments that he tried to correct my English pronunciation using a strong Greek accent.

I also wish to express great appreciation to all the mentors and teachers who served as part of the committee, Prof. Alan Freed, Prof. James Boyd, Prof. Raymundo Arroyave, and Prof. Darren Hartl. All of them have shown me how to become patient teachers, excellent researchers, and leading investigators. I want to thank Dr. Ibrahim Karaman, Dr. Rob Wheeler, Dr. Kadri Can Atli, and Mr. Glen Bigelow from NASA Glenn Research Center for providing me invaluable experimental data. I also owe a lot of thanks to Dr. Alex Solomou who helped me quite a lot when I struggled with implementation convergence issues, and all the group mates who shared every moment as a SMARTAN over these years. In addition, I feel very grateful to Jian He, Yuxiang Lin, Yijun Chen, Chao Fang, Minjie Lu, and Jianfeng Wen who greatly enriched my life as genuine friends.

From a personal perspective, I want to give my sincere gratitude to my parents and my brother for their endless, unconditional care and support, without which I, as a youth, would never have the courage and confidence to explore so many uncertainties to reach where I am. Being a beloved son and a naughty brother are considered the luckiest things in my growing up. It is such a harmonious environment created by them that protects and waters me to blossom, instills me the spirits of modesty, compassion, perseverance, ambition, and enthusiasm that enable me to gain a wide-ranging perception of the world. No words in my mind can express my utmost thanks and appreciation for them. And of course, I owe a debt of gratitude to my wife Chen. No matter it is happiness or suffering, she stood by my side from the very beginning when we were in our country of origin, until this very important moment on the other side of the Pacific ocean. She has been a fantastic life partner I couldn't ask for more and deserves to share every bit of achievement I have and will have.

Finally, I would also like to acknowledge the funding agencies for providing financial support for my research during my doctoral studies and all the accommodations during international conferences and workshops. The accomplishment of this dissertation was financially supported by the Qatar National Research Fund (QNRF) under grant number: NPRP 7-032-2-016, and the National Aeronautics and Space Administration (NASA) through University Leadership Initiative (ULI) project under grant number: NNX17AJ96A. I also greatly appreciate the financial support from NSF for the International Institute of Materials for Energy Conversion (IIMEC) Summer School that I participated in during July 2018 at Thessaloniki, Greece.

CONTRIBUTORS AND FUNDING SOURCES

Contributors

This work was supported by a dissertation committee consisting of Professor Dimitris Lagoudas (chair) from the Department of Aerospace Engineering, Professor Theocharis Baxevanis from the Department of Mechanical Engineering, University of Houston, Professor James Boyd and Professor Darren Hartl from the Department of Aerospace Engineering, Professor Alan Freed from the the Department of Mechanical Engineering, Professor Raymundo Arroyave form the Department of Material Science and Engineering. All other work conducted for the dissertation was completed by the student independently.

Funding Sources

The author would like to acknowledge the financial support provided by the Qatar National Research Fund (QNRF) under grant number: NPRP 7-032-2-016, and the National Aeronautics and Space Administration (NASA) through the University Leadership Initiative (ULI) project under the grant number: NNX17AJ96A. The conclusions in this work are solely made by the author and do not necessarily represent the perspectives of QNRF and NASA.

NOMENCLATURE

$\mathcal{C}$	Effective forth-order stiffness tensor
$\mathcal{D}$	Dissipation energy
$\mathcal{S}$	Effective forth-order compliance tensor
$\mathcal{S}^A$	Forth-order compliance tensor of austenite
$\mathcal{S}^M$	Forth-order compliance tensor of martensite
$\Delta\mathcal{S}$	Phase difference of compliance tensor
$\boldsymbol{\Upsilon}$	Internal state variables symbol
$\boldsymbol{\Lambda}$	Transformation direction tensor
$\boldsymbol{\Lambda}_{fwd}$	Forward transformation direction tensor
$\boldsymbol{\Lambda}_{rev}$	Reverse transformation direction tensor
$\boldsymbol{\Lambda}^{tp}$	TRIP strain direction tensor
$\boldsymbol{\Lambda}^{tp}_{fwd}$	Forward TRIP strain direction tensor
$\boldsymbol{\Lambda}^{tp}_{fwd}$	Reverse TRIP strain direction tensor
Φ	Transformation function
$\boldsymbol{\Omega}^{log}$	Logarithmic spin tensor
$\boldsymbol{\alpha}$	Effective thermal expansion tensor
$\boldsymbol{\alpha}^A$	Thermal expansion tensor for austenite ($\boldsymbol{\alpha}^M$ for martensite)
$\Delta\boldsymbol{\alpha}$	Phase difference of thermal expansion tensor
$\boldsymbol{\beta}$	Internal stress tensor
$\boldsymbol{\varepsilon}$	Infinitesimal strain

$\boldsymbol{\sigma}$	Cauchy stress
$\boldsymbol{\sigma}'$	Deviatoric part of Cauchy stress
$\boldsymbol{\sigma}_s$	Detwinning starting stress
$\boldsymbol{\sigma}_f$	Detwinning finishing stress
$\boldsymbol{\sigma}^{Ms}$	Foward transformation initiation stress
$\boldsymbol{\sigma}^{Mf}$	Foward transformation finishing stress
$\boldsymbol{\sigma}^{As}$	Reverse transformation initiation stress
$\boldsymbol{\sigma}^{Af}$	Reverse transformation finishing stress
$\bar{\boldsymbol{\sigma}}$	von Mises equivalent Cauchy stress
$\boldsymbol{\tau}$	Kirchhoff stress
$\bar{\boldsymbol{\tau}}$	von Mises equivalent Kirchhoff stress
$\boldsymbol{\tau}'$	Deviatoric part of Kirchhoff stress
$\boldsymbol{\tau}^{eff}$	Effective Kirchhoff stress
$\bar{\boldsymbol{\tau}}^{eff}$	von Mises equivalent effective Kirchhoff stress
$\mathbf{D}$	The rate of deformation tensor
$\mathbf{E}^{(m)}$	Lagrangian strain family
$\mathbf{E}^{(2)}$	Green-Lagrangian strain
$\mathbf{F}$	Deformation gradient
$\mathbf{H}$	Logarithmic strain of Lagrangian type
$\mathbf{L}$	Velocity gradient
$\mathbf{P}$	First Piola-Kirchhoff stress tensor
$\mathbf{R}$	Rotation tensor
$\mathbf{R}^{tr}$	Transformation strain residual

$\mathbf{R}^{tp}$	TRIP strain residual
$\mathbf{S}$	Second Piola-Kirchhoff stress tensor
$\mathbf{U}$	Right stretch tensor
$\mathbf{V}$	Left stretch tensor
$\mathbf{W}$	Spin tensor
$\boldsymbol{X}$	Position vector of material point at reference configuration
$\boldsymbol{b}$	Body force vector
$\mathbf{e}^{(m)}$	Eulerian strain family
$\mathbf{h}$	Logarithmic strain of Eulerian type
$\mathbf{h}^{e}$	Logarithmic elastic strain tensor
$\mathbf{h}^{tr}$	Logarithmic transformation strain
$\mathbf{h}^{tp}$	Logarithmic TRIP strain
$\boldsymbol{l}_1, \boldsymbol{l}_2, \boldsymbol{l}_3$	Lagrangian triads
$\boldsymbol{q}$	Heat flux vector
$\boldsymbol{q}_1, \boldsymbol{q}_2, \boldsymbol{q}_3$	Eulerian triads
$\boldsymbol{s}$	Deviatoric part of stress tensor
$\boldsymbol{t}$	Surface traction vector at deformed area
$\bar{\boldsymbol{t}}$	Surface traction vector at undeformed area
$\boldsymbol{u}$	Displacement vector
$\boldsymbol{v}$	Velocity vector
$\boldsymbol{x}$	Position vector of material point at current configuration
ζ^{d}	Accumulated detwinned martensitic volume fraction
λ_1	Internal stress evolution parameter

ξ	Martensitic volume fraction
ξ^d	Detwnnied martensitic volume fraction
π	Thermodynamic driving force
ρ	Body density at current configuration
ρ_0	Body density at reference configuration
σ_b	Internal stress evolution material parameter
ψ	Helmholtz free energy
A_s	Austenite transformation start temperature
A_f	Austenite transformation finish temperature
C_A	Stress influence coefficient for austenite transformation
C_M	Stress influence coefficient for martensite transformation
C_1^p	TRIP strain evolution parameter
C_2^p	TRIP strain evolution parameter
D	Smooth hardening function parameter
G	Gibbs free energy
H^{cur}	Current transformation strain
H^{max}	Maximum transformation strain
H_i^{max}	Initial value of H^{max} before the cyclic loading
H_f^{max}	Final value of H^{max} after the cyclic loading
H^{min}	Minimum transformation strain
J	Determinant of the deformation gradient
M_s	Martensite transformation start temperature
M_f	Martensite transformation finish temperature

T	Temperature
T_0	Temperature at reference point
Y	Critical thermodynamic driving force
Y_0	Reference thermodynamic driving force
a_1, a_2, a_3	Intermediate material parameters in hardening function
c	Specific heat
$f(\xi)$	Smooth hardening function
h	Enthalpy
k_t	Curve fitting parameter in H^{cur} curve
n_1, n_2, n_3, n_4	Smooth hardening parameters
p	Hydrostatic pressure
r	Heat supply per unit mass
s	Effective specific entropy
s_0	Specific entropy at reference state
Δs_0	Phase difference of specific entropy at reference state
u	Effective internal energy
u_0	Internal energy at reference state
Δu_0	Phase difference of internal energy at reference state

TABLE OF CONTENTS

Page

LIST OF FIGURES

FIGURE Page

LIST OF TABLES

TABLE Page

1. INTRODUCTION

1.1 Transformation characteristics and applications of SMAs

Shape memory alloys (SMA) belong to a subgroup of active or smart materials that are able to reversibly achieve their relatively large shape changes when subjected to specific thermomechanical loading conditions. The physical mechanism attributing to such unique property is through their solid-to-solid diffusionless phase transformation between the high-temperature, high-symmetry austenitic phase (cubic crystal structure) and the low-temperature, low-symmetry martensitic phase (which can be tetragonal, orthorhombic, or monoclinic crystal structure). For the majority of SMA material systems, such as Ni-, Cu- or Fe-based SMAs, a stress versus temperature chart like Figure 1.1 is often utilized as a phase diagram to differentiate the martensite and austenite phases. Specifically, SMAs under the low-temperature conditions can exist in two equilibrium forms, i.e., the self-accommodated (or twinned) state and oriented (or detwinned) state. At high temperature, SMAs usually exist in a cubic crystal structure phase of austenite. As the regions are separated by the detwinning start and finish stresses $\boldsymbol{\sigma}_s, \boldsymbol{\sigma}_f$ shown in the phase diagram. The self-accommodated martensite often presents at low stress levels and can transform into oriented martensite through a detwinning process induced by applying enough external mechanical load. In addition, the phase transformation between austenite and martensite phases can be triggered by either stress or temperature changes. By cooling without applying any stresses, SMAs experience a forward phase transformation from austenite to self-accommodated martensite. As the arrangement of martensitic variants is in a twinned manner, there is no perceivable macroscopic shape change observed during this process. Upon heating, SMAs experience a reverse transformation and transform from the self-accommodated martensitic phase back to the austenitic phase, and no

macroscopic shape change is perceived here neither. However, when the material, originally start with austenite, is cooled under a stress level greater than σ_f, SMAs experience a transition from austenitic phase to an oriented martensite phase, in which a macroscopic shape change is observed, and such changes can be recovered through the heating process to induce a reverse phase transformation.

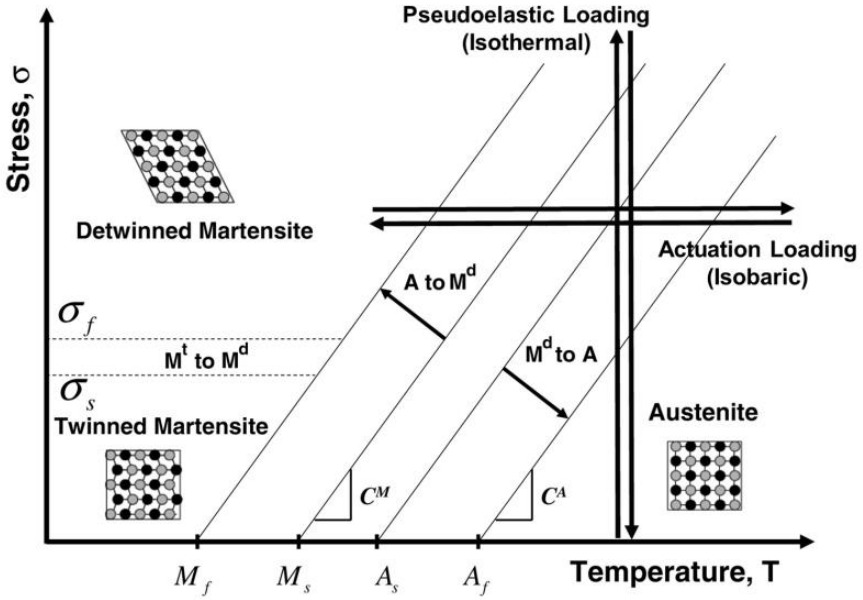

Figure 1.1: A typical stress versus temperature phase diagram of SMAs showing the low temperature martensitic phases (including detwinned/oriented and twinned/self-accommodated martensite) and the high temperature austenic phase, along with two representative loading paths, viz. the pseudoelastic and actuation loading path (from Figure 1.7 of [48], © 2008 Springer US, with permission of Springer US, DOI:10.1007/978-0-387-47685-8).

In general, two major thermomechanical loading paths are usually experienced by SMAs, viz., the pseudoelastic and actuation loading paths. In the case of pseudoelastic loading, the material, starting at high-temperature stable austenite phase, is subjected to

mechanical loading and unloading while the temperature is kept as a constant throughout the loading path. In the actuation loading case, the SMA material is subjected to heating and cooling process while the mechanical load is kept as constant. A schematic for the aforementioned two loading paths is illustrated in the phase diagram shown in Figure 1.1.

Refer to the phase diagram in Figure 1.2 to illustrate the transformation characteristics of the pseudoelastic response of SMAs. The pseudoelastic loading usually begins at a high temperature beyond A_f, which induces self-accommodated martensite as the stress level reaches the maximum point, and eventually reverts the material to the austenitic phase when the stress level returns to zero. There are four critical stress values during this pseudoelastic loading, i.e., $\boldsymbol{\sigma}^{Ms}, \boldsymbol{\sigma}^{Mf}, \boldsymbol{\sigma}^{As}, \boldsymbol{\sigma}^{Af}$, playing critical roles in dictating the pseudoelastic response features.

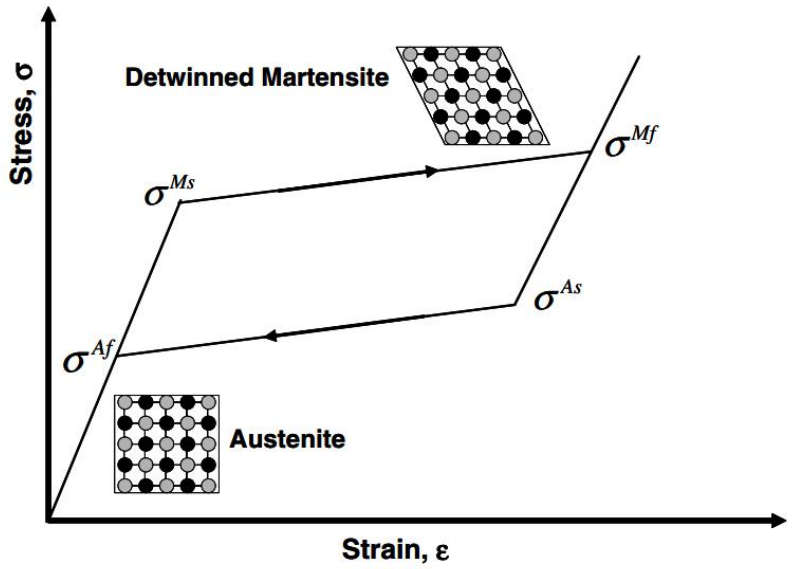

Figure 1.2: A representative pseudoelastic response of SMAs at a constant temperature corresponding to the pseudoelastic loading path in the phase diagram (from Figure 1.8 of [48], © 2008 Springer US, with permission of Springer US, DOI:10.1007/978-0-387-47685-8).

During the loading procedure, the starting austenite phase experiences elastic deformation when the external stress is employed. With the stress increasing to a certain point, the material state reaches a point for the initiation of martensitic transformation, which marks the forward transformation initiation stress level $\boldsymbol{\sigma}^{Ms}$. As the stress level proceeds to $\boldsymbol{\sigma}^{Mf}$, designated as the forward transformation finish stress level, a large amount of nonlinear transformation strain was generated during this forward transformation from austenite to martensite. After the loading path goes beyond $\boldsymbol{\sigma}^{Mf}$ which indicates the finish stress of the forward transformation, further stress increasing produces no further increase in transformation train and only the oriented martensite is further elastically deformed. During the unloading procedure, the stress-induced oriented martensite is first elastically unloaded. With further unloading, the material state meets a point for the initiation of reverse martensitic transformation from oriented martensite to austenite. The stress level then is marked as the reverse phase transformation starting point $\boldsymbol{\sigma}^{As}$. As the stress level further decreases to $\boldsymbol{\sigma}^{Af}$, designated as the reverse transformation finish stress level, the generated large transformation strain in the forward transformation is recovered during this reverse transformation procedure. Subsequent unloading beyond $\boldsymbol{\sigma}^{Af}$ only causes the austenite being elastically unloaded. The full pseudoelastic response accompanied by the forward and reverse phase transformations results in a closed hysteresis curve, by which the area surrounded represents the total dissipated energy in this phase transformation process. The transformation characteristics of pseudoelastic response for polycrystalline SMAs, including critical stress levels, the magnitude of transformation strain, and the size of hysteresis, are heavily dependent on the material's composition, manufacturing and aging process, and also the experiment testing conditions.

Apart from the stress-induced phase transformation, the thermal cycling of SMAs under specific stress level $\boldsymbol{\sigma}$ can also induce phase transformation. Recall that under zero stress state, SMAs transform from austenite into self-accommodated martensite upon

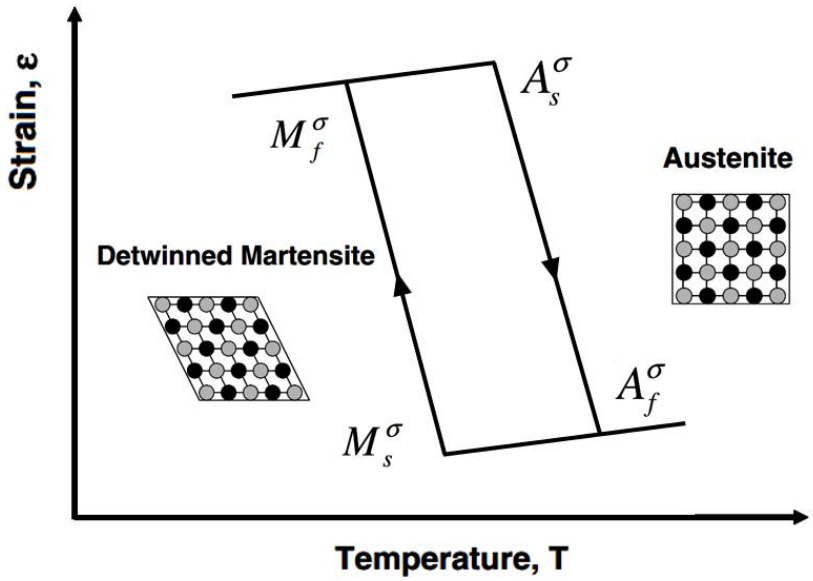

Figure 1.3: A representative actuation response of SMAs at a constant stress level corresponding to the actuation loading path in the phase diagram (from Figure 1.13 of [48], © 2008 Springer US, with permission of Springer US, DOI:10.1007/978-0-387-47685-8).

cooling and revert to austenite by reheating the self-accommodated martensite phase. Four critical temperatures associated with this process are (M_s, M_f, A_s, A_f), viz., the forward transformation start temperature, forward transformation finish temperature, reverse transformation start temperature and reverse transformation finish temperature. Those critical transformation temperatures are highly affected by the stress levels the material experienced, the larger the stress levels, the higher the transformation temperatures. Refer to Figure 1.3 for the schematic of a representative actuation response of SMAs under actuation loading with a constant stress level $\boldsymbol{\sigma}$. During the cooling step the temperature decreases from a high temperature to M_s^σ, the material in the austenite phase experiences a thermal contraction due to cooling. Further cooling the material from M_s^σ to M_f^σ induces a phase transformation from austenite to oriented martensite, during which a large

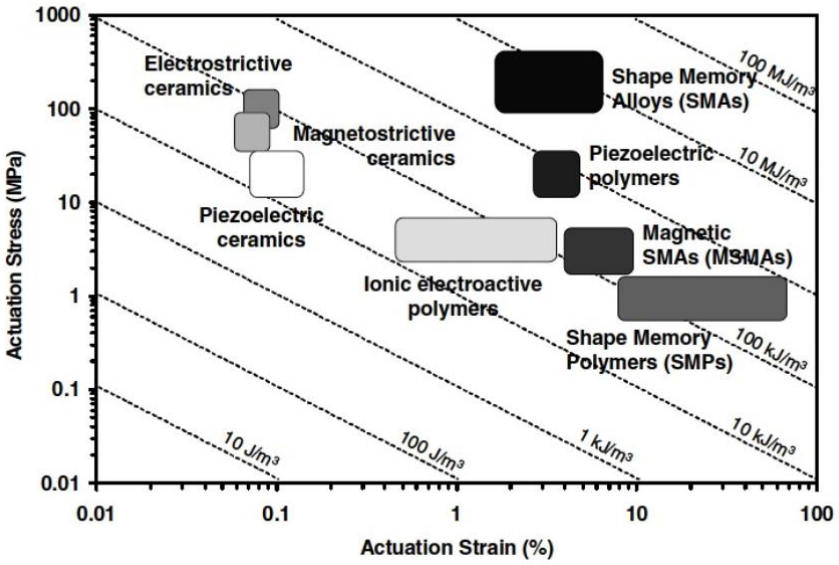

Figure 1.4: Actuation energy density chart showing the range of actuation stress, actuation strain and actuation energy densities for typical active materials including pizeoelectric ceramics, shape memory polymers, shape memory alloys, etc. wherein shape memory alloys show relatively large actuation energy density (from Figure 1.1 of [48], © 2008 Springer US, with permission of Springer US, DOI:10.1007/978-0-387-47685-8).

recoverable transformation strain is generated. A further temperature decreasing produces no further increase in transformation train and only causes an additional thermal contraction in the oriented martensite. When the material is reheated to A_s^σ, oriented martensite undergoes a thermal expansion upon heating. Further increasing the temperature to A_f^σ enables the oriented martensite transforming back to austenite, which results in the recovery of large transformation strain generated during the cooling stage. And subsequent temperature increasing beyond A_f^σ only results in additional thermal expansion in austenite. Similar to the pseudoelastic response of SMAs, the features of actuation response are also largely affected by composition, manufacturing and aging process, and its loading conditions.

Figure 1.5: Various SMA-based components in the forms of springs, beams and torque tubes that can be used as solid-state actuators.

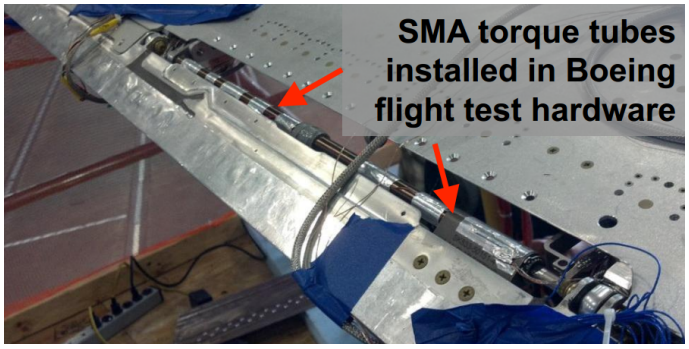

Figure 1.6: SMA-based torque tube components working as the torsional actuator installed on a Boeing 737 airplane to rotate the trailing edge flap during take-off and landing regime for a full-scale flight test, reprinted from [62].

As shown in Figure 1.4, because the high actuation energy density provided by SMAs compared to other active materials (such as shape memory polymers, piezoelectric ceram-

ics, and electroactive polymers), SMA-based functional components (usually in the forms of wires, springs, beams, and torque tubes shown in Figure 1.5) have been considerably investigated as actuators where a large amount of actuation stress and strain are required. Adaptive or morphing structures integrated with SMA-based actuators have tremendous advantages in terms of trade-offs between structure weight, integrity, and functionality. A considerable number of examples that SMA components are used as actuators can be found in various engineering industries. Take aerospace industry for instance, SMA-based torque tube components are used as torsional actuators installed on a Boeing 737 airplane, which are intended for rotating the trailing edge flap during take-off and landing regime for a full-scale flight test [62]. In the design of a deployment system for a solar panel used for microsats, a SMA-based torsional actuation system is utilized to replace the conventional electric motors, allowing for a deployable and retractable solar panel, which significantly reduces the microsats weight, volume, and complexity while providing the same needed functionality [108]. In the OPENAIR project [63], SMA wire actuators are used for the morphing chevron development to decrease the noise level of turbofan engines. Similar studies were conducted in the Boeing variable geometry chevron program, in which SMA beams were used as actuators to morph the shape of an engine outlet to reduce the noise during take-off and landing thereby to enhance the engine efficiency [31]. In the Smart Wing program via a collaboration between DARPA, AFRL, and Northrop Grumman, SMA wire actuators were used as tendons to actuate hinge-less ailerons, and SMA torque tube actuators were employed to achieve a span-wise wing twist for F-18 aircraft wing [46]. Recently, aerospace researchers have considered using the SMA-based actuators to reconfigure the shape of a supersonic aircraft to meet the noise and efficiency requirements in response to the real-time changing ambient environment, which has the great potential to realize a commercially viable overland civil supersonic flight in the near future [52].

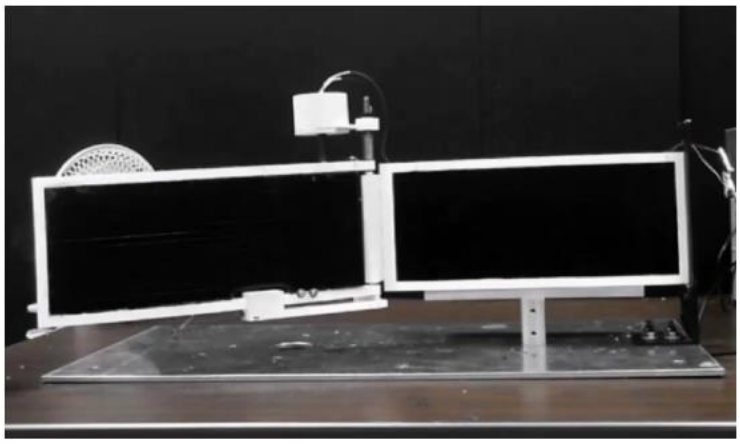

Figure 1.7: SMA-based torque tubes working as a rotational actuator for the solar panel in a small satellite, adapted from [108].

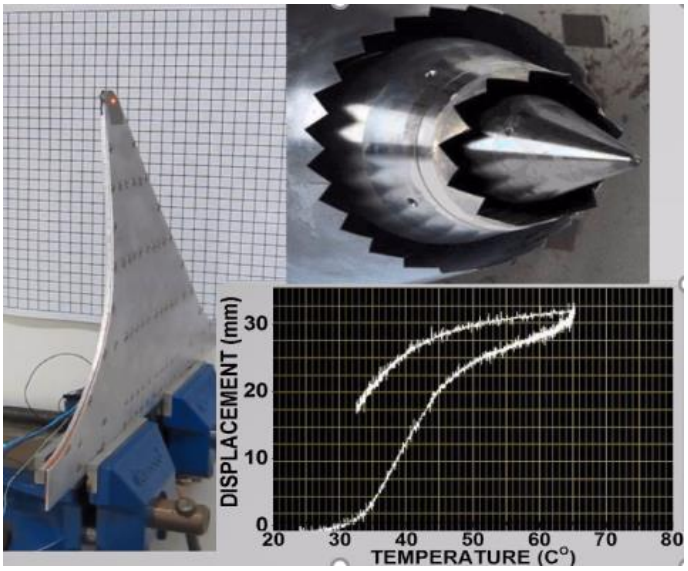

Figure 1.8: SMA wire actuators are used as a bending actuator to bend the panel to achieve a morphing chevron to decrease the noise level of turbofan engines in the OPENAIR project, adapted from [63].

1.2 Large deformations of SMAs

A lot of constitutive models have been proposed in the literature among which the majority of them are developed upon infinitesimal strain theory. These small deformation based models can be utilized as efficient modeling tools to predict SMA-based structure response accurately in the cases without large deformation. However, it has been reported that SMAs can reversibly deform to a relatively large strain regime up to 8% [89, 39]. Also for specific boundary value problems such as fracture in SMAs, the strain levels close to the crack tip are well beyond 10% [29, 28]. Under such large strains cases, it can be inaccurate to still use the infinitesimal strain models to predict SMA material response. Refer to the results shown in Figure 1.9 where the pseudoelastic response for an SMA bar is simulated by a logarithmic strain based finite strain model and its infinitesimal counterpart. When the maximum transformation strain reaches 10%, the difference between these predicted responses becomes predominant when the SMA bar approaching the end of the forward phase transformation. Specifically, a larger displacement value is predicted by the logarithmic strain based finite strain model. The cause for this displacement difference comes from the fact that infinitesimal strain neglects the higher-order terms in its strain measure while those terms are fully considered in the logarithmic strain based finite strain model. In addition to such relatively large strains, SMA-based actuators, in the forms of spring, beam and torque tube, undergoing large rotations have also been demonstrated in many engineering application situations. For instance, an SMA-based beam component is used as a bending actuator to morph the chevron geometry to realize an adaptive engine shape for desired flight aerodynamic conditions, in which the SMA-based beam experienced large bending-induced rotations [33]. Using an infinitesimal strain model in this case can predict an inaccurate structural response for the SMA-based actuators. Refer to the results shown in Figure 1.10 where the pseudoelastic response for an SMA beam is

provided. Although the two responses agree well in the initial stage, large discrepancy is developed as the SMA beam experiences large rotations afterward. The logarithmic strain based finite strain model predicts a much lager midpoint displacement value compared to its infinitesimal counterpart disregarding the large rotations. In the aforementioned SMA beams and torque tubes undertaking large strains and rotations, it is imperative to formulate a constitutive model based on the finite deformation framework to provide an accurate structural response of these structures. This is the first chosen objective to be addressed in this dissertation.

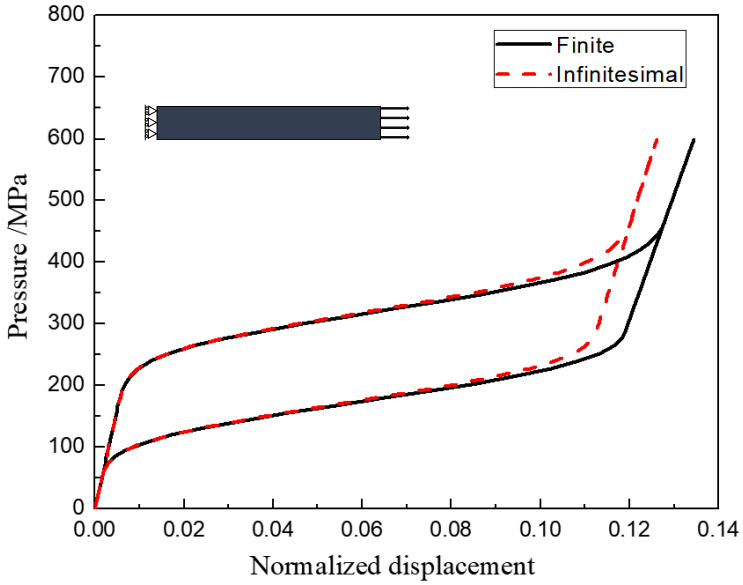

Figure 1.9: Comparison of pseudoelastic response for an SMA bar under tension predicted by a logarithmic strain based finite strain model and an infinitesimal strain model with transformation strain H^{max} = 10%, adapted from [118].

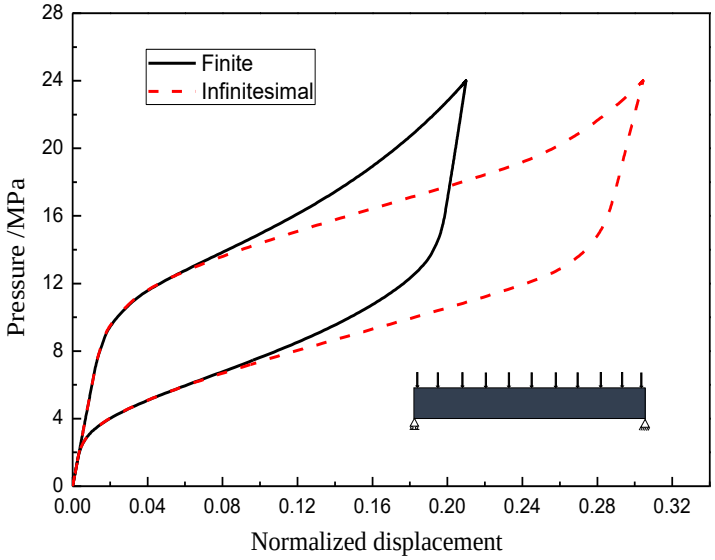

Figure 1.10: Comparison of pseudoelastic response for an SMA bending beam predicted by a logarithmic strain based finite strain model and an infinitesimal strain model with transformation strain H^{max} = 10%, adapted from [118].

1.3 Cyclic response of SMAs

The majority of engineering applications require SMAs experiencing a large number of loading cycles involving repeated phase transformations, which brings the increasing necessity to understand the material response of SMAs subjected to cyclic thermomechanical loading. Many experimental results [97, 98, 49, 50, 110] indicate that SMAs exhibit an evolving rather than stable material response under cyclic loading. More specifically, transformation characteristics of SMAs, e.g., the accumulation of irrecoverable strain, the size of stress/thermal hysteresis loop, the stress levels required to initiate the phase transformation, transformation temperatures, transformation strain magnitude, usually evolves from one cycle to another. Among those evolving characteristics, the irrecoverable strains are usually termed as transformation-induced plastic strain (TRIP), which are caused by the distortion as a result of the crystallographic misfit at the austenite-martensite inter-

faces and grain boundaries induced by the repeated phase transformation. This distortion results in an observable macroscopic plastic strain, which occurs at an effective stress level much lower than the conventional plastic yielding point [50]. Refer to the experimental results shown in Figure 1.11 for illustration, the 1^{st} and 50^{th} pseudoelastic loading cycle is plotted for a NiTi SMA wire subjected to 550 MPa mechanical loading at the isothermal condition. In the first mechanical cycling, the majority of strain generated during loading is recovered upon unloading with a small amount of them reserved at the end of the loading cycle. This small amount of irrecoverable strain keeps being generated during each consecutive mechanically cycling and accumulated throughout the entire loading cycles. A very similar evolving material response can be observed when an SMA is subjected to repeated thermal cycling. The major difference is that a more or less stable cycle is expected to be reached eventually in the pseudoelastic loading cycling (Figure. 1.12) while the TRIP strain evolves without a saturation limit is more closely aligned with actuation cycling (Figure. 1.14). In addition, the TRIP strain evolves with different rates throughout the entire material fatigue life state. It can be seen from the SMA fatigue test (Figure 1.14), the TRIP strain grows drastically during the very first hundreds of loading cycles then tends to increase in a stabilized trend until the material reaches the failing point at the very end. As the most of engineering applications require actuators functioning in stable material behavior, SMAs are usually subjected to a training process, i.e., repeated thermal/stress cycling, to stabilize their behaviors before being used as actuation components.

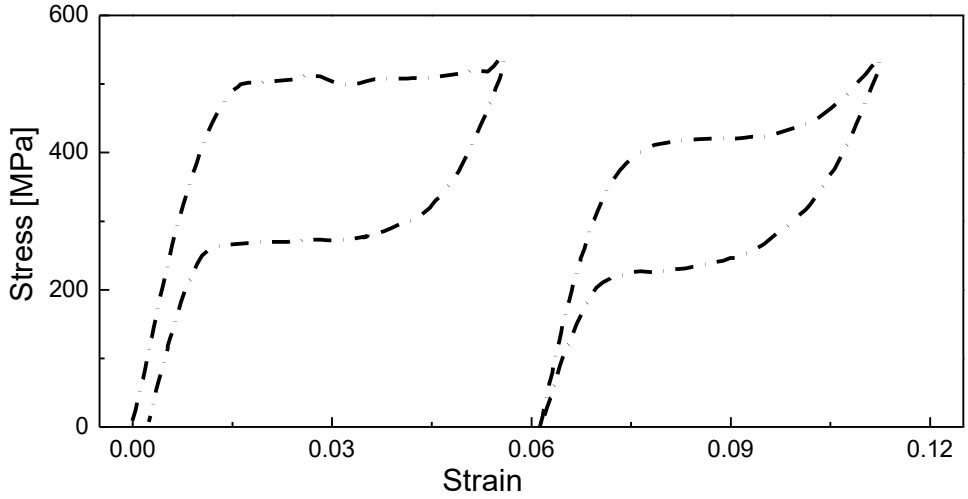

Figure 1.11: The 1^{st} and 50^{th} pseudoelastic loading cycle of a NiTi SMA wire subjected to a 550 MPa stress tension loading and unloading at isothermal condition, adapted from [97].

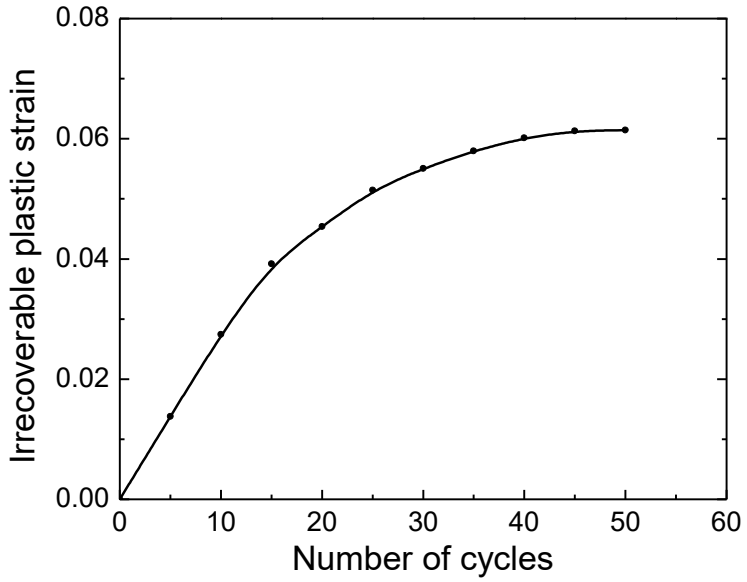

Figure 1.12: Accumulation of TRIP strain with respect to the number of loading cycles for the NiTi SMA under cyclic pseudoelastic response, adapted from [97].

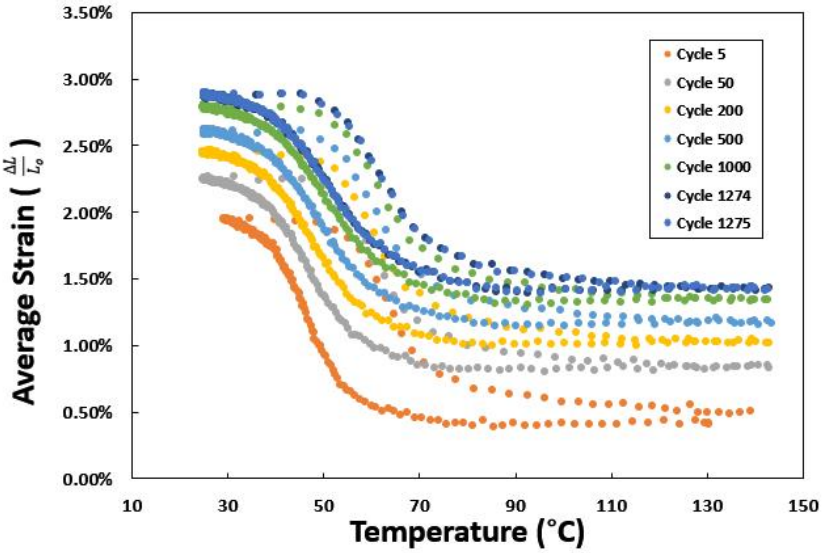

Figure 1.13: Cyclic actuation response of a $Ni_{60}Ti_{10}$ (wt.%) SMA dogbone specimen under thermal cycling at constant load 300 MPa, adapted from [109].

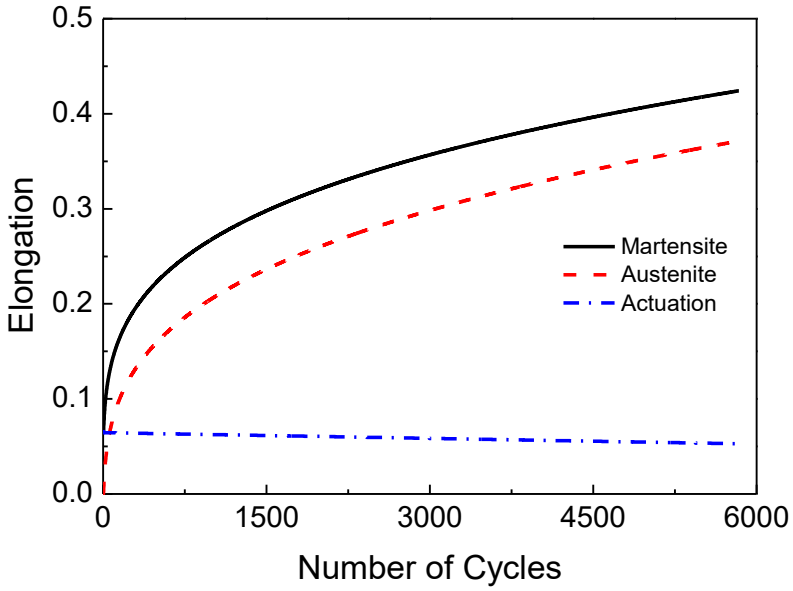

Figure 1.14: The elongation evolution results of an NiTi SMA at martensitic and austenic phases in an actuation fatigue experiment. Legend Martensite (Austenite) means the strain levels measured at martensitic(austenitic) phases while Actuation means the difference between them, adapted from [110].

1.3.1 Multiaxial TRIP evolution under non-uniform stress field

The TRIP strain evolution subjected to the uniaxial condition during cyclic thermomechanical loading is described in the previous sections, yet limited research has addressed TRIP evolution in the multiaxial case where a non-uniform stress field usually exists. However, the majority of applications require the functionality of actuators under multiaxial stress state either originated from geometry complexities or installment required discontinuities such as notches and holes. It has been demonstrated that the TRIP strain under such a multiaxial stress state evolves quite differently compared to that in the uniaxial one. Refer to Figure 1.15, a multiaxial non-uniform stress field is caused in the notched plate actuator due to the presence of the discontinuous cutout, a larger stress field is caused in the notch front while a much smaller stress field is shown in the rest of plate region. As such the phase transformation of the notched plate is largely redistributed. Specifically, the stress concentrated part starts the phase transformation much earlier due to the stress concentration compared to the less stressed part.

The experimental results from Figure 1.15 further show that the non-uniform multiaxial stress state has a significant impact on the TRIP strain accumulation from cycle to cycle. The TRIP strain accumulates much faster in the stress concentrated part in contrast to the less stress concentrated area. Specifically, the TRIP strain accumulated with a larger value over 1% in the notch front where there is a stress concentration while it accumulated a value lower than 0.5% in the rest of the less stressed plate actuator. Digital Image Correlation (DIC) results of transformation and TRIP strain for a notched NiTi plate revealed that a larger TRIP strain was generated at the stress concentration region over the less stressed part. Despite the importance of the fact that multiaxial stress state significantly affecting the evolution of the TRIP strain, it has rarely been addressed among existing models. This brings the second objective of this dissertation.

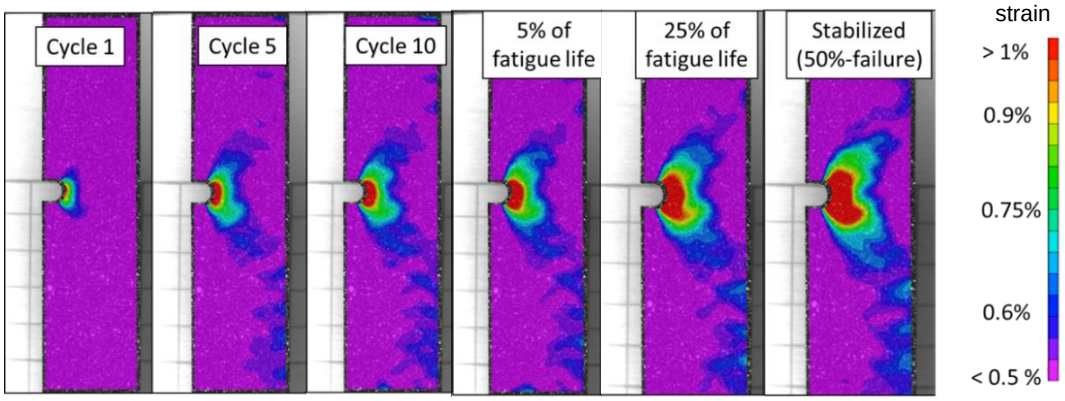

Figure 1.15: Evolution of transformation and TRIP strain for a notched NiTi plate subjected to thermal cycling under constant load, the contour is showing the summation of transformation and TRIP strain along the loading direction, adapted from [109].

1.3.2 Two-way shape memory effect after training

Another intrinsic phenomenon showed during the cyclic response for SMAs is the two-way shape memory effect (TWSME) after an appropriate training procedure. In general, SMAs exhibit the shape changes and recoveries under external bias load via the phase transformation between oriented martensite and austenite. However, SMAs sometimes can present repeatable shape changes even under load-free conditions after stress or thermal cycling, such phenomenon is the so-called TWSME. The TWSME feature can be perceived in SMAs with repeated phase transformations via either mechanical loading-unloading under constant temperature or thermal cycling with constant stress. Refer to Figure 1.16, the experimental result shows the TWSME for a NiTi material after 100 thermal training cycles at the load-free condition. The red curve is the response under bias load, and the blue curve indicates the TWSME response under load-free condition. Such cyclic loading under stress induces repeated phase transitions between oriented martensite and austenite, which results in changes in the microstructure of the material. Refer

to Figure 1.17 for the TEM images showing the microstructure of an SMA sample, it can be seen that after loading a large amount of dislocation bands are accumulated at the interfaces between different martensitic variants and the grain boundaries. These microstructure changes then introduce an internal stress field inside the material, hence promoting the initiation of oriented martensitic phase transformation when the SMA undergoes thermal cycling in the absence of mechanical bias load. Apart from the previously described training procedure, another method to induce TWSME is by aging the SMAs in the martensite phase subjected to a constant stress level [83]. However, the TWSME can be disturbed if the generated internal stress field is altered under certain conditions, such as aging the material or a mechanical overload to change the microstructure [84]. This TWSME feature exhibited by trained SMAs is also addressed in modeling effort of this dissertation.

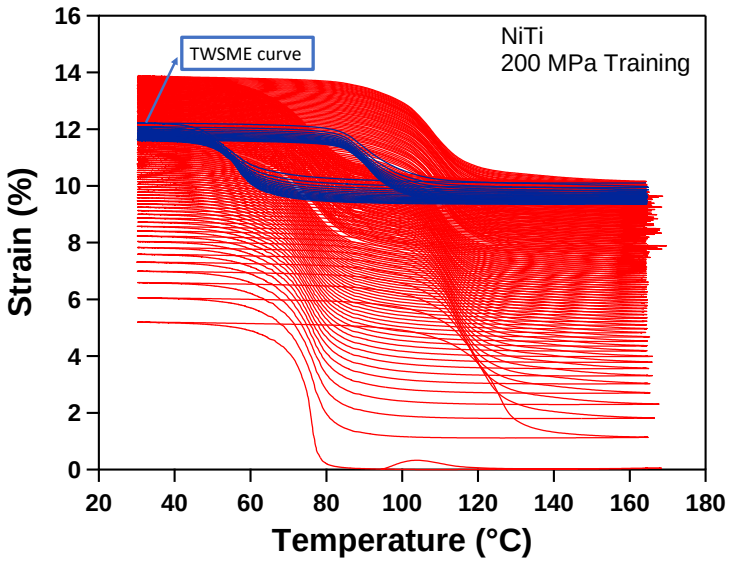

Figure 1.16: Experimental result showing the induced TWSME at load-free condition for a NiTi material after 100 thermal cycles under a constant load. The red curve is the response under bias load, and the blue curve indicates the TWSME reponse under load-free condition, adapted from [3].

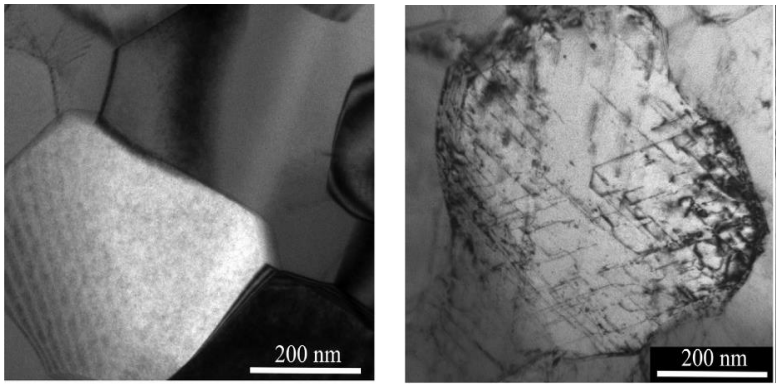

Figure 1.17: TEM images showing the microstructure changes of an NiTi specimen subjected to 10 loading cycles, (a) before the cyclic loading (b) after the cyclic loading (from Figure 18 of [91], © 2018 Elsevier, with permission of Elsevier, https://doi.org /10.1016/j.pmatsci.2018.07.003).

1.4 Research objectives

1.4.1 Finite strain constitutive modeling for SMAs under large deformation

The first objective of this dissertation lies in the proposition of a finite strain constitutive model for polycrystalline SMAs under large deformations. As it was mentioned in the previous discussion, SMAs can undergo large strains and also rotations, although a large number of constitutive theories for SMAs have been proposed so far, the majority of them are developed based on the infinitesimal strain theory, it is necessary to develop a constitutive model based on a finite deformation framework to provide an accurate prediction for the response of SMAs. Throughout the history of the development of finite strain constitutive models for SMAs, two kinematic assumptions are often employed in the finite deformation theory, i.e., the multiplicative decomposition of the deformation gradient and the additive decomposition of the strain rate tensor. Finite strain models based on additive decomposition significantly reduces the complexities in the model formulations compared to the multiplicative approach, which in return tremendously increases

the model computational efficiency as a 3-D design tool. As such they are widely used in current finite element software such as Abaqus and ANSYS. However, objective stress rates are required in additive models because the rate form hypoelastic constitutive relation needs to satisfy the so-called principle of objectivity. Several objective rates, such as the Zaremba-Jaumann-Noll rate, Green-Naghdi-Dienes rate, and Truesdell rate, have been proposed to that purpose, but those objective rates are not essentially "objective" because of their failure to integrate the rate form hypoelastic relation to yield a free energy based hyperelastic stress strain relationship [116]. As a result, spurious phenomena (e.g., shear stress oscillation, residual stress errors, etc.) are often observed in the predicted responses using these objective rates even for simple elastic materials. However, the previously mentioned self-inconsistency issue related to those non-integrable objective rates was resolved by the proposition of the logarithmic rate [112, 113, 13]. Although several finite strain SMA models have developed by using the newly proposed logarithmic rate [69, 102, 111, 124, 120, 117, 119], some of the very important phase transformation characteristics, such as the smooth transition during the phase transformation, the stress-dependent transformation strain to account for the coexistence of oriented/self-accommodated martensitic variants, and a stress-dependent critical driving force to consider the effect of applied stress levels on the size of hysteresis loop, have not been addressed among them.

A finite strain constitutive model for SMAs using the logarithmic strain and rate is proposed as the first objective of this work. As a continuous development from the infinitesimal SMA model [47], the proposed model has a simple model structure and considers three very important characteristics for SMA response as its infinitesimal counterpart does. The development of this model results in an improved computational efficiency and robustness to predict the SMA response at large deformation, without introducing additional intermediate state variables, such as Mandel stress, that are utilized in the mul-

tiplicative models. Moreover, this modeling formulation carefully examines the residual stress errors caused by using other non-integrable objective rates in current commercial finite element packages. The model capability to eliminate such stress errors shows significant importance for the analysis of SMA-based actuators, e.g., SMA beam and SMA torque tube subjected to cyclic large deformation, which paves a solid foundation for the further extension of this model to consider the multiaxial TRIP evolution considered as the second objective of this work.

1.4.2 Modeling of multiaxial TRIP evolution and TWSME

Based on the framework of the proposed finite strain model for SMAs from the first objective, the second goal of this dissertation focus on extending that model to further consider the multiaxial TRIP evolution under non-uniform stress state and the TWSME at load-free condition after training. Although many of the commonly cited models have enabled researchers to study the evolving material behaviors of SMAs, the majority of them are insufficient in their capacity to consider the following critical features. (i) The first aspect of many available models in need of improvement is their kinematic assumption based on infinitesimal strain theory. This assumption may be acceptable for SMA material systems, such as Ni-rich or NiTiHf SMAs, where the total deformation strain regime is below 3%. However, it has been reported that nearly 30% or even higher TRIP strains are observed during the lifetime of near equiatomic NiTi SMA-based actuators [110]. In the presence of such large strain, a finite strain model is needed to account for the exhibited large strains to provide an accurate structural response of SMA-based functional components. (ii) The second important aspect of many current models in need of improvement is the TWSME characteristic exhibited by trained SMAs at load-free conditions. Because of the required training process to stabilize the response of as-received SMAs before used as actuators, permanent changes such as dislocation bands, accumu-

lated defects/damage, and retained martensite variants are introduced in the microstructure of the material, which then results in the generation of an oriented internal stress field. The generated internal stresses oriented in the same direction as the applied load are subsequently able to induce the oriented phase transformation under thermal cycling without applying any pre-loading, i.e., the TWSME. In addition, (iii) the majority of applications require the functionality of actuators under multiaxial stress state originated from geometry complexities or installment required discontinuities, such as notches and holes. TRIP strain under such a multiaxial stress state evolves quite differently compared to that in the uniaxial loading case.

In order to address the three aforementioned critical features, a three-dimensional finite strain constitutive model accounting for multiaxial TRIP evolution and TWSME for SMAs is proposed in this dissertation. The presented modeling effort is developed based on the baseline model developed in the first objective. By using the martensitic volume fraction, transformation strain, internal stress, and TRIP strain tensors as internal state variables, the model is able to capture the TRIP evolution in SMAs subjected to multiaxial stress state during cyclic thermomechanical loading, and the TWSME due to the generation of internal stresses exhibited by trained SMAs at load-free conditions.

1.4.3 Summary of dissertation

The dissertation is organized as the following major chapters:

- Chapter 2 presents a brief review of the fundamental elements for the constitutive modeling of SMAs. These fundamental elements consist of the basic kinematics from continuum mechanics, various stress and strain measures, the basic principles from thermodynamics, constitutive theories for dissipative materials using internal state variables, and the finite deformation framework using logarithmic rate and strain.

- Chapter 3 focuses on the proposition of a finite strain constitutive model for polycrystalline SMAs under large deformation. The model is developed through classical thermodynamic laws combined with the standard Coleman-Noll procedure. The scalar martensitic volume fraction and the second-order transformation strain tensor are chosen as the internal state variables to capture the material response exhibited by polycrystalline SMAs. A detailed implementation procedure of the proposed model is described through a user-defined material subroutine. Numerical experiments considering SMA components including a bar, a beam, a torque tube and a solid flexible structure under stress/thermally-induced phase transformations are investigated via the proposed model, and the results under cyclic loading are compared against the predictions provided by using the Abaqus nonlinear solver.

- In Chapter 4, the finite strain baseline model proposed in the previous chapter is further extended to consider the multiaxial TRIP evolution under non-uniform stress fields and the TWSME after training. By using the martensitic volume fraction, transformation strain, internal stress, and TRIP strain tensors as internal state variables, the model is able to capture the multiaxial TRIP evolution when SMAs are subjected to non-uniform stress state, as well as the TWSME at load-free condition due to the generation of internal stresses exhibited by SMAs after cyclic thermomechanical loading. A detailed implementation procedure of the proposed model is presented through a user-defined material subroutine within a numerical environment for solving different bound value problems. Finally, the predicted cyclic pseudoelastic and actuation responses by this model for a wide range of SMA material systems, including, NiTiCu, NiTi and NiTiHf SMAs, under both uniaxial and multiaxial loading conditions, are compared against experimental results to validate the proposed modeling capabilities.

- Chapter 5 provides a summary and conclusions of this dissertation and discusses some potential future works.

2. PRELIMINARIES OF CONTINUUM MECHANICS AND THERMODYNAMICS

In this chapter, a brief review of the fundamental elements for the modeling of SMAs are introduced here. Those knowledge are well-established and can be learned in a much more detailed manner from many available classical mechanics textbooks elsewhere [26, 36, 48, 51, 23]. The definitions and notations presented here are systematically used throughout the later chapters and sections of the dissertation. These fundamental elements consist of the basic kinematics from continuum mechanics, stress and strain measures that work as energetic conjugate pairs, the basic principles from thermodynamics, constitutive theories for dissipative materials using internal state variables, and the finite deformation framework using logarithmic strain and rate.

2.1 Kinematics

Consider a continuous body possessing an initial state $\mathcal{B}_0$ in the reference configuration at time t_0, changes to another state $\mathcal{B}$ in the current configuration at time t after the deformation. Referring to Figure 2.1, a material point P from the continuous body is defined by a position vector $\mathbf{X}$ in the reference (undeformed) configuration, and vector $\mathbf{x}$ represents its location in the current (deformed) configuration at time t, during which the material point P undergoes a displacement that can be described by the vector $\boldsymbol{u}(\mathbf{X}, t)$. A neighboring point Q defined by position vector $\mathbf{X} + d\mathbf{X}$ undergoes the displacement $\boldsymbol{u}(\boldsymbol{X} + d\mathbf{X}, t)$ arriving at $\boldsymbol{x} + d\boldsymbol{x}$. Therefore, the deformation process of the material segment between $d\mathbf{X}$ at the reference configuration and $d\boldsymbol{x}$ at the current configuration can be defined through the well-known deformation gradient tensor $\mathbf{F}(\boldsymbol{x}, t)$,

$$d\boldsymbol{x} = \mathbf{F}\ d\mathbf{X} \tag{2.1}$$

It is known that for any real deformation gradient tensor $\mathbf{F}$ with a non-zero determinant, the following polar decomposition on $\mathbf{F}$ can be obtained,

$$\mathbf{F} = \mathbf{RU} = \mathbf{VR} \tag{2.2}$$

In the above equation, $\mathbf{U}$ is called the right stretch tensor while $\mathbf{V}$ is the left stretch tensor, they are both positive definite symmetric tensors., and the remaining $\mathbf{R}$ is an orthogonal tensor. This decomposition is unique in the sense that only one $\mathbf{R}$, one $\mathbf{U}$, and one $\mathbf{V}$ satisfy the above equation at the same time. The polar decomposition indicates that any admissible deformation processes for the continuous body can be decomposed into a pure rigid body rotation followed by a pure stretch, i.e., $\mathbf{F} = \mathbf{VR}$, or into a pure stretch first followed by a rigid body rotation, i.e., $\mathbf{F} = \mathbf{RU}$.

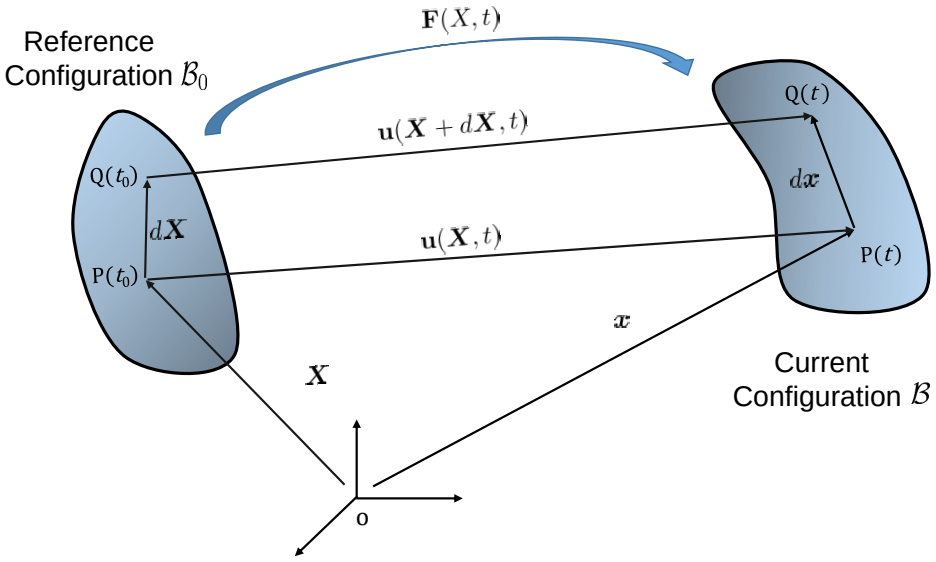

Figure 2.1: The schematics of deformation for the continuous body between the reference and the current configurations.

The following spectrum decomposition can be received based on the symmetric stretch tensors, for right stretch $\mathbf{U}$,

$$\mathbf{U} = \sum_{i=1}^{3} \lambda_i \boldsymbol{l}_i \otimes \boldsymbol{l}_i \tag{2.3}$$

for left stretch $\mathbf{V}$,

$$\mathbf{V} = \sum_{i=1}^{3} \lambda_i \boldsymbol{q}_i \otimes \boldsymbol{q}_i \tag{2.4}$$

where the scalars $\{\lambda_1, \lambda_2, \lambda_3\}$ are called the principal stretches which are the eigenvalues of $\mathbf{U}$ and $\mathbf{V}$, and the unit base vectors $\{\boldsymbol{l}_1, \boldsymbol{l}_2, \boldsymbol{l}_3\}$ and $\{\boldsymbol{q}_1, \boldsymbol{q}_2, \boldsymbol{q}_3\}$ are called, respectively, the *Lagrangian* and *Eulerian* triads dictating the *Lagrangian* and *Eulerian* principal directions.

Based on the left/right stretch tensors, the right Cauchy-Green tensor $\mathbf{B}$ and the left Cauchy-Green tensor $\mathbf{C}$ can be derived as,

$$\mathbf{B} = \mathbf{F}\mathbf{F}^{\mathbf{T}} = \mathbf{V}^2 \tag{2.5}$$

$$\mathbf{C} = \mathbf{F}^{\mathbf{T}}\mathbf{F} = \mathbf{U}^2 \tag{2.6}$$

2.2 Strain measures

There are many different strain measures available in the literature, and there is by no means a unique method of defining strain. In fact, a specific choice of strain measure is usually willful and mainly controlled by its mathematical convenience for specific model construction. Despite the various preferences on different strain measures, two major categories can be listed based on their formulation triads. A category of strain measure is introduced as Lagrangian strain tensors as follows, i.e., strain measures formulated by using Lagrangian triads [88, 35, 71].

$$\mathbf{E}^{(m)} = \begin{cases} \frac{1}{m}(\mathbf{U}^m - \mathbf{I}) & m \neq 0, \\ \ln[\mathbf{U}] & m = 0 \end{cases} \tag{2.7}$$

In the above equation, m is a real number, and $\ln[\cdot]$ indicates the tensor logarithm of $[\cdot]$. The above equation can be reformulated by virtue of the principal stretches and Lagrangian triads as,

$$\mathbf{E}^{(m)} = \sum_{i=1}^{3} f(\lambda_i)\, \boldsymbol{l}_i \otimes \boldsymbol{l}_i \tag{2.8}$$

where

$$f(\lambda_i) = \begin{cases} \frac{1}{m}(\lambda_i^m - 1) & m \neq 0, \\ \ln \lambda_i & m = 0 \end{cases} \tag{2.9}$$

The counterpart of Lagrangian strain tensors are the Eulerian strain tensors which have the Eulerian principal directions, i.e., strain measures formulated based on the Eulerian triads. Based on the left stretch, the Eulerian strain tensors are defined as,

$$\mathbf{e}^{(m)} = \begin{cases} \frac{1}{m}(\mathbf{V}^m - \mathbf{I}) & m \neq 0, \\ \ln[\mathbf{V}] & m = 0 \end{cases} \tag{2.10}$$

The Eulerian strain tensors can be reformulated by virtue of the principal stretches and Eulerian triads as,

$$\mathbf{e}^{(m)} = \sum_{i=1}^{3} f(\lambda_i)\, \boldsymbol{q}_i \otimes \boldsymbol{q}_i \tag{2.11}$$

where $f(\lambda_i)$ has the same definition as equation (2.9). The Lagrangian strain tensors are

related to the Eulerian strain tensors by the rotation tensor $\mathbf{R}$,

$$\mathbf{e}^{(m)} = \mathbf{R}\,\mathbf{E}^{(m)}\mathbf{R}^T \tag{2.12}$$

It is worthy to point out that the commonly used Green-Lagrangian strain measure in large deformation theory, i.e., $\mathbf{E}^{(2)} = \frac{1}{2}(\mathbf{U}^2 - \mathbf{I})$, belongs to the type of the Lagrangian strain tensors with $m = 2$. Other commonly utilized strain measures can also be deduced from the discussed strain family. For examples, Hencky strain with $m = 0$, the Biot strain with $m = 1$, and Almansi strain with $m = -2$. The Hencky strain measure of its Eulerian type $\mathbf{h}$ is the strain measure employed in the later chapters for the formulation of the constitutive model for SMAs under large deformation and considering other advanced features. It is particularly reviewed here.

$$\mathbf{h} = \ln(\mathbf{V}) \tag{2.13}$$

2.3 Stress measures and Forces

In the previous sections, the kinematic description of the deformation of an idealized continuous body was discussed. Concepts such as the deformation gradient and its polar decomposition, and different strain measures quantifying the internal stretch inside the idealized continuum body consist of the most fundamental elements for the construction of the constitutive theory of solids. It is intuitive to think that, as an energetic-conjugate, the forces and stress measures associated with the previously discussed deformation kinematics should be made clear. This section focus on this objective. A more detailed review of this part can be found from additional textbooks [51, 23].

In the realm of classical continuum mechanics where material is assumed to be continuously distributed, the forces acting at every material point associated with the deforma-

tion of continua can be categorized, in general, into two major types: (1) boundary forces applied on the boundary of the body arising from the contact with another body. The unit of such forces is usually force per unit area (2) body forces as a result of the presence of a physical field, such as gravity, magnetic, electric fields induced forces. Those body forces are exerted throughout the entire continua regardless of its location and time. The unit of such forces is usually force per unit volume. It is often acknowledged that molecules, atoms and subatomic particles constitute a material body. The resulting internal forces then arise in really matter from the interactions of these particles. In order to describe these forces in a mathematical manner, the concept of stress is needed and the different ways of quantifying it are introduced in the following sections

2.3.1 Cauchy stress tensor

One of the most basic axioms in continuum mechanics is Cauchy's stress principle which states that there exists a linear relationship between the surface traction $\boldsymbol{t}(\boldsymbol{x}, \boldsymbol{n})$ and the unit normal vector $\mathbf{n}$, in other words, there is a second-order tensor field $\boldsymbol{\sigma}$ such that the traction vector is given by

$$\boldsymbol{t}(\boldsymbol{x}, \boldsymbol{n}) = \boldsymbol{\sigma}(\boldsymbol{x})\boldsymbol{n} \tag{2.14}$$

Furthermore, due to the balance of angular momentum, $\boldsymbol{\sigma}$ is a symmetric tensor,

$$\boldsymbol{\sigma} = \boldsymbol{\sigma}^T \tag{2.15}$$

The second-order tensor $\boldsymbol{\sigma}$ is called the Cauchy stress tensor or the true stress tensor usually. Up to this point, it should be pointed out that the forces within the continuous material are connected by the molecular and atomic bonds that are discrete quantities. The continuous mathematical interpretation of these interactions by virtue of the second-order

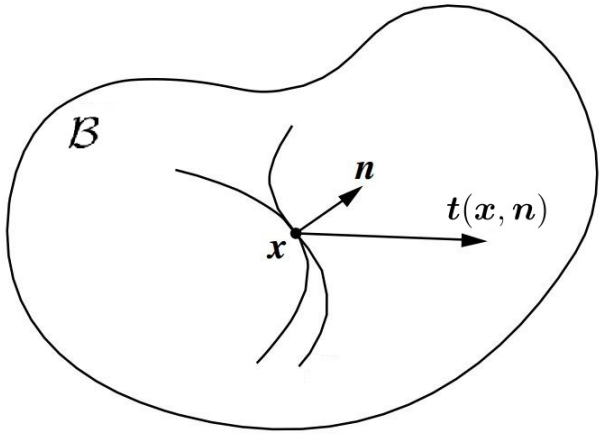

Figure 2.2: The schematics of traction forces at current configuration.

Cauchy stress tensor is valid only in an averaging sense for a sufficiently representative volume of material. This assumption is also adopted in other variables such as strain measures or other continuous field variables related to the continua. It is noted that the Cauchy stress tensor is defined in the deformed configuration and thus can be represented by using the afore introduced Eulerian triads $\{\boldsymbol{q}_1, \boldsymbol{q}_2, \boldsymbol{q}_3\}$ as,

$$\boldsymbol{\sigma} = \sigma_{ij}\ \boldsymbol{q}_i \otimes \boldsymbol{q}_j \tag{2.16}$$

For the convenience of formulation of constitutive models, the stress tensors are often decomposed into the summation of a spherical part and a deviatoric part, i.e.,

$$\boldsymbol{\sigma} = \boldsymbol{s} + p\mathbf{I} \tag{2.17}$$

where p is called the hydrostatic pressure,

$$p\mathbf{I} = \frac{1}{3}\text{tr}(\boldsymbol{\sigma})\mathbf{I} \tag{2.18}$$

and $\boldsymbol{s}$ is the deviatoric stress component,

$$\boldsymbol{s} = \boldsymbol{\sigma} - p\mathbf{I} \tag{2.19}$$

2.3.2 Kirchhoff stress tensor

Another important stress measure that has the same principal directions as Cauchy stress tensor is the Kirchhoff stress tensor $\boldsymbol{\tau}$ defined in the following equation wherein J is the determinant of the deformation gradient, i.e., $J = det|\mathbf{F}|$. Therefore, $\boldsymbol{\tau}$ is also a Eulerian variable defined in the current configuration. It can be deduced that the Kirchhoff stress is a symmetric tensor as a result of the symmetry of Cauchy stress tensor $\boldsymbol{\sigma}$.

$$\boldsymbol{\tau} = J\boldsymbol{\sigma} \tag{2.20}$$

In the following chapters, the energetic conjugate pair, i.e., Kirchhoff stress $\boldsymbol{\tau}$ and the Hencky strain of its Eulerian type $\mathbf{h}$, are utilized as stress and strain measures in the formulation of the constitutive model for SMAs.

2.3.3 Piola-Kirchhoff stress tensors

As discussed in the previous sections, there are strain measures defined not only in the Lagrangian configurations but also in the Eulerian configuration, so do they with stress measures. The introduced Cauchy stress and Kirchoff stress tensors are both variables defined in the Eulerian configuration, their counterparts are those defined in the Lagrangian configuration. The most commonly used ones are the first and second Piola-Kirchhoff stress tensors.

The vector $\boldsymbol{t}$ in equation (2.14) indicates the traction applied on a unit area in the deformed material surface with a normal vector $\boldsymbol{n}$. To obtain the definition of first Piola-Kirchhoff stress, anther important quantity $\bar{\boldsymbol{t}}$, the counterpart of $\boldsymbol{t}$, measures the traction

that exerts on that unit area in the reference material surface with normal vector $\boldsymbol{m}$. Let ds denote an infinitesimal area in the deformed configuration and ds_0 be its counterpart in the deformed configuration, the following relationship between $\bar{\boldsymbol{t}}$ and $\boldsymbol{t}$ is expressed,

$$\bar{\boldsymbol{t}}\, ds_0 = \boldsymbol{t}\, ds \tag{2.21}$$

with the combination of equations (2.14) and (2.21), $\bar{\boldsymbol{t}}$ can be reformulated as,

$$\bar{\boldsymbol{t}} = J\boldsymbol{\sigma}\mathbf{F}^{-T}\boldsymbol{m} = \mathbf{P}\,\boldsymbol{m} \tag{2.22}$$

the above equation brings the following definition for the first Piola-Kirchhoff stress tensor,

$$\mathbf{P} = J\boldsymbol{\sigma}\mathbf{F}^{-T} \tag{2.23}$$

It is clear to see that the first Piola-Kirchhoff stress tensor is an unsymmetric tensor. As the symmetry feature of a variable often comes with a reward in the mathematical derivation, which motivates the introduction of the second Piola-Kirchhoff stress tensor, a symmetric tensor, as follows,

$$\mathbf{S} = J\mathbf{F}^{-1}\boldsymbol{\sigma}\mathbf{F}^{-T} \tag{2.24}$$

It should be noted that the energetic conjugate pair of the second Piola-Kirchhoff stress tensor $\mathbf{S}$ is the Green-Lagrangian strain tensor $\mathbf{E}^{(2)}$.

2.4 Fundamental principles of thermodynamics

In order to formulate the constitutive theories in the later section, the fundamental principles of thermodynamics are reviewed here. They are conservation of mass, conservation of linear momentum, conservation of angular momentum, conservation of energy,

and the entropy inequality. The conservation of energy is also called the first principle of thermodynamics, and entropy inequality is also called the second principle of thermodynamics.

2.4.1 Conservation of mass

The conservation of mass indicates that the rate of change of mass for continua is always zero with respect to time and deformation, which can be expressed in the following equation,

$$\frac{D}{Dt}\int_V \rho dV = 0 \tag{2.25}$$

In the preceding equation, ρ is the density of the body, V is the volume of the body, and $\frac{D}{Dt}$ means the material derivative. By using the Reynolds transport theorem, the integral form of conservation of mass can derive the following local form,

$$\frac{\partial \rho}{\partial t} + \text{div}(\rho \mathbf{v}) = 0 \tag{2.26}$$

in which, $\mathbf{v}$ is the velocity field of the material point, and div means the divergence of that vector variable.

2.4.2 Conservation of linear momentum

The conservation of linear momentum indicates that the rate of change of linear momentum for a continuum media is equal to the summation of total forces applied on it, which can be expressed in the following integral form as,

$$\frac{D}{Dt}\big(\int_V \rho\, \mathbf{v} dV\big) = \int_{\partial V} \boldsymbol{t}\, dS + \int_V \boldsymbol{b}\, dV \tag{2.27}$$

in the preceding equation, $\boldsymbol{t}$ is the traction applied on the body surface, and $\boldsymbol{b}$ is the body force vector exhibited on the entire body. By using the conservation of mass and the relationship in equation (2.14), the following local form can be obtained,

$$\rho \frac{D\boldsymbol{v}}{Dt} = \text{div}(\boldsymbol{\sigma}) + \boldsymbol{b} \tag{2.28}$$

2.4.3 Conservation of angular momentum

The conservation of angular momentum states that the rate of change of angular momentum for a continuum medium about a fixed point is equal to the summation of total moments caused by the surface and body forces applied on it plus the existing body couples, which can be expressed in the following equation by using the integral form,

$$\frac{D}{Dt}\Big(\int_V \boldsymbol{r} \times \rho \, \mathbf{v} dV \Big) = \int_{\partial V} \boldsymbol{r} \times \boldsymbol{t} \, dS + \int_V \boldsymbol{r} \times \boldsymbol{b} \, dV \tag{2.29}$$

in the preceding equation, $\boldsymbol{r}$ means the position of the fixed point, '$\times$' means the cross product of two vectors. The result obtained from the conversation of angular momentum means that the Cauchy stress tensor is symmetric, i.e.,

$$\boldsymbol{\sigma} = \boldsymbol{\sigma}^T \tag{2.30}$$

2.4.4 Conservation of energy

The principle of conservation of energy, also called the first law of thermodynamics, states that the rate of change of summation of kinetic and internal energy for the continua is equal to the summation of the rate of work applied by surface and body forces, rate of heat flow across the boundary, and heat supply within the body. The integral form of this

principle can be expressed as follows,

$$\frac{D}{Dt}\int_V \big(\frac{1}{2}\rho \boldsymbol{v}^2+\rho u\big)dV = \int_{\partial V} \boldsymbol{t}\cdot\boldsymbol{v}\; dS+\int_V \boldsymbol{b}\cdot\boldsymbol{v}\; dV-\int_{\partial V}(\boldsymbol{q}\cdot\boldsymbol{n})\; dS+\int_V \rho r\; dV \quad (2.31)$$

in the preceding equation, u is the internal energy per unit mass, $\boldsymbol{q}$ is the heat flux vector, r is the heat supply per unit mass, $\boldsymbol{n}$ is a unit normal vector on the body surface ∂V, $(-\boldsymbol{q}\cdot\boldsymbol{n})$ indicates the rate of heat flowing into the body. The local form of this principle of conservation of energy can be expressed as,

$$\rho\dot{u} = \boldsymbol{\sigma} : \mathbf{D} - \text{div}(\boldsymbol{q}) + \rho r \quad (2.32)$$

in which ':' means the contraction operation between two tensors, $(\boldsymbol{\sigma} : \mathbf{D})$ means the stress power per unit deformed volume. The local form of conservation of energy indicates that the rate of change of internal energy equals the stress power per unit deformed volume minus the divergence of the heat flux, plus heat production within the body.

2.4.5 Entropy inequality

The entropy inequality, also knowns as the second law of thermodynamics or the Clausius - Duhem inequality, states that the sum of the total internal entropy production within the system is always no less than zero, which can be expressed in the following integral form as,

$$\frac{D}{Dt}\big(\int_V \rho s dV\big)+\int_{\partial V}\frac{\boldsymbol{q}}{T}\cdot\boldsymbol{n}\; dS-\int_V \frac{\rho r}{T}\; dV \geqslant 0 \quad (2.33)$$

in the above equation, s is the entropy per unit mass. By using the divergence theorem and the conservation of mass, the following local form of the entropy inequality can be

obtained,

$$\rho\dot{s} + \frac{1}{T}\text{div}(\boldsymbol{q}) - \frac{\boldsymbol{q}}{T^2} \cdot \boldsymbol{\nabla} T - \frac{\rho r}{T} \geqslant 0 \tag{2.34}$$

Because the heat flux always flows from a higher temperature place to a lower one, the term $-\frac{\boldsymbol{q}}{T^2} \cdot \boldsymbol{\nabla} T$ is always a quantity greater than zero. Thus the following strict form of the entropy inequality, called Clausius-Planck inequality, is obtained.

$$\rho\dot{s} + \frac{1}{T}\text{div}(\boldsymbol{q}) - \frac{\rho r}{T} \geqslant 0 \tag{2.35}$$

2.5 Thermodynamic framework

In this subsection, the generic derivation of constitutive equations for dissipative materials is presented, which is utilized for the formulation of constitutive modeling of SMAs in the later sections. The formulation of constitutive models usually starts with the selection of a set of thermodynamic state variables to define the thermodynamic potential. Thermodynamic state variables are those quantities that can determine a specific thermodynamic state for the material bodies [20, 21]. The state variables are called external ones if they can be measured, while those can not be directly measured are called internal state variables. In the case of SMAs, the internal state variables can be martensitic volume fraction, transformation strain, internal stress tensor, and transformation-induced plasticity tensor.

After the determination of both external and internal state variables, a thermodynamic potential function, characterizing a specific thermodynamic status for a material, can thus be formulated [37]. In general, there is a total of four thermodynamic potentials commonly adopted in constitutive modeling depending on their choice of independent state variables, i.e., the internal energy function,u, the enthalpy function, h, the Helmholtz free energy function, ψ, and the specific Gibbs free energy function, G. All four thermody-

namic potentials are defined per unit mass. Specifically, the internal energy u is a measure that combines the kinetic and potential energy in the material system. The Helmholtz free energy ψ is a measure of the portion in internal energy that is accessible for providing external work subjected to a constant temperature, while enthalpy h is the available portion in internal energy that is able to be transferred as heat energy under constant applied stress. In the end, the Gibbs free energy is the available portion in enthalpy that can be used for doing work subjected to a constant temperature. The aforementioned four thermodynamic potentials have the following relations linked to each other, in which $\boldsymbol{\sigma}$ is the Cauchy stress and $\boldsymbol{\varepsilon}$ is the infinitesimal strain tensor.

The relation between the internal energy and enthalpy is,

$$h = u - \frac{1}{\rho}\boldsymbol{\sigma} : \boldsymbol{\varepsilon} \tag{2.36}$$

The Gibbs free energy is correlated with the internal energy as,

$$G = u - \frac{1}{\rho}\boldsymbol{\sigma} : \boldsymbol{\varepsilon} - sT \tag{2.37}$$

The Helmholtz free energy is linked with the internal energy as,

$$\psi = u - sT \tag{2.38}$$

When it comes to the choice of the thermodynamic potential for the formulation of constitutive models, an intuitive option can be the internal energy. However, as the internal energy is controlled by the state variable entropy h, which is not a quantity can be directly measured, the internal energy is barely used in model derivations. The same situation applies to the enthalpy. Thus, the two commonly adopted thermodynamic potentials are the Helmholtz free energy ψ and the Gibbs free energy G. The specific selection

between them is usually based on the preference on the state variables, i.e., stress (load) or strain (displacement) control, that the researchers want to control in the experiments. In the following section, the Gibbs free energy is chosen as the thermodynamic potential for the formulation of constitutive models for SMAs.

To proceed the formulation of constitutive models for dissipative materials, such as SMAs, the thermodynamic potential, Gibbs free energy G, is prescribed to be a continuous function dependent on Cauchy stress tensor $\boldsymbol{\sigma}$, infinitesimal strain tensor $\boldsymbol{\varepsilon}$, temperature T and a set of internal state variables $\boldsymbol{\Upsilon}$. The selection of a set of internal state variables that can properly describe the experimentally observed material dissipative response is an important part to formulate constitutive relations. In the case of a conventional plastic material such as steel, magnesium, and aluminum, the second-order irrecoverable plastic strain tensor is usually used for the consideration of the nonlinear material response. In the case of SMAs, the martensitic volume fraction ξ and the infinitesimal transformation strain $\boldsymbol{\varepsilon}^{tr}$ (assuming small strain theory) are usually selected as internal state variables $\boldsymbol{\Upsilon} = \{\xi, \boldsymbol{\varepsilon}^{tr}\}$ to characterize the phase transformation and thermomechanical response of SMAs. Specifically, $\xi = 0$ means the material is fully in austenitic phase, $\xi = 1$ indicates the material is fully in the martensitic phase, and $0 < \xi < 1$ means the material is in mixed phase. The transformation strain $\boldsymbol{\varepsilon}^{tr}$ is responsible for the fully recoverable strain upon unloading/heating the SMA material. In Chapter 4, another two internal state variables, i.e., transformation-induced plastic strain and internal stress tensors, are introduced into the current constitutive model as an extension of the model to consider the evolving material response of SMAs under cyclic loading.

$$G(\boldsymbol{\sigma}, T, \boldsymbol{\Upsilon}) = u - \frac{1}{\rho}\boldsymbol{\sigma} : \boldsymbol{\varepsilon} - sT \tag{2.39}$$

where ρ is the density of the material, s and u are the specific entropy and internal energy

respectively. By assuming the Gibbs free energy is a continuous function based on its independent state variables, the chain rule differentiation can be applied on G, thus the following rate form of G can be obtained,

$$\dot{G} = \dot{u} - \frac{1}{\rho}\,\dot{\boldsymbol{\sigma}} : \boldsymbol{\varepsilon} - \frac{1}{\rho}\boldsymbol{\sigma} : \dot{\boldsymbol{\varepsilon}} - s\dot{T} - \dot{s}T \tag{2.40}$$

in addition, the following equation is derived after the rearrangement of equation (2.40),

$$\dot{u} - \dot{s}T = \dot{G} + \frac{1}{\rho}\,\dot{\boldsymbol{\sigma}} : \boldsymbol{\varepsilon} + \frac{1}{\rho}\boldsymbol{\sigma} : \dot{\boldsymbol{\varepsilon}} + s\dot{T} \tag{2.41}$$

Based on the 2^{nd} law of thermodynamics, by combining the conservation of energy in equation (2.32), the strict form of dissipation inequality (2.35), and also the equivalence between the rate of the infinitesimal strain and the rate of deformation tensor under small deformation assumption, i.e., $\dot{\boldsymbol{\varepsilon}} = \mathbf{D}$, the dissipation energy $\mathcal{D}$ can be written in the following form of inequality,

$$\mathcal{D} = \boldsymbol{\sigma} : \mathbf{D} - \rho(\dot{u} - T\dot{s}) \geqslant 0 \tag{2.42}$$

After the substitution of the rate form equation (3.22) into the inequality (3.20), the dissipation energy is reformulated as,

$$\mathcal{D} = -\rho\dot{G} - \rho s\dot{T} - \dot{\boldsymbol{\sigma}} : \boldsymbol{\varepsilon} \geqslant 0 \tag{2.43}$$

The Gibbs free energy $G(\boldsymbol{\sigma}, T, \boldsymbol{\Upsilon})$ is prescribed to a continuous function dependent on Cauchy stress $\boldsymbol{\sigma}$, temperature T and a set of internal state variables $\boldsymbol{\varepsilon}$ undetermined, after the application of chain rule differentiation of G with respect to these independent

state variables (i.e., $\boldsymbol{\sigma}$, T and $\boldsymbol{\Upsilon}$), the following equation is derived,

$$\dot{G} = \frac{\partial G}{\partial \boldsymbol{\sigma}} : \dot{\boldsymbol{\sigma}} + \frac{\partial G}{\partial T}\dot{T} + \frac{\partial G}{\partial \boldsymbol{\Upsilon}} : \dot{\boldsymbol{\Upsilon}} \tag{2.44}$$

Substitution of the preceding equation (3.24) into equation (3.23) yields the following expression for the dissipation energy $\mathcal{D}$,

$$\mathcal{D} = -(\rho\frac{\partial G}{\partial \boldsymbol{\sigma}} + \boldsymbol{\varepsilon}) : \dot{\boldsymbol{\sigma}} - (\rho\frac{\partial G}{\partial T} + s) : \dot{T} - \rho\frac{\partial G}{\partial \boldsymbol{\Upsilon}} : \dot{\boldsymbol{\Upsilon}} \geqslant 0 \tag{2.45}$$

One of the most important steps to obtain the constitutive relations is the so-called Coleman-Noll procedure, which states that all the admissible values of $\dot{\boldsymbol{\sigma}}$, $\dot{T}$ and $\dot{\boldsymbol{\Upsilon}}$ have to comply with the dissipation inequality (3.25) regardless of their thermodynamic paths, thereby the following constitutive relationships between stress and strain, entropy and temperature can be obtained,

$$\boldsymbol{\varepsilon} = -\rho\frac{\partial G}{\partial \boldsymbol{\sigma}} \tag{2.46}$$

$$s = -\rho\frac{\partial G}{\partial T} \tag{2.47}$$

By substituting the obtained constitutive relationships (3.26) and (3.27) back into inequality (3.25), the following reduced form of the dissipation inequality is acquired,

$$-\rho\frac{\partial G}{\partial \boldsymbol{\Upsilon}} : \dot{\boldsymbol{\Upsilon}} \geqslant 0 \tag{2.48}$$

2.6 Finite strain constitutive modeling using logarithmic strain and rate

This section focus on the large deformation framework using the newly proposed logarithmic rate together with the logarithmic strain. In general, two kinematic assumptions are often adopted in the finite deformation theory, i.e., the multiplicative decomposition

of the deformation gradient and the additive decomposition of the strain rate tensor. In the multiplicative approach, the deformation gradient is usually decomposed into an elastic part multiplied with an irrecoverable part, $\mathbf{F} = \mathbf{F}^e\mathbf{F}^{ie}$, while in the additive models, the rate of deformation tensor is decomposed into an elastic part followed by an irrecoverable part, $\mathbf{D} = \mathbf{D}^e + \mathbf{D}^{ir}$. It is known that finite strain constitutive models based on additive decomposition significantly reduces the complexities of the model structure thereby they are widely used in current available finite element software (e.g., Abaqus, ANSYS). To satisfy the principle of objectivity, additive models are usually required to employ an objective rate in its rate form hypoelastic constitutive relation. A number of objective rates (such as Zaremba-Jaumann-Noll rate, Green-Naghdi-Dienes rate, and Truesdell rate) have been proposed to meet this goal. However, those objective rates are not essentially "objective" because of their failure to integrate the rate form hypoelastic relation into the hyperelastic stress-strain equation (2.54) [116]. As a result, spurious phenomena (e.g., shear stress oscillation, residual stress errors, etc.) are often observed in the predicted response even for non-dissipative elastic materials. To illustrate the issues with objective rates, two boundary value problems are chosen to be analyzed by using the hypoelastic constitutive relationships.

The constitutive relationship for thermoelastic materials based on additive kinematic assumption can be expressed as equation (2.49), in which $\mathcal{C}$ is the fourth-order stiffness tensor of the elastic material, $\boldsymbol{\tau}$ is the Kirchhoff stress tensor, and a circle over $\boldsymbol{\tau}$ means the objective rates adopted.

$$\mathring{\boldsymbol{\tau}} = \mathcal{C} : \mathbf{D} \tag{2.49}$$

The previously mentioned self-inconsistency issue related to non-integrable objective rates was resolved by the logarithmic rate proposed in the works [112, 113, 13, 14, 15, 66, 67], in which they indicates that the logarithmic rate of Eulerian logarithmic strain

$\mathbf{h}$ is identical to the rate of deformation tensor $\mathbf{D}$. This unique relationship between logarithmic strain $\mathbf{h}$ and the strain rate tensor $\mathbf{D}$ can be expressed as follows,

$$\mathring{\mathbf{h}}^{log} = \dot{\mathbf{h}} + \mathbf{h}\boldsymbol{\Omega}^{log} - \boldsymbol{\Omega}^{log}\mathbf{h} = \mathbf{D} \tag{2.50}$$

where $\boldsymbol{\Omega}^{log}$ is called the logarithmic spin introduced by [112] defined as,

$$\boldsymbol{\Omega}^{log} = \mathbf{W} + \sum_{i \neq j}^{n} \left(\frac{1 + (\lambda_i/\lambda_j)}{1 - (\lambda_i/\lambda_j)} + \frac{2}{\ln(\lambda_i/\lambda_j)}\right)\mathbf{b}_i\mathbf{D}\mathbf{b}_j \tag{2.51}$$

in which $\lambda_{i,j}(i, j = 1, 2, 3)$ are the eigenvalues of left Cauchy-Green tensor $\mathbf{B}$ and $\mathbf{b}_i, \mathbf{b}_j$ are the corresponding subordinate eigenprojections. As along as the logarithmic spin tensor $\boldsymbol{\Omega}^{log}$ is defined, the second order rotation tensor $\mathbf{R}^{log}$, associated with $\boldsymbol{\Omega}^{log}$, can be determined through the following differential equation (4.3). In general cases, the initial condition of $\mathbf{R}^{log}$ is assumed as $\mathbf{R}^{log}|_{t=0} = \mathbf{I}$.

$$\boldsymbol{\Omega}^{log} = \dot{\mathbf{R}}^{log}(\mathbf{R}^{log})^T \tag{2.52}$$

By using the corotational integration technique defined from [45], and assume the initial conditions for strain as $\mathbf{h}|_{t=0} = \mathbf{0}$, the rate form equation (2.50) can be integrated to yield the following relation between the total logarithmic strain $\mathbf{h}$ and the logarithmic corotational integration of $\mathbf{D}$,

$$\mathbf{h} = \int_{\text{corot.}} \mathbf{D}\, \mathrm{d}t = (\mathbf{R}^{log})^T \left(\int_0^t \mathbf{R}^{log}\mathbf{D}^e(\mathbf{R}^{log})^T \mathrm{d}t' \right) \mathbf{R}^{log} \tag{2.53}$$

By applying the logarithmic corotational integration on the rate form constitutive equation (2.49), the following algebraic constitutive equation between the Kirchhoff stress

tensor $\boldsymbol{\tau}$ and the Eulerian logarithmic strain $\mathbf{h}$ can be derived,

$$\boldsymbol{\tau} = \mathcal{C} : \mathbf{h} \tag{2.54}$$

During the following subsections, two elastic boundary value problems are analyzed to demonstrate the benefits of using logarithmic strain and rate to formulate the finite strain constitutive models. The first boundary value problem is a simple elastic cube under simple shear deformation, and the second one is a simple elastic cube under closed path cyclic loading.

2.6.1 Elastic cube under simple shear

As it was proved from [112], the hypoelastic formulation (2.49) using logarithmic rate can be self-consistently integrated to the hyperelastic equation (2.54) using logarithmic strain via the logarithmic corotational integration. The example in this subsection is to demonstrate such equivalence between the rate form hypoelastic formulation and the algebraic form hyperelastic formulation to characterize the simple elastic response.

Refer to Figure 2.3 for the boundary value problem schematic, a simple elastic cube with length H is under simple shear loading, the cube top face is subjected to a displacement control shearing deformation using displacement u_{max} in X_2 direction. The cube is a simple elastic material with Young's modulus of E and Poisson's ratio $\nu = 0.33$. The simulation was conducted using commercial finite element software Abaqus, in which the cube meshed with one three-dimensional C3D8 element. A UMAT corresponding to the rate form hypoelastic formulation (2.49) and another one corresponding to the hyperelastic formulation (2.54) were implemented into Abaqus to solve the boundary value problems here.

First, the simulation was conducted using the Abaqus built-in nonlinear geometry solver (designated as NLGEOM) with 500 incremental step until the maximum displace-

ment u_{max} was reached, it is noted that when NLGEOM is activated in Abaqus, the constitutive equation to calculate the stress-strain response is the rate form hypoelastic equation (2.49) using Jaumman rate. Afterward, the same simulation was conducted by using the UMAT describing hyperelastic formulation with 200 incremental steps. Finally, the simulation was performed by using the hypoelastic UMAT with 200 to 10000 incremental steps. The shear Kirchhoff stress components τ_{12} predicted by different methods in the all above simulations are summarized in Figure 2.4.

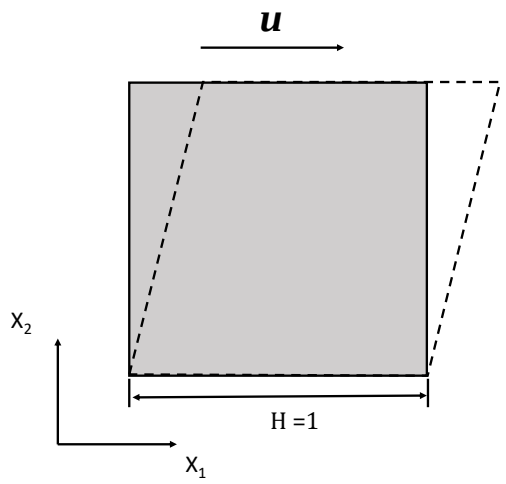

Figure 2.3: The schematic of a simple elastic square under simple shear loading conditions.

Figure 2.4 shows the normalized shear stress component $\boldsymbol{\tau}/E$ versus the normalized displacement u/u_{max}. The rate form hypoelastic formulation presents a stress-displacement response converging to the response produced by the hyperelastic formulation as the number of increments increases. The difference between the responses predicted by these two formulations is almost negligible, which demonstrates what was proved in the work [113] that the hypoelastic constitutive formulation can be integrated

into the hyperelastic constitutive formulation via the logarithmic corotational integration. In contrast, the response predicted by the hypoelastic formulation using Zarempa–Jauman rate shows a spurious shear stress oscillation.

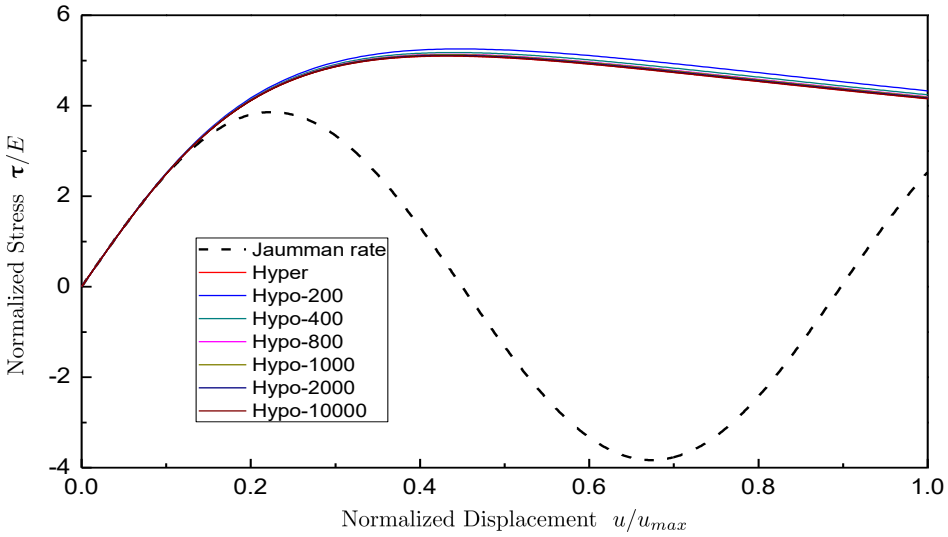

Figure 2.4: The shear Kirchhoff stress components predicted by the hyperelastic formulation (Eq. (2.54)) using logarithmic strain and hypoelastic formulation (Eq. (2.49)) using Jaumman and logarithmic rates.

2.6.2 Elastic cube under closed path cyclic loading

In this subsection, an elastic cube under closed path cyclic loading is investigated to study the residual stress errors caused by the hypoelastic formulation using other non-integrable objective rates. Refer to Figure 2.5 for the boundary value problem schematics, an elastic cube with length H is under a closed path cyclic loading. The upper face of the cube is subjected to a displacement-controlled circular deformation, the deformation over geometry ratio is $r/H = 0.2$ to represent a relatively large deformation situation. The shear Kirchhoff stress components are examined by the hypoelastic equation (2.49) with 10 consecutive closed path loading cycles. Based on the results from [112], hypoelastic

equation (2.49) using logarithmic rate can be self-consistently integrated to a hyperelastic constitutive equation (2.54) based on logarithmic strain through the logarithmic corotational integration [45]. In order to demonstrate that, the Kirchhoff stress components are obtained by the rate form hypoelastic equation (2.49) with three different objective rates, *i.e.* Jaumman rate, Green-Naghdi rate, and Logarithmic rate. The predicted results are presented in Figure 2.6, Figure 2.7 and Figure 2.8. The stress results are normalized by the material Young's modulus E.

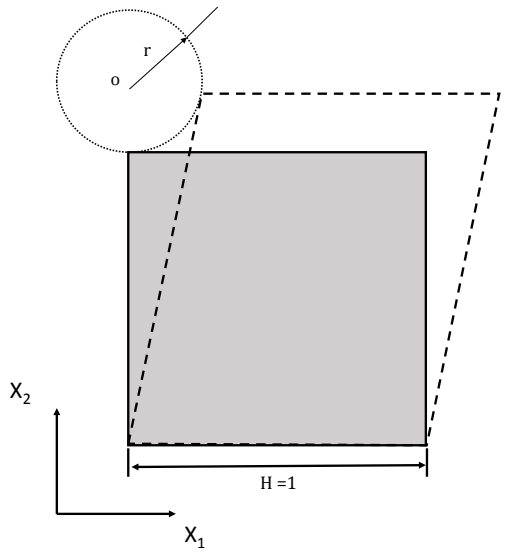

Figure 2.5: The schematic of a simple elastic square under closed path cyclic loading.

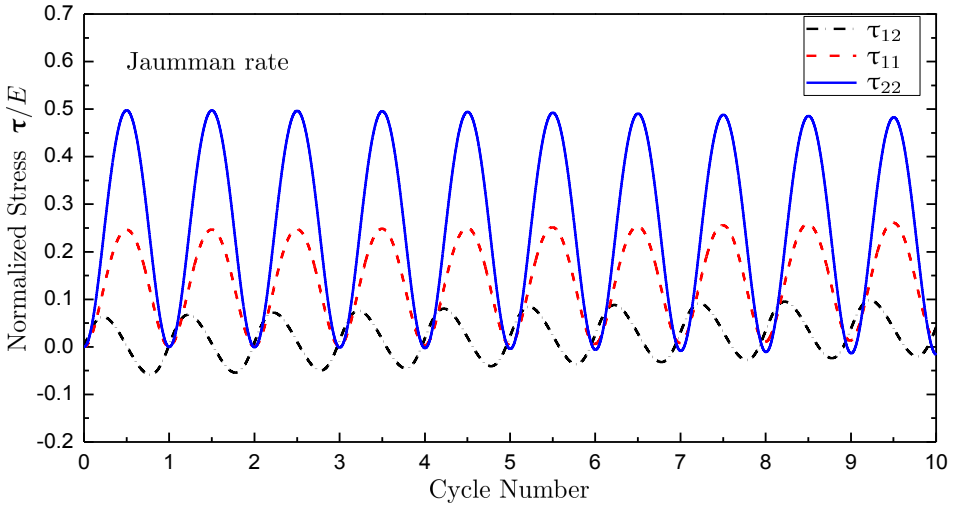

Figure 2.6: Kirchhoff stress components predicted by hypoelastic equation using Jaumman rate under 10 loading cycles

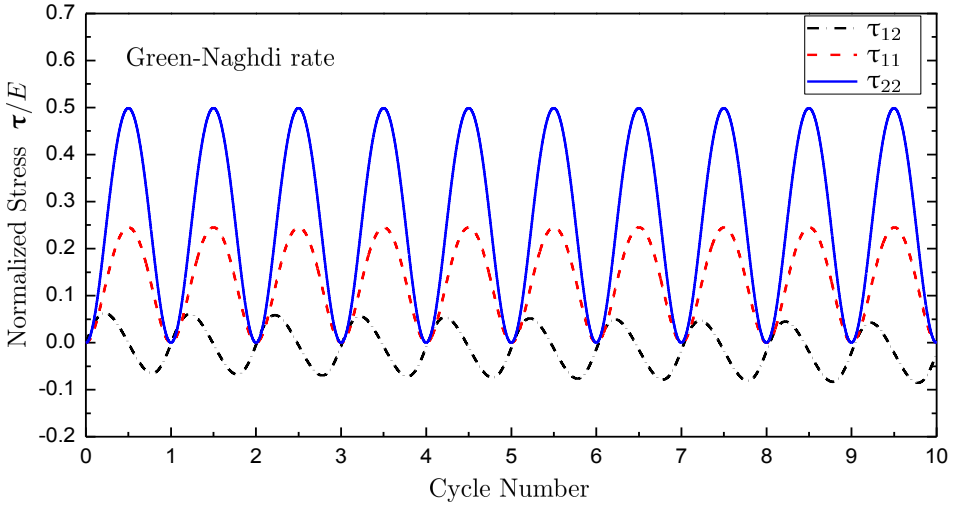

Figure 2.7: Kirchhoff stress components predicted by hypoelastic equation using Green-Naghdi rate under 10 loading cycles

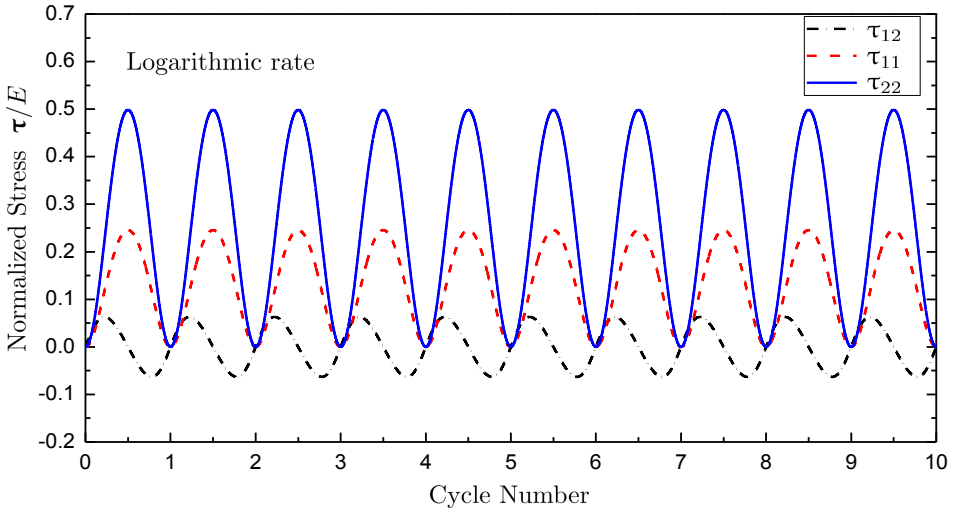

Figure 2.8: Kirchhoff stress components predicted by hypoelastic equation using Logarithmic rate under 10 loading cycles

Table 2.1: Stress residuals obtained by hypoelastic equation (2.49) with different objective rates for the elastic square

Normalized stress	Logarithmic rate	Jaumman rate	Green-Naghdi rate
τ_{11}/E	-1.71e-5	0.0164	2.17 e-6
τ_{12}/E	2.17e-6	0.0411	-0.023
τ_{22}/E	1.71e-5	-0.0164	1.76e-5

The stress residuals are examined at the end of the loading cycle and summarized in table 2.1. First, the stress components in all the three cases showed periodic oscillation. Since the material is confined to behave elastically, the deformation should be indissipative to anticipate that all the stress components should return to zero value in the end. However, the predicted stress components in the cases of Jaumman rate and Green-Naghdi rate showed artificial stress residuals are introduced. Refer to figure 2.6 for the

case of Jaumman rate, stress residuals τ_{11} is 0.0164, τ_{22} is -0.0164 and τ_{12} is 0.0411 after the 10 loading cycles. In the case of Green-Naghdi rate, although there are inconsiderable stress residuals for τ_{11} and τ_{22} components, the shear residuals τ_{12} is -0.023. In contrast, all the stress residuals are almost negligible in the case of Logarithmic rate, which demonstrates that the hypoelastic constitutive equation utilizing logarithmic rate can be self-consistently integrated to deliver a hyperelastic equation based on the logarithmic strain. Interested readers are encouraged to further read [66, 115].

3. FINITE STRAIN CONSITUTIVE MODELING FOR MARTENSITIC TRANSFORMATION IN POLYCRYSTALLINE SHAPE MEMORY ALLOYS *

3.1 Introduction

SMAs belong to a specialized subgroup of multifunctional materials known as active materials and are capable of recovering their pre-defined geometry when subjected to a thermal stimulus above certain temperatures. This unique property of SMAs is achieved through a solid-to-solid state diffusionless phase transformation between the high-symmetry, high-temperature austenitic phase and the low-symmetry, low-temperature martensitic phase [48]. Since the discovery of shape memory effect, SMAs have been extensively investigated as sensors and actuators towards building smart systems integrated with adaptive and morphing features [76, 33]. Recently, aerospace researchers have considered using the SMA-based actuators to reconfigure the shape of a supersonic aircraft to meet the noise and efficiency requirements in response to the real-time changing ambient environment, which has the great potential to realize a commercially viable overland civil supersonic flight in the near future [52, 122].

A substantial number of constitutive theories for SMAs have been proposed so far with the majority of them based on the infinitesimal strain theory for small deformation analysis. Thorough reviews can be found from [81, 10, 7, 80, 73, 56, 57, 74, 125, 85, 27, 17, 87, 19]. In general, constitutive models for SMAs can be approximately categorized into three different types: phase-field theory based models, crystal-plasticity theory based models, and classical J_2-flow theory based models. The phase-field models, in which order parameters are utilized to differentiate austenitic and martensitic phases, can track

*Portions of this chapter are reprinted or adapted from [121], L. Xu, T. Baxevanis, and D.C. Lagoudas, A three-dimensional constitutive model for the martensitic transformation in polycrystalline shape memory alloys under large deformation. Smart Materials and Structures, Volume 28, Issue 7, 074004, 2019. doi:10.1088/1361-665x/ab1acb

microstructure evolution, such as phases front movement, during the phase transformation process [56, 57, 18, 94, 93, 64, 126]. Therefore, phase-field theory based models are well suited to investigate the dynamic nucleation and phase morphology growth for martensitic phase transformation in SMAs. The enormous computational time, however, needed to solve the phase kinetic partial differential equations hinders its popularity to the extent that macroscopic structural response is concerned. In regard to crystal-plasticity theory based models [103, 107, 123], with the consideration of the effect of material microstructure (e.g., crystal orientation, texture, etc.), these models are able to capture the anisotropy in material response (e.g., tension-compression asymmetry) exhibited by textured polycrystalline SMAs. Similar to phase-field methods, the complex implementation procedure of these models to incorporate the microstructure information makes them computational costly. Following the legacy of J_2-flow theory, phenomenological SMA models have attracted attention in the engineering community where repetitive designs and optimization procedures on SMA components are needed to find target shapes. By introducing a set of internal state variables (such as volume fraction and transformation strain tensor), J_2 theory-based SMA models are able to simulate the macroscopic response of an SMA component in an efficient way. The simplicity of this model type and its well-established implementation procedure have allowed it to be widely used among real engineering applications [5, 47, 11, 12, 53, 58, 125, 82].

Constitutive models based on the infinitesimal strain theory are able to predict SMA response accurately under small deformation situations. However, it has been reported that SMAs can reversibly deform to a relatively large strain regime up to 8% [89, 39]. Also for specific boundary value problems such as fracture in SMAs, the strain levels close to the crack tip are well beyond 10% [29, 28] within the finite strain regime. In addition to such relatively large strain, SMA-based actuators (e.g., spring, beam, torque tube) may also undergo large rotation during their deployment. For example, an SMA beam

component is used as a bending actuator in order to realize a morphing engine shape, where the SMA experienced large bending induced rotation [33]. Another example is the SMA tube component utilized as a torsional actuator to repeatedly rotate a deployable and retractable solar panel [108], where the SMA tube is subjected to cyclic large rotation. Combining the aforementioned two facts that SMAs may undergo large strain and rotation, it is necessary to develop a constitutive model based on a finite deformation framework to provide an accurate prediction for the response of SMAs.

Two kinematic assumptions are often employed in the finite deformation theory, i.e., the multiplicative decomposition of the deformation gradient and the additive decomposition of the strain rate tensor. In the multiplicative approach, the deformation gradient is usually decomposed into an elastic part multiplied with an inelastic part. Finite strain SMA models based on the multiplicative decomposition can be obtained from literature [129, 82, 25, 105, 106, 99, 22], among which some advanced capabilities are considered. For example, Wang and coworkers [106] presented a finite strain SMA model with the fully thermomechanically coupled feature, the consideration of coexistence of different martensitic variants, and accounting for temperature effect on the hysteresis size. In the work of Stupkiewicz and Petryk [99], they proposed a finite strain SMA model to capture the tension-compression asymmetry phenomenon. Damanpack and coworkers [22] also developed an SMA model that considers anisotropic behaviors and reorientation in SMAs at finite deformation. However, it is known that finite strain model based on additive decomposition significantly reduces the complexities of the model structure compared to multiplicative models, which in return facilitates the computational efficiency of the finite strain model as a 3-D design tool. Therefore, they are widely used in current available finite element software (e.g., Abaqus, ANSYS). However, to satisfy the principle of objectivity, additive models are required to use an objective rate in its rate form hypoelastic constitutive relation. A number of objective rates (such as Zaremba-Jaumann-

Noll rate, Green-Naghdi-Dienes rate, and Truesdell rate) have been proposed to meet this goal. However, those objective rates are not essentially “objective" because of their failure to integrate the rate form hypoelastic relation to yield a free energy based hyperelastic stress-strain relation [116]. As a result, spurious phenomena (e.g., shear stress oscillation, artificial stress residuals, etc.) are often observed in the predicted response even for simple elastic materials through these objective rates.

It was not until the logarithmic rate was proposed in the literature [112, 113, 13, 14, 15, 66, 67] that the previously mentioned self-inconsistency issue related to non-integrable objective rates was resolved. As was proved in the work [112], the logarithmic rate of Eulerian logarithmic strain $\mathbf{h}$ is exactly identical to the strain rate tensor $\mathbf{D}$, and the logarithmic strain is the only one among all other strain measures enjoying this important property. Therefore, the finite strain models using logarithmic strain and rate are not only able to capture large strain and large rotation but also are capable of resolving the aforementioned spurious phenomena. This new development in finite deformation theory not only provides a solution to classical finite elastoplastic problems for conventional metallic materials [127, 128], but also sheds light on the finite strain model development for active materials such as SMAs. Few SMA models using additive approach can be found from [69, 102, 111, 124, 120, 117, 119], but some of the very important SMA phase transformation characteristics have not been addressed among them, such as the smooth transition during the phase transformation, the stress-dependent transformation strain to account for the coexistence of oriented/self-accommodated martensitic variants, and a stress-dependent critical driving force to consider the effect of applied stress levels on the size of hysteresis loop. To this end, this work presents a finite strain SMA model formulation based on the additive decomposition using the logarithmic strain and rate. As a continuous development from the infinitesimal SMA model [47], the proposed model has a simple model structure and considers three very important characteristics

for SMA response as its infinitesimal counterpart does. These developments combined result in improved computational efficiency and robustness for the proposed finite strain model to predict the SMA response at large deformation, without introducing additional intermediate state variables, such as Mandel stress, that are utilized in the multiplicative models. It is noted that the primary focus of this work is mainly on the formulation of a finite strain SMA model, rather than the development of a constitutive model that can capture the full complexities of the SMA thermomechanical deformation. Thus, tension-compression, latent-heat effects, reorientation between orientated and self-accommodated martensitic variants, cyclic evolution features (transformation-induced plasticity, two-way shape memory effect at stress-free conditions) are not included here for simplicity. Moreover, this work carefully examines the artificial stress errors caused by using other non-integrable objective rates in current commercial finite element packages. The capability of the proposed model to eliminate such stress errors shows significant importance for the analysis of SMA-based actuators, e.g., SMA beam and SMA torque tube subjected to cyclic large deformation.

This work is organized as follows. Section 3.2 presents the kinematic preliminaries. Section 3.3 concentrates on the model development based on the logarithmic strain and logarithmic rate. The derivation of the consistent tangent stiffness matrix and the consistent thermal matrix are also provided. In section 3.4, the detailed implementation procedure for the proposed model is described by using a user-defined material subroutine (UMAT) through the finite element software Abaqus. A detailed calibration procedure for the material parameters used in this model is also provided in the Section 3.5. Numerical examples are studied to demonstrate the capability of the proposed model in Section 3.6. Conclusions are presented in Section 3.7.

3.2 Preliminaries

3.2.1 Kinematics

Let material point $\mathcal{P}$ from body $\mathcal{B}$ be defined by a position vector $\mathbf{X}$ in the reference (undeformed) configuration at time t_0, and let vector $\mathbf{x}$ represent the position vector of that material point in the current (deformed) configuration at time t. Therefore ,the deformation process of point $\mathcal{P}$ between the reference configuration and the current configuration can be defined through the well-known deformation gradient tensor $\mathbf{F}(\mathbf{x}, t)$:

$$\mathbf{F}(\mathbf{x}, t) = \frac{\partial \mathbf{x}}{\partial \mathbf{X}} \tag{3.1}$$

and the velocity field $\mathbf{v}$ can be defined as,

$$\mathbf{v} = \frac{d\mathbf{x}}{dt} = \dot{\mathbf{x}} \tag{3.2}$$

based on the velocity field $\mathbf{v}$, the velocity gradient $\mathbf{L}$ can be derived as,

$$\mathbf{L} = \frac{\partial \mathbf{v}}{\partial \mathbf{x}} = \dot{\mathbf{F}}\mathbf{F}^{-1} \tag{3.3}$$

the following polar decomposition equation for deformation gradient $\mathbf{F}$ is well known,

$$\mathbf{F} = \mathbf{R}\mathbf{U} = \mathbf{V}\mathbf{R} \tag{3.4}$$

where $\mathbf{R}$ is the rotation tensor, $\mathbf{U}$ and $\mathbf{V}$ are the right (or Lagrangian) and the left (or Eulerian) stretch tensors, respectively, by which the right Cauchy-Green tensor $\mathbf{C}$ and the left Cauchy-Green tensor $\mathbf{B}$ can be obtained, as follows,

$$\mathbf{C} = \mathbf{F}^{\mathbf{T}}\mathbf{F} = \mathbf{U}^2 \tag{3.5}$$

$$\mathbf{B} = \mathbf{F}\mathbf{F}^{\mathbf{T}} = \mathbf{V}^2 \tag{3.6}$$

where $\mathbf{I}$ is the second order identity tensor. The logarithmic strain (also called Hencky or true strain) of Lagrangian type $\mathbf{H}$ and Eulerian type $\mathbf{h}$ can thus be defined as,

$$\mathbf{H} = \frac{1}{2}\ln(\mathbf{C}) = \ln(\mathbf{U}) \tag{3.7}$$

$$\mathbf{h} = \frac{1}{2}\ln(\mathbf{B}) = \ln(\mathbf{V}) \tag{3.8}$$

It is also well known that the velocity gradient $\mathbf{L}$ can be additively decomposed into a symmetric part, the strain rate tensor $\mathbf{D}$, and an anti-symmetric part, the spin tensor $\mathbf{W}$,

$$\mathbf{L} = \mathbf{D} + \mathbf{W}, \qquad \mathbf{D} = \frac{1}{2}(\mathbf{L} + \mathbf{L}^{\mathbf{T}}), \qquad \mathbf{W} = \frac{1}{2}(\mathbf{L} - \mathbf{L}^{\mathbf{T}}) \tag{3.9}$$

3.2.2 Logarithmic strain, logarithmic rate and logarithmic spin

As was mentioned in section 3.1, two widely accepted kinematic assumptions, i.e., the multiplicative decomposition of deformation gradient $\mathbf{F}$ and the additive decomposition of the strain rate tensor $\mathbf{D}$, are usually considered in finite deformation theory. The multiplicative models use a hyperelastic constitutive relation while a rate form hypoelastic constitutive equation is usually adopted for additive models. The rate form hypoelastic constitutive theory using objective rates has been criticized for its non-integrability because it can not well define an essential elastic material behavior [90], this includes many well known objective rates such as Zaremba-Jaumann rate, Green-Naghdi rate, Truesdell rate, etc.[116].

The aforementioned problems about objective rates were solved in the work by Xiao et al.[112, 113, 116], Bruhns et al.[13, 14, 15] and Meyers et al.[66, 67], where they proved that the logarithmic rate of the Eulerian logarithmic strain $\mathbf{h}$ is identical with the strain

rate tensor $\mathbf{D}$, by which a hypoelastic model can be exactly integrated to a hyperelastic finite strain model [112]. This unique relationship between logarithmic strain $\mathbf{h}$ and the strain rate tensor $\mathbf{D}$ is expressed as follows,

$$\mathring{\mathbf{h}}^{log} = \dot{\mathbf{h}} + \mathbf{h}\mathbf{\Omega}^{log} - \mathbf{\Omega}^{log}\mathbf{h} = \mathbf{D} \tag{3.10}$$

where $\mathbf{\Omega}^{log}$ is called the logarithmic spin introduced by [112] defined as,

$$\mathbf{\Omega}^{log} = \mathbf{W} + \sum_{i \neq j}^{n} \left(\frac{1 + (\lambda_i/\lambda_j)}{1 - (\lambda_i/\lambda_j)} + \frac{2}{\ln(\lambda_i/\lambda_j)}\right)\mathbf{b}_i\mathbf{D}\mathbf{b}_j \tag{3.11}$$

in which $\lambda_{i,j}(i, j = 1, 2, 3)$ are the eigenvalues of left Cauchy-Green tensor $\mathbf{B}$ and $\mathbf{b}_i, \mathbf{b}_j$ are the corresponding subordinate eigenprojections. As along as the logarithmic spin tensor $\mathbf{\Omega}^{log}$ is defined, the second order rotation tensor $\mathbf{R}^{log}$, associated with $\mathbf{\Omega}^{log}$, can be determined through the following differential equation (4.3). In general cases, the initial condition is assumed as $\mathbf{R}^{log}|_{t=0} = \mathbf{I}$.

$$\mathbf{\Omega}^{log} = \dot{\mathbf{R}}^{log}(\mathbf{R}^{log})^T \tag{3.12}$$

follow the corotational integration definition from [45], and assume the initial conditions $\mathbf{h}|_{t=0} = \mathbf{0}$, equation (4.1) yields the total logarithmic strain $\mathbf{h}$ after the logarithmic corotational integration,

$$\mathbf{h} = \int_{\text{corot.}} \mathbf{D}\, \mathrm{d}t = (\mathbf{R}^{log})^T \left(\int_0^t \mathbf{R}^{log}\mathbf{D}^e(\mathbf{R}^{log})^T \mathrm{d}t' \right) \mathbf{R}^{log} \tag{3.13}$$

3.2.3 Additive decomposition of logarithmic strain

The kinematic assumption starts with the additive decomposition of the strain rate tensor $\mathbf{D}$ into an elastic part $\mathbf{D}^e$ plus a transformation part $\mathbf{D}^{tr}$,

$$\mathbf{D} = \mathbf{D}^e + \mathbf{D}^{tr} \tag{3.14}$$

The elastic strain rate part $\mathbf{D}^e$ and the transformation strain rate part $\mathbf{D}^{tr}$ in equation (4.5) can be rewritten as $\mathring{\mathbf{h}}^{e\_log}$ and $\mathring{\mathbf{h}}^{tr\_log}$ by virtue of the relation in equation (4.1) respectively,

$$\mathring{\mathbf{h}}^{e\_log} = \mathbf{D}^e; \;\; \mathring{\mathbf{h}}^{tr\_log} = \mathbf{D}^{tr} \tag{3.15}$$

combining equations (4.1), (4.5) and (4.6) obtains the following equation,

$$\mathring{\mathbf{h}}^{log} = \mathring{\mathbf{h}}^{e\_log} + \mathring{\mathbf{h}}^{tr\_log} \tag{3.16}$$

Similar to the results obtained from equation (4.4), equation (4.7) can yield the following relation after applying the logarithmic corotational integration,

$$\mathbf{h}^e = \int_{\text{corot.}} \mathbf{D}^e \, \mathrm{d}t = (\mathbf{R}^{log})^T \left(\int_0^t \mathbf{R}^{log} \mathbf{D}^e (\mathbf{R}^{log})^T \mathrm{d}t' \right) \mathbf{R}^{log} \tag{3.17a}$$

$$\mathbf{h}^{tr} = \int_{\text{corot.}} \mathbf{D}^{tr} \, \mathrm{d}t = (\mathbf{R}^{log})^T \left(\int_0^t \mathbf{R}^{log} \mathbf{D}^{tr} (\mathbf{R}^{log})^T \mathrm{d}t' \right) \mathbf{R}^{log} \tag{3.17b}$$

Based on the additive decomposition on the strain rate tensor, combing equations (4.5), (4.7) and (4.8), the following additive decomposition on the total logarithmic strain $\mathbf{h}$ can be achieved, i.e., the total logarithmic strain $\mathbf{h}$ can be additively split into an elastic

strain like part $\mathbf{h}^e$ plus a transformation strain like part $\mathbf{h}^{tr}$.

$$\mathbf{h} = \mathbf{h}^e + \mathbf{h}^{tr} \tag{3.18}$$

3.3 Model formulation

3.3.1 Thermodynamic framework

The Gibbs free energy potential G is defined to be a continuous function dependent on Kirchhoff stress tensor $\boldsymbol{\tau}$ [1], Eulerian logarithmic strain $\mathbf{h}$, temperature T and a set of internal state variables Υ.

$$G(\boldsymbol{\tau}, \mathbf{h}, T, \boldsymbol{\Upsilon}) = u - \frac{1}{\rho_0}\boldsymbol{\tau} : \mathbf{h} - sT \tag{3.19}$$

where ρ_0 is the density in the reference configuration, s and u are the specific entropy and internal energy respectively. From the 2^{nd} law of thermodynamics, the dissipation energy $\mathcal{D}$ can be written in the form of Clausius-Duhem inequality,

$$\mathcal{D} = \boldsymbol{\tau} : \mathbf{D} - \rho_0(\dot{u} - T\dot{s}) \geqslant 0 \tag{3.20}$$

The logarithmic rate of the Gibbs free energy is taken in equation (3.19). Note that a scalar subjected to an objective rate equals to its conventional time rate, the following equation is derived. An circle hat denotes the logarithmic rate in the following text for brevity.

$$\mathring{G}^{log} = \dot{u} - \frac{1}{\rho_0}\mathring{\boldsymbol{\tau}}^{log} : \mathbf{h} - \frac{1}{\rho_0}\boldsymbol{\tau} : \mathring{\mathbf{h}}^{log} - s\dot{T} - \dot{s}T \tag{3.21}$$

[1] The relationship between Kirchhoff stress $\boldsymbol{\tau}$ and Cauchy stress $\boldsymbol{\sigma}$ is $\boldsymbol{\tau} = J\boldsymbol{\sigma}$, where J is the determinant of the deformation gradient $\mathbf{F}$, i.e., $J = \det|\mathbf{F}|$. Assuming phase transformation to be volume preserving, J is approximately equivalent to 1, so $\boldsymbol{\tau} \approx \boldsymbol{\sigma}$. Kirchhoff stress $\boldsymbol{\tau}$ and Eulerian logarithmic strain $\mathbf{h}$, called an energetic conjugate pair [114], are usually paired up in the formation of free energy potentials.

The following equation can be obtained after rearrangement of equation (3.21),

$$\dot{u} - \dot{s}T = \dot{G} + \frac{1}{\rho_0}\mathring{\boldsymbol{\tau}} : \mathbf{h} + \frac{1}{\rho_0}\boldsymbol{\tau} : \mathring{\mathbf{h}} + s\dot{T} \tag{3.22}$$

Substitute equation (3.22) into Clausius-Duhem inequality (3.20), the dissipation energy is rearranged as the following,

$$\mathcal{D} = -\rho_0\dot{G} - \rho_0 s\dot{T} - \mathring{\boldsymbol{\tau}} : \mathbf{h} \geqslant 0 \tag{3.23}$$

Recall that the Gibbs free energy is a continuous function, chain rule differentiation can be applied on the Gibbs free energy with respect to its independent state variables (i.e., Kirchhoff stress $\boldsymbol{\tau}$, temperature T and internal state variables $\boldsymbol{\Upsilon}$), which gives,

$$\mathring{G} = \frac{\partial G}{\partial \boldsymbol{\tau}} : \mathring{\boldsymbol{\tau}} + \frac{\partial G}{\partial T}\dot{T} + \frac{\partial G}{\partial \boldsymbol{\Upsilon}} : \mathring{\boldsymbol{\Upsilon}} \tag{3.24}$$

Substitute equation (3.24) into equation (3.23), the following expression for the dissipation energy $\mathcal{D}$ is acquired,

$$\mathcal{D} = -(\rho_0\frac{\partial G}{\partial \boldsymbol{\tau}} + \mathbf{h}) : \mathring{\boldsymbol{\tau}} - (\rho_0\frac{\partial G}{\partial T} + s) : \dot{T} - \rho_0\frac{\partial G}{\partial \boldsymbol{\Upsilon}} : \mathring{\boldsymbol{\Upsilon}} \geqslant 0 \tag{3.25}$$

Following the standard Coleman-Noll procedure, all admissible values for $\mathring{\boldsymbol{\tau}}$, $\dot{T}$ and $\mathring{\boldsymbol{\Upsilon}}$ have to comply with the dissipation inequality (3.25) regardless of thermodynamic paths, thereby the constitutive relationships between stress and strain, entropy and temperature can be inferred as,

$$\mathbf{h} = -\rho_0\frac{\partial G}{\partial \boldsymbol{\tau}} \tag{3.26}$$

$$s = -\rho_0\frac{\partial G}{\partial T} \tag{3.27}$$

Substitute equations (3.26) and (3.27) into equation (3.25), the following reduced form of the dissipation inequality is acquired,

$$-\rho_0 \frac{\partial G}{\partial \boldsymbol{\Upsilon}} : \mathring{\boldsymbol{\Upsilon}} \geqslant 0 \tag{3.28}$$

3.3.2 Constitutive modeling for SMAs

3.3.2.1 Thermodynamic potential

The formulation of the proposed model is based on the thermodynamic framework presented in section 3.3 and the early SMA model developed by Lagoudas and coworkers [10, 47] for small deformation analysis. The model is able to predict the pseudoelastic (isothermal) and actuation (isobaric) response under large deformation including both large strain and large rotation. A quadratic Gibbs free energy potential G is introduced in equation (3.29), in which Kirchhoff stress tensor $\boldsymbol{\tau}$ and temperature T are chosen as the independent state variables. The martensitic volume fraction ξ and the second order transformation strain tensor $\mathbf{h}^{tr}$ are chosen as internal state variables $\boldsymbol{\Upsilon} = \{\xi, \mathbf{h}^{tr}\}$ to capture the material response exhibited by polycrystalline SMAs. The Gibbs free energy potential G is employed as follows,

$$\begin{aligned} G = -\frac{1}{2\rho_0}\boldsymbol{\tau} : \mathcal{S}\boldsymbol{\tau} - \frac{1}{\rho_0}\boldsymbol{\tau} : [\,\boldsymbol{\alpha}(T - T_0) + \mathbf{h}^{tr}] + c\Big[(T - T_0) - T\ln(\frac{T}{T_0})\Big] \\ -s_0(T - T_0) + u_0 + \frac{1}{\rho_0} f(\xi) \end{aligned} \tag{3.29}$$

where $\mathcal{S}$ is the effective compliance tensor calculated by equation (3.30), $\mathcal{S}^A$ is the compliance tensor for austenitic phase while $\mathcal{S}^M$ is for martensitic phase, and $\Delta\mathcal{S}$ is the phase difference for the compliance tensor. The effective stiffness tensor $\mathcal{C}$ can be gained by taking the inverse of the effective compliance tensor, i.e., $\mathcal{C} = \mathcal{S}^{-1}$. $\boldsymbol{\alpha}$ is the second order thermoelastic expansion tensor, c is the effective specific heat, s_0 and u_0 are the effective

specific entropy and effective specific internal energy at the reference state. All the aforementioned effective variables are determined from equation (3.31) to (3.34). T represents the temperature at current state while T_0 is the temperature at reference state.

$$\mathcal{S}(\xi) = \mathcal{S}^A + \xi(\mathcal{S}^M - \mathcal{S}^A) = \mathcal{S}^A + \xi\Delta\mathcal{S} \tag{3.30}$$

$$\boldsymbol{\alpha}(\xi) = \boldsymbol{\alpha}^A + \xi(\boldsymbol{\alpha}^M - \boldsymbol{\alpha}^A) = \boldsymbol{\alpha}^A + \xi\Delta\boldsymbol{\alpha} \tag{3.31}$$

$$c(\xi) \ = c^A \ + \xi(c^M - c^A) \ = c^A + \xi\Delta c \tag{3.32}$$

$$s_0(\xi) = s_0^A + \xi(s_0^M - s_0^A) \ = s_0^A + \xi\Delta s_0 \tag{3.33}$$

$$u_0(\xi) = u_0^A + \xi(u_0^M - u_0^A) \ = u_0^A + \xi\Delta u_0 \tag{3.34}$$

A smooth hardening function $f(\xi)$ is proposed in equation (4.11) to account for the hardening effects in polycrystalline SMAs, such as the plastic strain accumulation after the training procedure, imperfections located at the grain boundary, and nano-precipitates hardening effects, etc.[48], where three additional intermediate material parameters a_1, a_2, a_3 and four curve fitting parameters n_1, n_2, n_3, n_4 are introduced to better treat the smooth transition behaviors at the initiation and completion of phase transformation.

$$f(\xi) = \begin{cases} \dfrac{1}{2}a_1\left(\xi + \frac{\xi^{n_1+1}}{n_1+1} + \frac{(1-\xi)^{n_2+1}}{n_2+1}\right) + a_3\xi \ , \ \dot{\xi} > 0, \\ \dfrac{1}{2}a_2\left(\xi + \frac{\xi^{n_3+1}}{n_3+1} + \frac{(1-\xi)^{n_4+1}}{n_4+1}\right) - a_3\xi \ , \ \dot{\xi} < 0 \end{cases} \tag{3.35}$$

following the standard Coleman-Noll procedure described in section 3.3, the explicit form for constitutive relation (3.26) between stress and strain is derived as follows. Note that

the nonlinearity in this constitutive relation is implied by the transformation strain $\mathbf{h}^{tr}$.

$$\mathbf{h} = -\rho_0 \frac{\partial G}{\partial \boldsymbol{\tau}} = \mathcal{S}\boldsymbol{\tau} + \boldsymbol{\alpha}(T - T_0) + \mathbf{h}^{tr} \tag{3.36}$$

the explicit form for constitutive relation (3.27) between entropy s and temperature T can also be derived as,

$$s = -\rho_0 \frac{\partial G}{\partial T} = \frac{1}{\rho_0}\boldsymbol{\tau} : \boldsymbol{\alpha} + c\ln(\frac{T}{T_0}) + s_0 \tag{3.37}$$

the reduced form of the dissipation inequality (3.28) can be rewritten in terms of the chosen internal state variables $\boldsymbol{\Upsilon} = \{\xi, \mathbf{h}^{tr}\}$ as,

$$-\rho_0 \frac{\partial G}{\partial \mathbf{h}^{tr}} : \mathring{\mathbf{h}}^{tr} - \rho_0 \frac{\partial G}{\partial \xi}\dot{\xi} \geqslant 0 \tag{3.38}$$

3.3.2.2 Evolution equation of internal state variables

The evolution equation for the internal state variables $\boldsymbol{\Upsilon} = \{\xi, \mathbf{h}^{tr}\}$ is presented here. It is proposed that the logarithmic rate of the transformation strain $\mathbf{h}^{tr}$ is proportional to the rate change of the martensitic volume fraction ξ. This proportional evolution rule is adopted by following the principle of maximum dissipation such that among all the admissible thermodynamic paths, the one dissipating the most energy is chosen during the SMAs phase transformation process [79]. The idea of maximum dissipation for inelastic materials is not new, it was also widely employed for plastic deformed materials to derive the associated flow rule [34]. It is worth pointing out that the rate applied on the transformation strain is the logarithmic rate rather than the conventional time rate. The explicit

evolution rule is as follows,

$$\mathring{\mathbf{h}}^{tr} = \mathbf{\Lambda}\dot{\xi}, \;\; \mathbf{\Lambda} = \begin{cases} \mathbf{\Lambda}^{fwd}, \;\; \dot{\xi} > 0, \\ \\ \mathbf{\Lambda}^{rev}, \;\; \dot{\xi} < 0, \end{cases} \tag{3.39}$$

where $\mathbf{\Lambda}^{fwd}$ is called the forward transformation direction tensor and $\mathbf{\Lambda}^{rev}$ is called the reverse transformation direction tensor. They are defined as,

$$\mathbf{\Lambda}^{fwd} = \frac{3}{2} H^{cur} \frac{\boldsymbol{\tau}^{'}}{\bar{\boldsymbol{\tau}}}, \;\; \mathbf{\Lambda}^{rev} = \frac{\mathbf{h}^{t\text{-}r}}{\xi^{r}}. \tag{3.40}$$

in which, $\boldsymbol{\tau}^{'}$ is the deviatoric part of Kirchhoff stress tensor calculated by $\boldsymbol{\tau}^{'} = \boldsymbol{\tau} - \frac{1}{3}\text{tr}(\boldsymbol{\tau})\ \mathbf{1}$, $\mathbf{1}$ is the second order identity tensor. The effective Mises equivalent stress is given by $\bar{\boldsymbol{\tau}} = \sqrt{\frac{3}{2}\boldsymbol{\tau}^{'} : \boldsymbol{\tau}^{'}}$. $\mathbf{h}^{tr\text{-}r}$ and ξ^{r} represent the transformation strain value and martensitic volume fraction at the reverse transformation starting point. It is common among available SMA models that the magnitude of the inelastic recoverable transformation strain is the same for full transformation under any applied stress levels. This is true when the stress levels is high enough to generate maximum oriented martensitic variants. However, if the applied stress level is not sufficiently high, self-accommodated martensitic variants will be generated. This renders the value of transformation strain less than it is in the high stress level case (i.e., the stress dependency of the magnitude of the transformation strain). Therefore, an exponential function H^{cur} dependent on current stress levels is introduced to calculate the current transformation strain as shown in equation (4.19), where H^{max} is the maximum (or saturated) transformation strain and k_t is a curve fitting material parameter.

$$H^{cur}(\boldsymbol{\tau}) = H^{max}(1 - e^{-k_t \bar{\boldsymbol{\tau}}}) \tag{3.41}$$

3.3.2.3 Transformation function

The objective in this part is to define a proper transformation criterion to determine the occurrence of the phase transformation. Recall the reduced form for dissipation energy is given by inequility (3.38) and the relation between $\mathbf{h}^{tr}$ and ξ is defined through evolution equation (4.15). Substituting evolution equation (4.15) into reduced form dissipation inequality (3.38), the following equation is obtained,

$$(\boldsymbol{\tau} : \boldsymbol{\Lambda} - \rho_0 \frac{\partial G}{\partial \xi})\dot{\xi} = \pi \dot{\xi} \geqslant 0 \tag{3.42}$$

the above equation implies that all the dissipation energy is directly a result of the change in the martensitic volume fraction. Based upon this, a scalar variable π, called the thermodynamic driving force conjugated to the martensitic volume fraction ξ, can thus be defined. Substitution of Gibbs free energy potential G in equation (3.29) into equation (3.42) yields the explicit expression for π as follows,

$$\begin{aligned} \pi(\boldsymbol{\tau}, T, \xi) = \boldsymbol{\tau} : \boldsymbol{\Lambda} + \frac{1}{2}\boldsymbol{\tau} : \Delta\mathcal{S}\boldsymbol{\tau} + \boldsymbol{\tau} : \Delta\boldsymbol{\alpha}(T - T_0) - \rho_0 \Delta c \big[T - T_0 \\ - T\ln(\frac{T}{T_0})\big] + \rho_0 \Delta s_0 T - \rho_0 \Delta u_0 - \frac{\partial f(\xi)}{\partial \xi} \end{aligned} \tag{3.43}$$

where $\Delta\mathcal{S}, \Delta\alpha, \Delta c, \Delta s_0$, and Δu_0 are the phase differences on compliance tensor, thermal expansion tensor, specific heat, reference entropy and reference internal energy, respectively. It can be observed that the thermodynamic driving force π is a function of Kirchhoff stress $\boldsymbol{\tau}$, temperature T and martenstic volume fraction ξ. This indicates that the phase transformation process can be activated by two independent sources, namely either the stress or temperature, which correlates quite well with the experimentally observed stress-induced and thermally-induced phase transformations in SMAs. To proceed to the goal of defining a transformation criteria, it is assumed that whenever the thermo-

dynamic driving force π reaches a critical value Y $(-Y)$, the forward (reverse) phase transformation takes place. Therefore a transformation function Φ can be defined as the transformation criteria to determine the transformation occurrence as follows,

$$\Phi = \begin{cases} \pi - Y, \ \dot{\xi} > 0, \\ \\ -\pi - Y, \ \dot{\xi} < 0, \end{cases} \tag{3.44}$$

In the infinitesimal strain theory based SMA model [47], a reference critical value Y_0 and an additional parameter D were introduced into Y, through which the thermodynamical critical value Y becomes a function dependent on applied stress levels, see in equation (3.45). Such treatment let the model consider the effect of applied stress levels on the size of hysteresis loop. This capability is provided through capturing the different slopes C_A, C_M in the effective stress-temperature phase diagram. The explicit derivation is provided from equation (4.44) to equation (3.72) at the model calibration part in 3.5.

$$Y(\boldsymbol{\tau}) = \begin{cases} Y_0 + D\boldsymbol{\tau} : \boldsymbol{\Lambda}^{fwd}, \ \dot{\xi} > 0, \\ \\ Y_0 + D\boldsymbol{\tau} : \boldsymbol{\Lambda}^{rev}, \ \dot{\xi} < 0, \end{cases} \tag{3.45}$$

As a consequence of the application of the principle of maximum dissipation [79], the so-called Kuhn-Tucker constraints are placed on the proposed model, which are stated as follows for the forward and reverse cases respectively,

$$\begin{aligned} &\dot{\xi} \geqslant 0; \quad \Phi(\boldsymbol{\tau}, T, \xi) = \ \ \pi - Y \leqslant 0; \quad \Phi\dot{\xi} = 0; \quad (\mathbf{A} \Rightarrow \mathbf{M}) \\ &\dot{\xi} \leqslant 0; \quad \Phi(\boldsymbol{\tau}, T, \xi) = -\pi - Y \leqslant 0; \quad \Phi\dot{\xi} = 0; \quad (\mathbf{M} \Rightarrow \mathbf{A}) \end{aligned} \tag{3.46}$$

3.3.3 Consistent tangent stiffness and thermal matrix

In this section, a detailed derivation of the consistent tangent stiffness matrix and the thermal matrix is provided to complete the proposed model. For most typical displacement-based finite element softwares, such as Abaqus, the consistent tangent matrices are often required to be provided in the UMAT so that the finite element solver can achieve a fast convergence for the global equilibrium equations. Normally, consistent tangent matrices can be expressed in the rate form shown in equation (4.33), where $\mathcal{L}$ is called the consistent tangent stiffness matrix and Θ is the consistent thermal matrix.

$$\mathring{\boldsymbol{\tau}} = \mathcal{L}\mathring{\mathbf{h}} + \Theta\dot{T} \tag{3.47}$$

applying the logarithmic rate on constitutive equation (4.12) yields,

$$\mathring{\boldsymbol{\tau}} = \mathcal{C}\,[\mathring{\mathbf{h}} - \boldsymbol{\alpha}\dot{T} - (\Delta\mathcal{S}\boldsymbol{\tau} + \Delta\boldsymbol{\alpha}(T - T_0) + \boldsymbol{\Lambda})\dot{\xi}\,] \tag{3.48}$$

taking chain rule differentiation on the transformation function equation (4.30) gives,

$$\dot{\Phi} = \partial_{\boldsymbol{\tau}}\Phi : \mathring{\boldsymbol{\tau}} + \partial_T\Phi\dot{T} + \partial_\xi\Phi\dot{\xi} = 0 \tag{3.49}$$

substituting equation (4.34) back into equation (4.35) to eliminate $\mathring{\boldsymbol{\tau}}$ and solving it for $\dot{\xi}$, the following expression for $\dot{\xi}$ can be obtained,

$$\dot{\xi} = -\frac{\partial_{\boldsymbol{\tau}}\Phi : \mathcal{C}\mathring{\mathbf{h}} + (\partial_T\Phi - \partial_{\boldsymbol{\tau}}\Phi : \mathcal{C}\boldsymbol{\alpha})\dot{T}}{\partial_\xi\Phi - \partial_{\boldsymbol{\tau}}\Phi : \mathcal{C}(\Delta\boldsymbol{S}\boldsymbol{\tau} + \boldsymbol{\Lambda} + \Delta\boldsymbol{\alpha}(T - T_0))} \tag{3.50}$$

substituting equation(4.36) back into the rate form constitutive equation(4.34) to eliminate $\dot{\xi}$, considering the phase difference of the thermal expansion coefficients can be ignored for martensite and austenite phase, the final explicit expression corresponding to equation

(4.33) can be obtained as follows,

$$\mathring{\boldsymbol{\tau}} = \Big[\mathcal{C} + \frac{[\mathcal{C}(\Delta\mathcal{S}\boldsymbol{\tau} + \boldsymbol{\Lambda})] \otimes [\mathcal{C}\partial_{\boldsymbol{\tau}}\Phi]}{\partial_{\xi}\Phi - \partial_{\boldsymbol{\tau}}\Phi : \mathcal{C}(\Delta\mathcal{S}\boldsymbol{\tau} + \boldsymbol{\Lambda})}\Big]\mathring{\mathbf{h}} + \Big[-\mathcal{C}\boldsymbol{\alpha} + \frac{\mathcal{C}(\Delta\mathcal{S}\boldsymbol{\tau} + \boldsymbol{\Lambda})(\partial_T\Phi - \partial_{\boldsymbol{\tau}}\Phi : \mathcal{C}\boldsymbol{\alpha})}{\partial_{\xi}\Phi - \partial_{\boldsymbol{\tau}}\Phi : \mathcal{C}(\Delta\mathcal{S}\boldsymbol{\tau} + \boldsymbol{\Lambda})}\Big]\dot{T} \tag{3.51}$$

in which the consistent tangent stiffness matrix $\mathcal{L}$ is,

$$\mathcal{L} = \mathcal{C} + \frac{[\mathcal{C}(\Delta\mathcal{S}\boldsymbol{\tau} + \boldsymbol{\Lambda}] \otimes [\mathcal{C}\partial_{\boldsymbol{\tau}}\Phi]}{\partial_{\xi}\Phi - \partial_{\boldsymbol{\tau}}\Phi : \mathcal{C}(\Delta\mathcal{S}\boldsymbol{\tau} + \boldsymbol{\Lambda})} \tag{3.52}$$

and the consistent thermal matrix Θ is,

$$\Theta = -\mathcal{C}\boldsymbol{\alpha} + \frac{\mathcal{C}(\Delta\mathcal{S}\boldsymbol{\tau} + \boldsymbol{\Lambda})(\partial_T\Phi - \partial_{\boldsymbol{\tau}}\Phi : \mathcal{C}\boldsymbol{\alpha})}{\partial_{\xi}\Phi - \partial_{\boldsymbol{\tau}}\Phi : \mathcal{C}(\Delta\mathcal{S}\boldsymbol{\tau} + \boldsymbol{\Lambda})} \tag{3.53}$$

In order to fully determine the explicit values for $\mathcal{L}$ and Θ during the implementation section for the proposed model, the explicit expressions of the following terms $\partial_{\boldsymbol{\tau}}\Phi$, $\partial_{\xi}\Phi$, $\partial_T\Phi$ used in above equations are derived in Appendix B.

3.4 Numerical implementation

This section focuses on the implementation of the proposed model within finite element (FE) solvers to solve boundary value problems (BVPs). The implementation flowchart is shown in Figure 4.3. While typically stress and strain information are provided from FE solver, the initial input information used in this model are only the temperatures $T_n,\ \Delta T_n$ and deformation gradients at current step $\mathbf{F}_n$ and next step $\mathbf{F}_{n+1}$. The reason for using only these information is that other tensorial variables have been rotated by the finite element (FE) solver before they are used as inputs, in which the rotation tensor is calculated based on the other non-integrable objective rates. This consequently leads to the artificial stress errors described in section 3.1. During the implementation for the proposed model, a pre-calculation and a rotation procedure are employed before calling the main

UMAT subroutine. In the pre-calculation procedure, the logarithmic strain at current step $\mathbf{h}_n$ and next step $\mathbf{h}_{n+1}$ are calculated based on $\mathbf{F}_n$ and $\mathbf{F}_{n+1}$. The incremental rotation tensor $\Delta\mathbf{R}_n^{log}$ based on the logarithmic rate can be calculated by using the exponential map scheme [90, 68, 127]. In the rotation procedure, tensorial variables including $\mathbf{h}_n$, $\mathbf{h}_n^{tr}$ and $\mathbf{\Lambda}_n$ are rotated from step n configuration to the new configuration at step $n+1$ by using the obtained $\Delta\mathbf{R}_n^{log}$, thus, the so-called principle of objectivity is preserved.

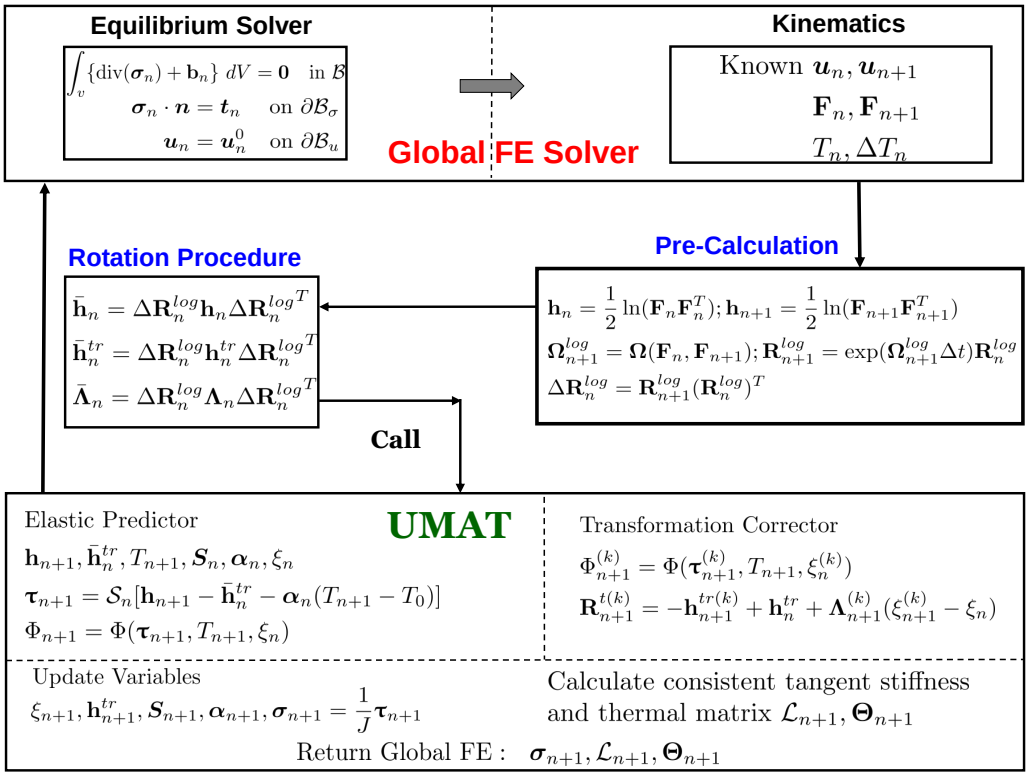

Figure 3.1: Flowchart for the used variables in the proposed model and the UMAT integration with the global FE solver (from Figure 1 of [121], © 2019 by IOP Publishing, with permission of IOP Publishing, DOI:10.1088/1361-665x/ab1acb).

The rest of implementation procedure consists of two steps, the first step is called the thermoelastic predictor and the second step is called the transformation corrector. During the initialization of thermoelastic step, the total strain $\mathbf{h}_{n+1}$ and current temperature $T_{n+1} = T_n + \Delta T_n$ are provided. The initial internal state variables $\boldsymbol{\Upsilon}_{n+1}^{(0)}$ are assumed to be the same as $\boldsymbol{\Upsilon}_n$ for the initial Kuhn-Tucker consistency checking, i.e., $\Phi_{n+1}^{(0)} \leqslant 0$. If the initial value of $\Phi_{n+1}^{(0)}$ satisfies the consistency checking, the n+1 step is detected as a thermoelastic response and the UMAT returns to global FE solver for next increment. In case of consistency condition violated, the second step called the transformation corrector is activated to find the updated internal state variables $\boldsymbol{\Upsilon}_{n+1}^{(k)}$ in order to regain the Kuhn-Tucker consistency. A detailed summary for the implementation procedure is listed in the table 3.1.

3.4.1 Thermoelastic prediction

Take the $(n+1)^{th}$ step as an example to go through the thermoelastic prediction process. The total strain tensor $\mathbf{h}_{n+1}$ and the temperature T_{n+1} are provided from Pre-Calculation procedure, and the initial internal state variables $\boldsymbol{\Upsilon}_{n+1}^{(0)}$ are assumed the same as $\boldsymbol{\Upsilon}_n$,

$$\mathbf{h}_{n+1}^{tr(0)} = \mathbf{h}_n^{tr}; \quad \xi_{n+1}^{(0)} = \xi_n \tag{3.54}$$

Based on equation (4.45), the initial guess for Kirchhoff stress $\boldsymbol{\tau}_{n+1}^{(0)}$ can be calculated through the constitutive equation (4.46). Here the integer in the upper parenthesis represents that how many iterations have been done during the transformation correction procedure, and integer zero means that this step is just an initial guess in the thermoelastic procedure. The initial calculation for stress $\boldsymbol{\tau}_{n+1}^{(0)}$ can be obtained,

$$\boldsymbol{\tau}_{n+1}^{(0)} = \mathcal{C}_n\Big[\mathbf{h}_{n+1} - \mathbf{h}_{n+1}^{tr(0)} - \boldsymbol{\alpha}_{n+1}^{(0)}(T_{n+1} - T_0)\Big] \tag{3.55}$$

Table 3.1: The implementation procedure for the proposed finite strain SMA model, reprinted with permission from [121].

1.*Initialization*

- Conduct pre-calculation and rotation procedures.
- $k = 0; \xi_{n+1}^{(0)} = \xi_n; \boldsymbol{h}_{n+1}^{tr(0)} = \boldsymbol{h}_n^{tr};$

2.*Thermoelastic Predictor*

- $\boldsymbol{\tau}_{n+1}^{(0)} = \mathcal{C}_{n+1}^{(0)}[\boldsymbol{h}_{n+1} - \boldsymbol{h}_{n+1}^{tr(0)} - \boldsymbol{\alpha}(T_{n+1} - T_0)]$
- Calculate $\Phi_{n+1}^{(k)}$.
- IF $\Phi_{n+1}^{(0)} \leqslant tol$, GOTO 4 (thermoelastic response).
- IF $\Phi_{n+1}^{(0)} > tol$, GOTO 3 (transformation happens).

3.*Transformation Corrector*

- Calculate residual matrix

  $\mathbf{R}_{n+1}^{tr(k)} = -\boldsymbol{h}_{n+1}^{tr(k)} + \boldsymbol{h}_n^{tr} + \boldsymbol{\Lambda}_{n+1}^{(k)}(\xi_{n+1}^{(k)} - \xi_n)$

  $\Phi_{n+1}^{(k)} \quad = \Phi(\boldsymbol{\tau}_{n+1}^{(k)}, T_{n+1}, \xi_{n+1}^{(k)})$
- Perform the Newton-Raphson iterations in equation (4.52).
- Update variables $\xi_{n+1}^{(k+1)}, \boldsymbol{h}_{n+1}^{tr(k+1)}, \mathcal{S}_{n+1}^{(k+1)}$

  $\xi_{n+1}^{(k+1)} \quad = \xi_{n+1}^{(k)} + \Delta\xi_{n+1}^{(k+1)}$

  $\boldsymbol{h}_{n+1}^{tr(k+1)} \; = \boldsymbol{h}_{n+1}^{tr(k)} + \Delta\boldsymbol{h}_{n+1}^{tr(k+1)}$

  $\mathcal{S}_{n+1}^{(k+1)} \quad = \mathcal{S}^A + \xi_{n+1}^{(k+1)}\Delta\mathcal{S}$
- IF $\Phi_{n+1}^{(k+1)} \geqslant tol$, GOTO step 3 for the next local iteration, $k = k + 1$.

  ELSE GOTO step 4

4.*Calculate consistent stiffness matrix $\mathcal{L}$ and thermal matrix $\boldsymbol{\Theta}$.*

- $\mathcal{L} = \mathcal{C} + \dfrac{[\mathcal{C}(\Delta\mathcal{S}\boldsymbol{\tau} + \boldsymbol{\Lambda}] \otimes [\mathcal{C}\partial_{\boldsymbol{\tau}}\Phi]}{\partial_\xi\Phi - \partial_{\boldsymbol{\tau}}\Phi : \mathcal{C}(\Delta\mathcal{S}\boldsymbol{\tau} + \boldsymbol{\Lambda})}$
- $\Theta = -\mathcal{C}\boldsymbol{\alpha} + \dfrac{\mathcal{C}(\Delta\mathcal{S}\boldsymbol{\tau} + \boldsymbol{\Lambda})(\partial_T\Phi - \partial_{\boldsymbol{\tau}}\Phi : \mathcal{C}\boldsymbol{\alpha})}{\partial_\xi\Phi - \partial_{\boldsymbol{\tau}}\Phi : \mathcal{C}(\Delta\mathcal{S}\boldsymbol{\tau} + \boldsymbol{\Lambda})}$

5.Exit UMAT and proceed to the global FE solver for the next increment

---

After the calculation of $\boldsymbol{\tau}_{n+1}^{(0)}$, the value of transformation function $\Phi_{n+1}^{(0)}$ can be evaluated based on equations (4.29) and (4.30) for the initial Kuhn-Tucker consistency checking,

$$\Phi_{n+1}^{(0)} = \Phi(\boldsymbol{\tau}_{n+1}^{(0)}, T_{n+1}, \boldsymbol{\Upsilon}_{n+1}^{(0)}) \tag{3.56}$$

If the calculated value of transformation function $\Phi_{n+1}^{(0)}$ remains under the transformation surface (i.e., $\Phi_{n+1}^{(0)} \leqslant$ 'tol', 'tol' is usually set to be 10^{-6}), step n+1 is detected as a thermoelastic response. Therefore the values of current state variables $\boldsymbol{\tau}_{n+1}^{(0)}$ and $\boldsymbol{\Upsilon}_{n+1}^{(0)}$ are accepted as correct and the UMAT proceeds to the global FE solver for the next increment. In case the transformation surface is violated (i.e. $\Phi_{n+1}^{(0)} \geqslant$ tol), the transformation corrector step is activated to find the updated state variables until the consistency equation (4.32) is preserved.

3.4.2 Transformation correction

This part addresses the iterative procedures required for the transformation corrector to restore the Kuhn-Tucker consistency. In general, the transformation corrector is nothing but a set of Newton-Raphson iterations on equations (4.49) and (4.50) to find the updated internal state variables. Take the k^{th} local iteration for example, the corrector is activated to find a set of $\boldsymbol{\Upsilon}_{n+1}^{(k)}$ which makes the residual terms $\mathbf{R}_{n+1}^{tr(k)}$ in equation (4.49) and transformation function $\Phi_{n+1}^{(k)}$ in equation (4.50) less than 'tol'.

$$\mathbf{R}_{n+1}^{tr(k)} = -\mathbf{h}_{n+1}^{tr(k)} + \mathbf{h}_{n}^{tr} + \boldsymbol{\Lambda}_{n+1}^{(k)}(\xi_{n+1}^{(k)} - \xi_n) \tag{3.57}$$

$$\Phi_{n+1}^{(k)} \ = \Phi(\boldsymbol{\tau}_{n+1}^{(k)}, T_{n+1}, \xi_{n+1}^{(k)}) \tag{3.58}$$

This objective is equivalent to the following convergence conditions,

$$|\xi_{n+1}^{(k+1)} - \xi_{n+1}^{(k)}| \leqslant \text{tol} \ ; \ |\mathbf{h}_{n+1}^{tr(k+1)} - \mathbf{h}_{n+1}^{tr(k)}| \leqslant \text{tol} \tag{3.59}$$

Use the standard Newton-Raphson procedure [2] to solve equations (4.49) and (4.50),

$$\begin{bmatrix} \Delta\xi_{n+1}^{(k+1)} \\ \Delta\mathbf{h}_{n+1}^{tr(k+1)} \end{bmatrix} = - \begin{bmatrix} \dfrac{\partial\Phi_{n+1}^{(k)}}{\partial\xi} & \dfrac{\partial\Phi_{n+1}^{(k)}}{\partial\mathbf{h}^{tr}} \\ \dfrac{\partial\mathbf{R}_{n+1}^{tr(k)}}{\partial\xi} & \dfrac{\partial\mathbf{R}_{n+1}^{tr(k)}}{\partial\mathbf{h}^{tr}} \end{bmatrix}^{-1} \begin{bmatrix} \Phi_{n+1}^{(k)} \\ \mathbf{R}_{n+1}^{tr(k)} \end{bmatrix} \tag{3.60}$$

The following results on internal state variables at $(k+1)^{th}$ iteration can be obtained,

$$\begin{bmatrix} \xi_{n+1}^{(k+1)} \\ \mathbf{h}_{n+1}^{tr(k+1)} \end{bmatrix} = \begin{bmatrix} \xi_{n+1}^{(k)} \\ \mathbf{h}_{n+1}^{tr(k)} \end{bmatrix} + \begin{bmatrix} \Delta\xi_{n+1}^{(k+1)} \\ \Delta\mathbf{h}_{n+1}^{tr(k+1)} \end{bmatrix} \tag{3.61}$$

Once the converged values of $\{\mathbf{h}_{n+1}^{tr(k+1)}, \xi_{n+1}^{(k+1)}\}$ are found, the current transformation corrector step is labeled as finished and the UMAT proceeds to the next increment. Otherwise the Newton-Raphson procedure exits at this step after certain number of iterations and the current finite element increment step stops.

3.5 Calibration of the material parameters

In this section, the material parameters utilized in the proposed model are identified from a set of one-dimensional experimental data. Note that the strain measure used here should be in the true (or logarithmic) scale rather than the engineering (or infinitesimal)

[2] The explicit expression for the Jacobian matrix during this Newton-Raphson iteration in equation (4.52) is quite complicated. The symbolic calculation tool in MATLAB is used here to find the Jacobian matrix, and the authors suggest interested readers to utilize this method to perform the tedious calculation.

scale. Material parameters used in the proposed model can be categorized into three groups, *i.e.* the key material parameters, smooth hardening parameters and intermediate parameters. First, the material constants such as elastic modulus E_A, E_M, Poisson's ratios ν_A and ν_B, the thermal expansion tensors $\boldsymbol{\alpha}_A$ and $\boldsymbol{\alpha}_M$, stress influenced coefficients C_A and C_M from the phase diagram (or called clausius clapeyron coefficient), critical phase transformation temperatures A_s, A_f, M_s, M_f at stress free state are determined. Secondly, the hardening parameters describing the smooth transition feature are discussed. Finally, the intermediate parameters are derived based on the aforementioned two parameter groups. All the material parameters used in this model are summarized in table 3.2.

Because the data is provided in one-dimensional case, all tensorial variables of the proposed model have to be reduced into 1-D scalar value. For example, the stress tensor is reduced as $\boldsymbol{\tau} \rightarrow \tau_{11} = \tau$; logarithmic strain tensor is reduced as $\mathbf{h} \rightarrow h_{11} = h$, *etc*. Constitutive equation (4.12) can be rewritten as one dimensional form as follows,

$$\tau = E[h - \alpha(T - T_0) - h^{tr}] \tag{3.62}$$

where the effective elastic modulus E is calculated by using the rule of mixture as follows,

$$E = [1/E^A + \xi(1/E^M - 1/E^A)] \tag{3.63}$$

The evolution equation (4.15) is also reduced in one-dimensional form as,

$$\Lambda = \Lambda_{11} = \begin{cases} H^{cur}(\sigma)\ \text{sgn}(\tau) & ;\dot{\xi} > 0, \\ \dfrac{h^{t-r}}{\xi^r} & ;\dot{\xi} < 0, \end{cases} \tag{3.64}$$

the thermodynamic driving force π in one-dimensional case can thus be obtained,

$$\pi = \tau\Lambda + \frac{1}{2}\Delta\mathcal{S}\tau^2 + \tau\Delta\alpha(T - T_0) + \rho_0\Delta s_0 T - \rho_0\Delta c\big[T - T_0 - T\ln(\frac{T}{T_0})\big] \\ -\rho\Delta u_0 - \frac{\partial f}{\partial \xi} \tag{3.65}$$

the transformation function in one-dimensional form can be calculated based on equation (3.65). Considering the phase difference for the thermal expansion $\Delta\alpha$ and specific heat Δc are small enough to be ignored, the following transformation functions for the forward case and the reverse case can be obtained respectively,

$$\Phi_{fwd}(\tau, T, \xi) = \big[\tau\Lambda + \frac{1}{2}\Delta\mathcal{S}\tau^2 + \rho_0\Delta s_0 T - \rho_0\Delta u_0 - \frac{\partial f}{\partial \xi}\big] - Y = 0 \tag{3.66}$$

$$\Phi_{rev}(\tau, T, \xi) = -\big[\tau\Lambda + \frac{1}{2}\Delta\mathcal{S}\tau^2 + \rho_0\Delta s_0 T - \rho_0\Delta u_0 - \frac{\partial f}{\partial \xi}\big] - Y = 0 \tag{3.67}$$

As described in the first paragraph of this section, there are three sets of material parameters that need to be identified. First, material constants $(E_A, E_M, \nu_A, \nu_M, \alpha_A, \alpha_M)$ are considered. Elastic modulus E_A, E_M can be determined through a pseudoelastic stress and strain curve by calculating the slopes at martensitic phase and austenite phase. Poisson's ratio is attained using a widely accepted value of $\nu_A = \nu_M = 0.33$ found in [47]. The thermal expansion coefficient are usually considered as $\alpha_A = \alpha_M$, which can be calibrated through an isobaric actuation experiment. The maximum transformation strain H^{max} can be determined from the pseudoelastic experimental and the value of parameter k_t are chosen to best fit the H^{cur} curve. The stress influence coefficients and the critical phase transformation temperatures $(C_A, C_M, M_s, M_f, A_s, A_f)$ can be calibrated through the phase diagram. Second, the material parameters related to the smooth hardening features are discussed. The Coefficients (n_1, n_2, n_3, n_4) without specific physical meanings are determined to best match the smoothness in corners of material response. Lastly, there

are seven intermediate material parameters $(\rho_0\Delta s_0, \rho_0\Delta u_0, a_1, a_2, a_3, Y_0, D)$ that need to be calculated to complete the model. Determination of such intermediate parameters requires a set of seven algebraic equations. The needed four equations come from transformation constraints as the Kuhn-Tucker condition Equation.4.32 (i.e. $\Phi_{rev}(\tau, T, \xi) = 0$). The fifth equation comes from the continuity of Gibbs free energy at the end of the forward transformation $(\xi = 1)$. The needed five algebraic equations are summarized as follows, The above five algebraic equations yield the following expression for the five out of seven intermediate model parameters,

$$\begin{aligned} a_1 &= \rho_0\Delta s_0(M_f - M_s); \quad a_2 = \rho_0\Delta s_0(A_s - A_f) \\ a_3 &= \frac{1}{4}\, a_2(1 + \frac{1}{n_3 + 1}) - \frac{1}{4}\, a_1(1 + \frac{1}{n_1 + 1}) \\ \rho_0\Delta u_0 &= \frac{1}{2}\rho\Delta s_0(M_s + A_f) \\ Y_0 &= \frac{1}{2}\rho_0\Delta s_0(M_s - A_f) - a_3 \end{aligned} \tag{3.68}$$

Another two equations are derived from the Kuhn-Tucker condition in order to complete the calculation. For a one-dimensional uniaxial experiment, the Kuhn-Tucker condition (4.32) requires equation (3.69) to hold true at any specific stress level τ^*,

$$\mathrm{d}\Phi = \partial_\tau\Phi\ \mathrm{d}\tau + \partial_T\Phi\ \mathrm{d}T + \partial_\xi\Phi\ \mathrm{d}\xi = 0 \tag{3.69}$$

Evaluate $\mathrm{d}\Phi$ at the start point of the forward phase transformation (i.e. $\xi = 0$), and at the finish point of the forward phase transformation (i.e. $\xi = 1$), the incremental part of martensitic volume fraction should be zero (i.e. $\mathrm{d}\xi = 0$) in both of the aforementioned cases. Therefore, the relationships between the stress temperature coefficients C_M, C_A and the stress temperature slopes $\frac{\mathrm{d}\tau}{\mathrm{d}T}$ can be obtained.

For the forward transformation case, $\dot{\xi} > 0$,

$$C_M = \frac{\mathrm{d}\tau}{\mathrm{d}T}\Big|_{\tau^*,\dot{\xi}>0} = \frac{-\rho\Delta s_0}{\Lambda + \tau : \partial_\tau \Lambda + \Delta\mathcal{S}\tau - \partial_\tau Y}\Big|_{\tau^*} \tag{3.70}$$

For the reverse transformation case, $\dot{\xi} < 0$

$$C_A = \frac{\mathrm{d}\tau}{\mathrm{d}T}\Big|_{\tau^*,\dot{\xi}<0} = \frac{-\rho\Delta s_0}{\Lambda + \tau : \partial_\tau \Lambda + \Delta\mathcal{S}\tau + \partial_\tau Y}\Big|_{\tau^*} \tag{3.71}$$

Using the equations (3.70) and (3.71), the rest two intermediate material parameters $\rho_0\Delta s_0$ and D can thus be expressed as follows,

$$D = \frac{(C_M - C_A)\big[H^{cur} + \tau\partial_\tau H^{cur} + \tau\Delta\mathcal{S}\big]}{(C_M + C_A)(H^{cur} + \tau\partial_\tau H^{cur})} \tag{3.72}$$

$$\rho_0\Delta s_0 = -\frac{2C_M C_A\big[H^{cur} + \tau\partial_\tau H^{cur} + \tau\Delta\mathcal{S}\big]}{C_M + C_A} \tag{3.73}$$

3.6 Numerical results

In this section, the proposed model is used to predict the stress/thermally-induced phase transformations in SMAs subjected to general three-dimensional thermo-mechanical loading. Several numerical examples are presented here to test the capabilities of this model to account for large strains and rotations, and also to resolve the artificial stress errors issue. First, a parametric analysis on a uniaxial SMA bar is studied to show that the proposed model is able to consider the geometry nonlinearity induced by large strains. Second, two BVPs, i.e., an SMA beam and an SMA torque tube subjected to stress-induced phase transformations, are tested as large rotation cases. To show the model is able to resolve the artificial stress errors issue, the cyclic response of the beam and the torque tube are obtained via the proposed model, and the results are compared against

the predictions obtained by the Abaqus nonlinear solver[3]. Next, an isobaric BVP of an SMA torque tube subjected to varying thermal loading is investigated to predict the thermally-induced phase transformation. In the end, to show the model is able to capture the non-proportional local stress and strain evolutions, a 3-D solid flexible structure undergoing a self-expanding process is studied. The proposed model is anticipated to be further validated against experimental data of NiTi and NiTiHf SMAs under uniaxial and other non-uniform loading conditions. The ultimate objective is to validate the capability of the proposed model to predict the response of SMA-based actuators, such as SMA beams and torque tubes, which are intended to be integrated with the future supersonic transport aircrafts to realize the morphing capabilities to reduce the sonic boom noise.

3.6.1 SMA bar under isothermal loading

To test the capability of the proposed model to account for the effects of large strain, an SMA prismatic bar is studied under uniaxial isothermal loading condition. A parametric study is performed with the maximum transformation strain $H^{max} = 3\%, 5\%, 8\%$ to represent three different loading cases. A group of representative material parameters (two material parameter groups combined) used in this example are listed in table 3.2 referenced from [48, 47]. The SMA prismatic bar has a length $L = 100$ (mm) and an square cross section with an edge length $a = 10$ (mm). It is subjected to a proportional force loading up to 120 (kN) then unloading to 0 (kN), the temperature is kept constant at 380K throughout the process. Generally, the load-displacement curves provided from such uniaxial experiments are interpreted into the engineering scale stress-strain curves to facilitate the model calibration. However, when the materials experience a strain that is no longer considered small, the geometry nonlinearity due to such strain has to be taken into

[3]As the nonlinear solver is activated for implicit analysis (i.e., select NLGEOM on), Abaqus automatically use the logarithmic strain as its strain measure, and the Jaumman rate is the utilized objective rate to account for the large rotation[1].

consideration. To demonstrate that the proposed model accounts for this, the calibrated values of elastic modulus (E_A, E_M) and maximum transformation strain (H^{max}) based on the true stress-strain curve are compared against the values from its infinitesimal counterpart. Three sets of load-displacement curves are generated shown in Figure 3.2. They are interpreted into stress-strain curves in two scales, i.e, the true stress (Cauchy stress) versus the true strain (logarithmic strain) curve and the engineering stress (nominal stress) versus engineering strain (infinitesimal strain) curve. By using the calibration procedure described in 3.5, the calibrated values of E_A, E_M and H^{max} summarized in table 3.3.

Table 3.3 shows that the values of E_A are identical in both the two scales. However, the values of E_M in engineering scale change from 35.48 GPa to 32.05 GPa, which indicates a material softening. Actually, such material softning is not real. Instead, it is the effect of disregarding the geometric nonlinearity induced by large strain as described previously. In this case, the geometric nonlinearity means that the bar needs to contract its cross section to compensate for its elongation to preserve the volume conservation. Disregarding the change of cross section results in an unreal decreasing on the values of E_M. By doing the calibration based on the true stress-strain curve instead of the engineering one, the proposed model is able to exclude the geometry nonlinearity induced by large strain, so that the calibrated values of E_M remain the same in the three loading cases from true scale. Besides, The values of H^{max} are also worth to be noted. Although H^{max} shows different values in the two scales, a relationship exists between the true scale H^{max} and the engineering scale H^{max}_{eng}, i.e., $H^{max} = \ln(1 + H^{max}_{\text{eng}})$. Based on the results from this parametric study, it is shown that the infinitesimal strain assumption may no longer be considered as an accurate approximation when the strain regime is beyond 3%. In order to account for the effects caused by large strain, a finite strain model to consider the geometry nonlinearity is required even in a uniaxial case.

Table 3.2: A set of representative material parameters used in the parametric study for the comparison of infinitesimal and fintie strain model, adapted from [48, 47].

Type	Parameter	Value	Parameter	Value
Key material parameters 12	E_A	60 [GPa]	C_A	8 [MPa/K]
	E_M	40 [GPa]	C_M	6 [MPa/K]
	$\nu_A = \nu_M$	0.3	M_s	333 [K]
	$\alpha_A = \alpha_M$	1.0×10^{-5} [K^{-1}]	M_f	220 [K]
	H^{max}	3%, 5%, 8%	A_s	274 [K]
	k_t	0.02	A_f	370 [K]
Smooth hardening parameters 4	n_1	0.5	n_3	0.5
	n_2	0.5	n_4	0.5

Table 3.3: Elastic modulus and transformation strain calibrated based on engineering and true scale stress-strain curves, reprinted with permission from [121].

Engineering scale	Case 1	Case 2	Case 3	True scale	Case 1	Case 2	Case 3
E_A [GPa]	60.00	60.00	60.00	E_A [GPa]	60.00	60.00	60.00
E_M[GPa]	35.48	34.06	32.05	E_M[GPa]	40.00	40.00	40.00
H^{max}_{eng}	3.04%	5.13%	8.33%	H^{max}	3.00%	5.00%	8.00%

3.6.2 SMA beam under isothermal loading

The second BVP considered here is an SMA beam subjected to isothermal loading shown in Figure 3.4. The SMA beam component has been investigated as bending actuators in [33] to realize a morphing variable-geometry chevron in order to change the outer engine shell shape to achieve specific aerodynamic characteristics. While only one loading cycle was considered in the previous study, this example examines the cyclic material and structural response. The studied beam has the same geometry as the SMA bar in section 3.6.1. Refer to Figure 3.4, the beam is simply supported with one node being fixed to suppress the rigid body motion, and the upper face is subjected to a traction that

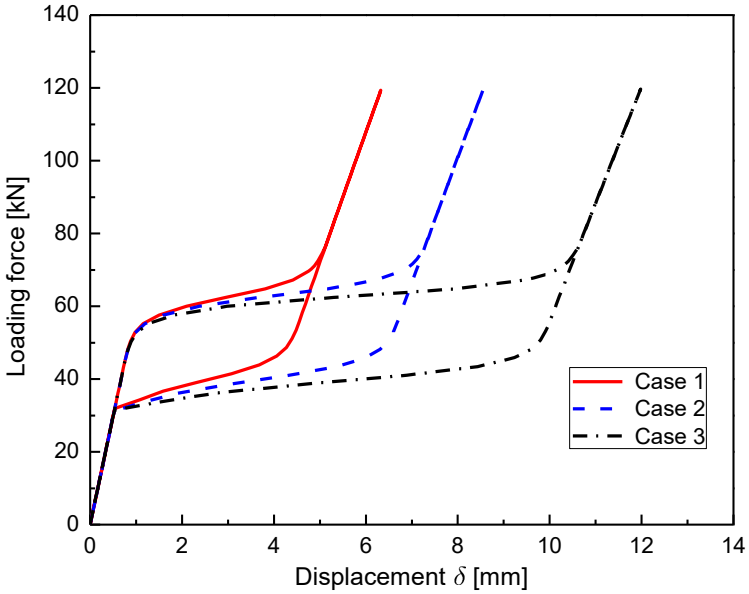

Figure 3.2: Three sets of load-displacement curves used for the calibration of material parameters for infinitesimal model and the proposed finite strain model (from Figure 2 of [121], © 2019 by IOP Publishing, with permission of IOP Publishing, DOI:10.1088/1361-665x/ab1acb).

ramps up to 24 (MPa) then decreases to 0 (MPa). Temperature is kept constant at 380K throughout the whole numerical experiment. Material parameters used in this simulation are summarized in table 3.4. The cyclic material and structural response are obtained by the proposed model for a material point p (in Figure 3.4) located at the middle bottom position, and are compared against the results obtained from the Abaqus nonlinear solver.

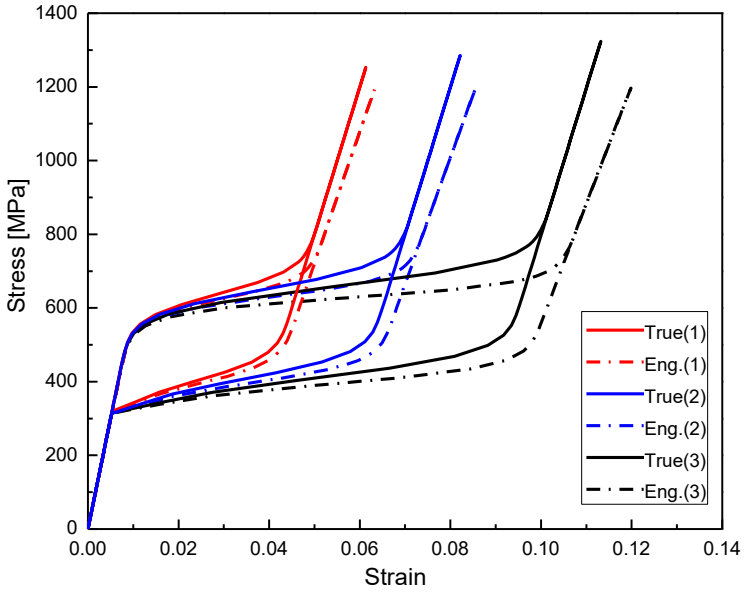

Figure 3.3: Three sets of load-displacement curves are interpreted into the engineering scale stress-strain curve for the calibration of infinitesimal model, and the true stress-strain curve for the calibration of proposed model. Engineering scale is denoted by Eng. and true scale is denoted by True (from Figure 2 of [121], © 2019 by IOP Publishing, with permission of IOP Publishing, DOI:10.1088/1361-665x/ab1acb).

Table 3.4: Calibrated material parameters for equiatomic NiTi SMA, adapted from [47].

Type	Parameter	Value	Parameter	Value
Key material parameters 12	E_A	60 [GPa]	C_A	7.8 [MPa/K]
	E_M	60 [GPa]	C_M	7.3 [MPa/K]
	$\nu_A = \nu_M$	0.3	M_s	333 [K]
	$\alpha_A = \alpha_M$	1.0×10^{-5} [K^{-1}]	M_f	220 [K]
	H^{max}	4.7%	A_s	274 [K]
	k_t	0.021	A_f	370 [K]
Smooth hardening parameters 4	n_1	0.5	n_3	0.5
	n_2	0.5	n_4	0.5

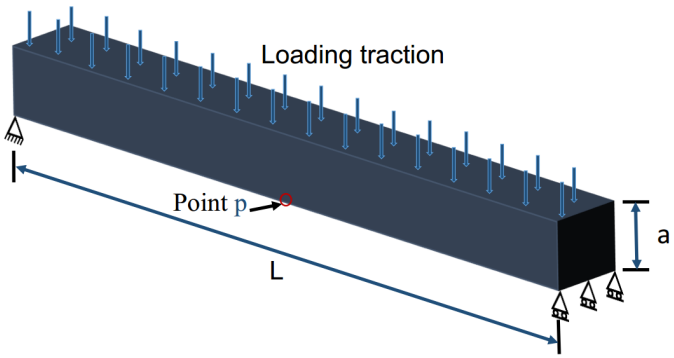

Figure 3.4: Schematic for the SMA beam subjected to isothermal bending load condition at constant temperature 306 K (from Figure 3 of [121], © 2019 by IOP Publishing, with permission of IOP Publishing, DOI:10.1088/1361-665x/ab1acb).

Figure 3.5 and Figure 3.6 show the obtained cyclic longitudinal stress-strain curve for material point p under tension. As shown in Figure 3.5, the proposed model provided a stable material response, while the Abaqus nonlinear solver predicted a shifting, instead of stable, response shown in Figure 3.6. The observation from these results indicate that the spurious material response is obtained due to the usage of non-integrable objective rates in Abaqus as discussed in the introduction. Although the initial several loading cycles are almost the same in the results provided by Abaqus nonlinear solver, the accumulation of artificially introduced stress errors, around -2 MPa for each cycle, gradually drifts the material response left downwards throughout the 100 loading cycles. In total, -200 MPa stress residuals together with -0.6% remnant strains are observed at the end. Such stress errors consist of almost 18% of the maximum stress levels experienced by material point p. As a comparison, Figure 3.7 and Figure 3.8 shows 100 stress-strain curves for another material point subjected to compression at the middle of beam upper surface. The result shows an opposite shifting trend in contrast to the results of point p. Again, a stable compressive stress-strain curve are predicted by the proposed model while the Abaqus

nonlinear solver predicts a shifting one. In addition, Figure 3.9 and Figure 3.10 shows the obtained cyclic load-displacement curves for point p. It can be seen that the proposed model predicted a stable structural response while the Abaqus nonlinear solver predicted a shifting structural response. Based on these results, it is demonstrated that the Abaqus nonlinear solver can no longer produce reliable results for the SMA beam subjected to 100 bending cycles. Therefore, the proposed model with the capability to eliminate the stress errors is required for the SMA beam subjected to cyclic loading.

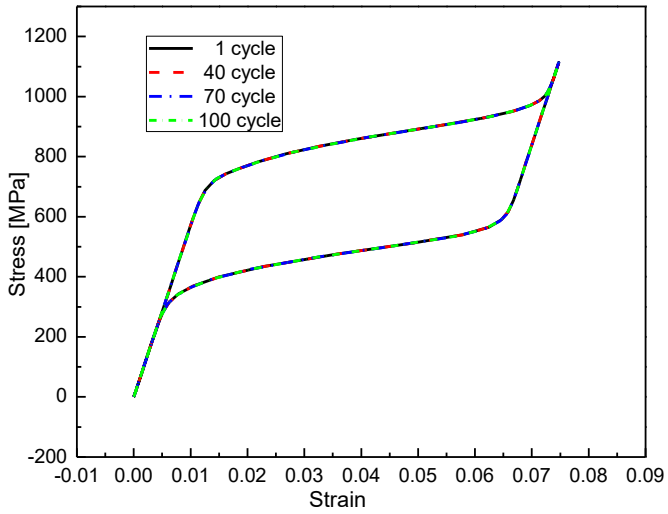

Figure 3.5: The cyclic shear stress-strain response predicted by the proposed model for a bottom surface point under isothermal loading condition (from Figure 4 of [121], © 2019 by IOP Publishing, with permission of IOP Publishing, DOI:10.1088/1361-665x/ab1acb).

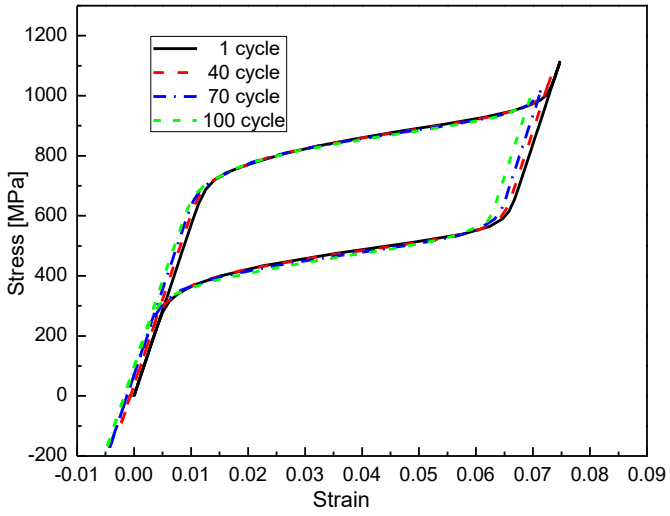

Figure 3.6: The cyclic shear stress-strain response predicted by the infinitesimal strain model using Abaqus nonlinear geometry option on for a bottom surface point under isothermal loading condition (from Figure 4 of [121], © 2019 by IOP Publishing, with permission of IOP Publishing, DOI:10.1088/1361-665x/ab1acb).

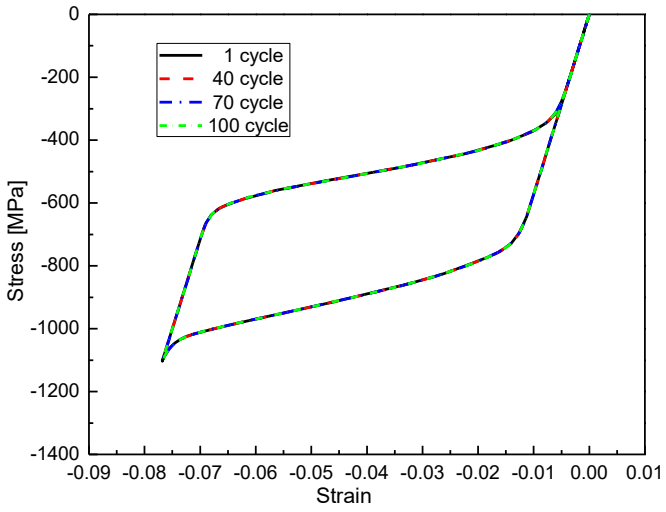

Figure 3.7: The cyclic stress-strain response predicted by the proposed model for an upper surface point under isothermal loading condition (from Figure 5 of [121], © 2019 by IOP Publishing, with permission of IOP Publishing, DOI:10.1088/1361-665x/ab1acb).

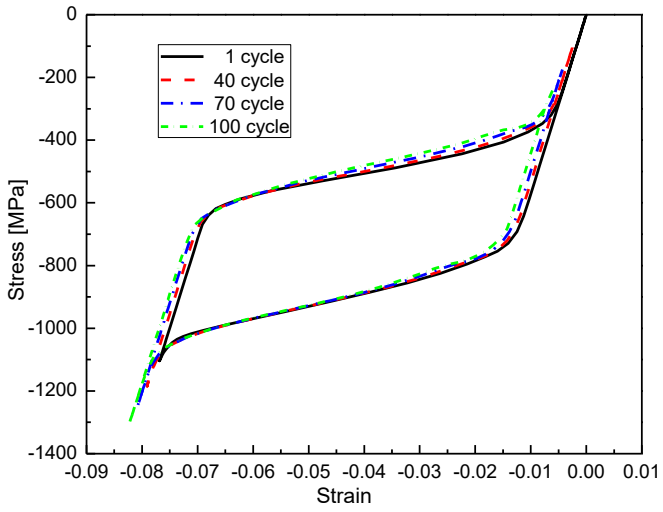

Figure 3.8: The cyclic stress-strain response predicted by the infinitesimal strain model using Abaqus nonlinear solver for an upper surface point under isothermal loading condition (from Figure 5 of [121], © 2019 by IOP Publishing, with permission of IOP Publishing, DOI:10.1088/1361-665x/ab1acb).

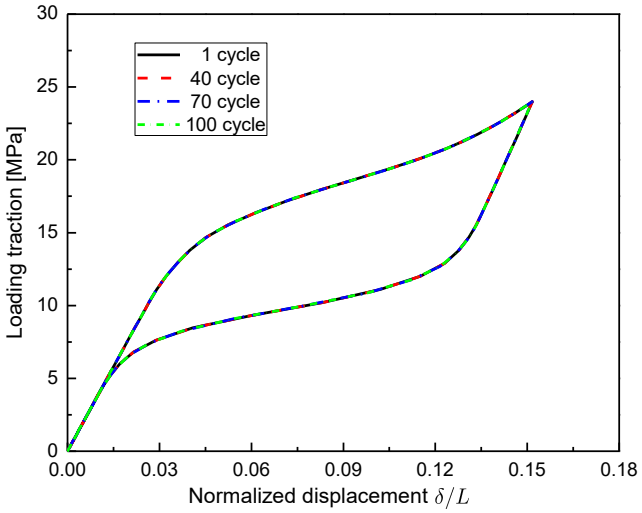

Figure 3.9: The cyclic load-displacement response predicted by the proposed model for an SMA beam under isothermal loading condition (from Figure 6 of [121], © 2019 by IOP Publishing, with permission of IOP Publishing, DOI:10.1088/1361-665x/ab1acb).

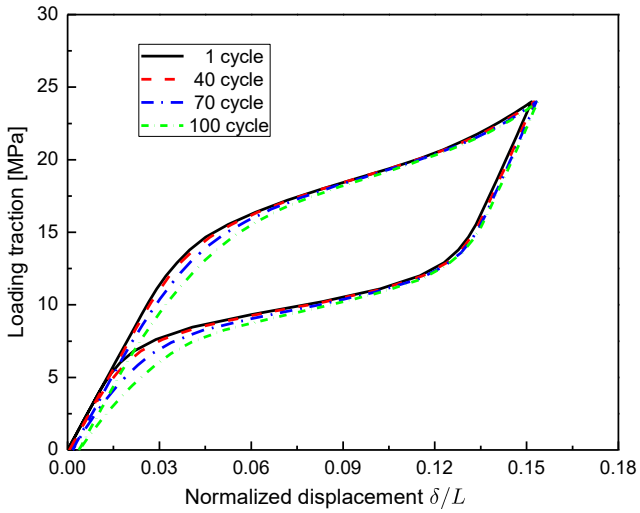

Figure 3.10: The cyclic load-displacement response predicted by the infinitesimal strain model using Abaqus nonlinear solver for an SMA beam under isothermal loading condition (from Figure 6 of [121], © 2019 by IOP Publishing, with permission of IOP Publishing, DOI:10.1088/1361-665x/ab1acb).

3.6.3 SMA tube under isothermal loading

In this subsection, the BVP of a three-dimensional SMA torque tube under torsion loading is studied. Refer to Figure 3.11(a), the tube has an inner radius $r = 3.0$(mm) and thickness $t/r = 0.1$. In order to reduce the computational cost, a representative tube segment $L/r = 2/3$ is analyzed here. Boundary conditions are depicted in Figure 3.11(b), the tube left face is fixed and the right face is subjected to a torsion loading. The torque proportionally increases to 25 (N·m) then unloads to 0 (N·m), the temperature is kept constant at 380 K. The torque tube undergoes a fully forward phase transformation from austenitic phase to martensitic phase followed by a reverse phase transformation from martensitic phase to austenitic phase. The material parameters used in this simulation are from table 3.4.

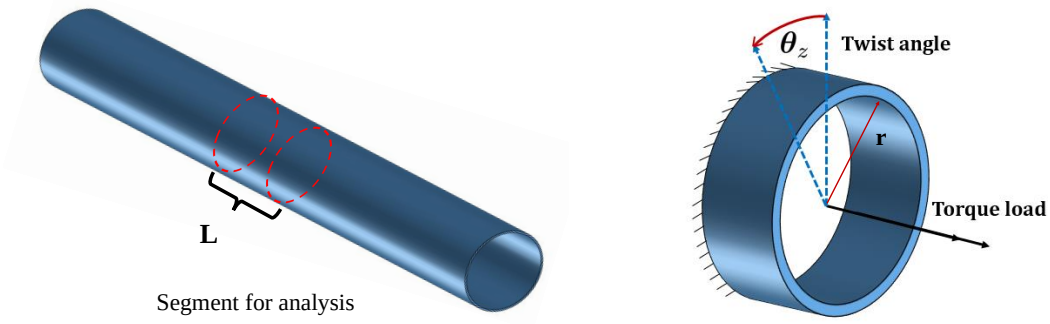

(a) Full size torque tube geometry

(b) Reduced size torque tube geometry

Figure 3.11: Schematic for the cylindrical SMA torque tube subjected to isothermal torsion loading (from Figure 7 of [121], © 2019 by IOP Publishing, with permission of IOP Publishing, DOI:10.1088/1361-665x/ab1acb).

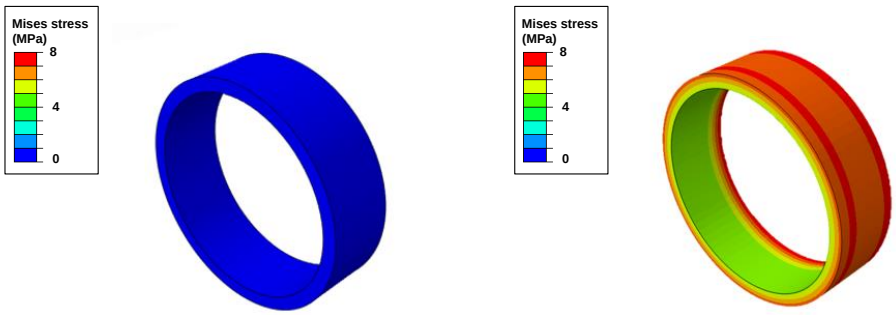

(a) Proposed model

(b) Abaqus nonlinear solver

Figure 3.12: Mises stress residuals accumulated after one loading cycle for the torque tube predicted by the proposed model and the Abaqus nonlinear solver (from Figure 7 of [121], © 2019 by IOP Publishing, with permission of IOP Publishing, DOI:10.1088/1361-665x/ab1acb).

The cyclic shear stress-strain response of a material point from the tube outer surface at the right end is predicted by the proposed model and Abaqus nonlinear solver. As shown in Figure 3.14, similar to the results observed in the SMA beam case, a shifting response is predicted by the Abaqus nonlinear solver due to the accumulation of shear stress errors. In contrast, a stable response is predicted by the proposed model shown in Figure 3.13. More specifically, Figure 3.12 shows the magnitude of stress residual accumulated after one loading cycle. The value of Mises stress residual predicted by the proposed model is almost zero compared to a value around 4 MPa predicted by the Abaqus nonlinear solver. As a result of the accumulation of such shear stress errors, the shear stress levels required to start the forward phase transformation spuriously decreases in the case of Abaqus nonlinear solver shown in Figure 3.14. Besides, the maximum shear stress levels at the end of forward transformation increases, and the shape of hysteresis loop also changes. The cyclic structural response of the torque tube is also provided in Figure 3.15 and Figure 3.16 by plotting the applied torque versus the twist angle θ_z. It can be seen that a stable structural response is predicted by the proposed model shown in Figure 3.15 compared to a shifting structural response predicted by the Abaqus nonlinear solver shown in Figure 3.16. From the observation on these results, it is seen that the Abaqus nonlinear solver is not able to predict reliable results for the SMA torque tube subjected to 100 shearing cycles any more. Thus, the proposed model that can resolve the shear stress errors is required for the SMA torque tube subjected to cyclic torsion loading.

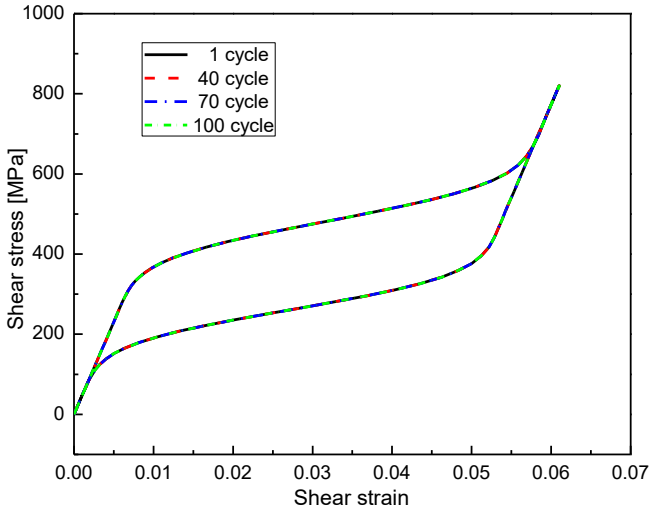

Figure 3.13: The cyclic shear tress-strain response predicted by the proposed model for an SMA tube under isothermal loading condition (from Figure 9 of [121], © 2019 by IOP Publishing, with permission of IOP Publishing, DOI:10.1088/1361-665x/ab1acb).

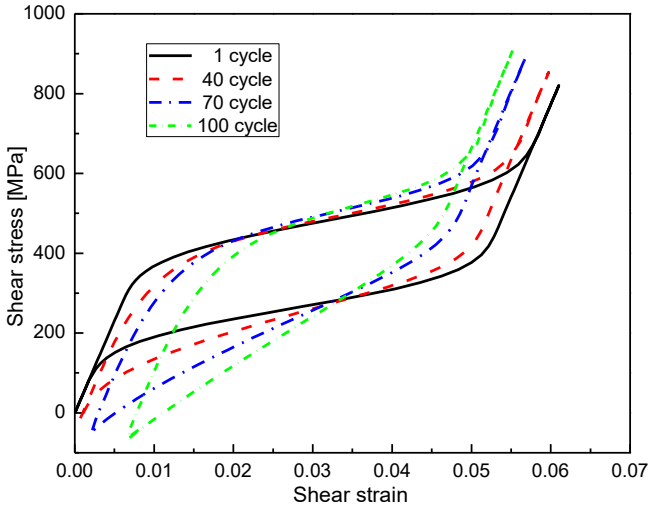

Figure 3.14: The cyclic shear tress-strain response predicted by the infinitesimal strain model using Abaqus nonlinear solver for an SMA tube under isothermal loading condition (from Figure 9 of [121], © 2019 by IOP Publishing, with permission of IOP Publishing, DOI:10.1088/1361-665x/ab1acb).

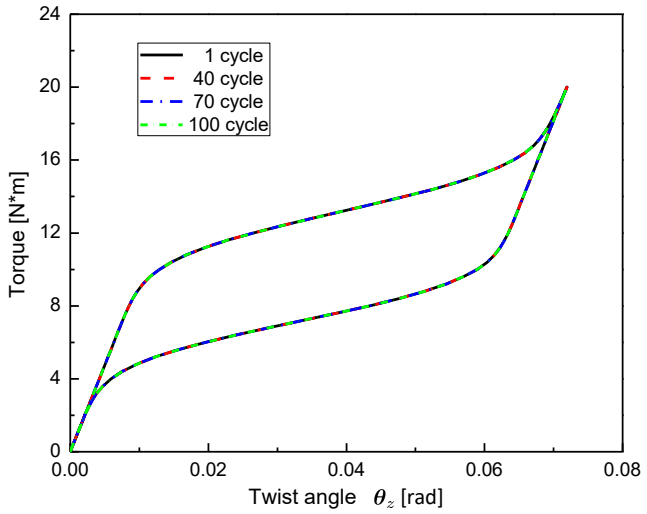

Figure 3.15: The cyclic load-displacement curve predicted by the proposed model for an SMA tube under isothermal condition (from Figure 10 of [121], © 2019 by IOP Publishing, with permission of IOP Publishing, DOI:10.1088/1361-665x/ab1acb).

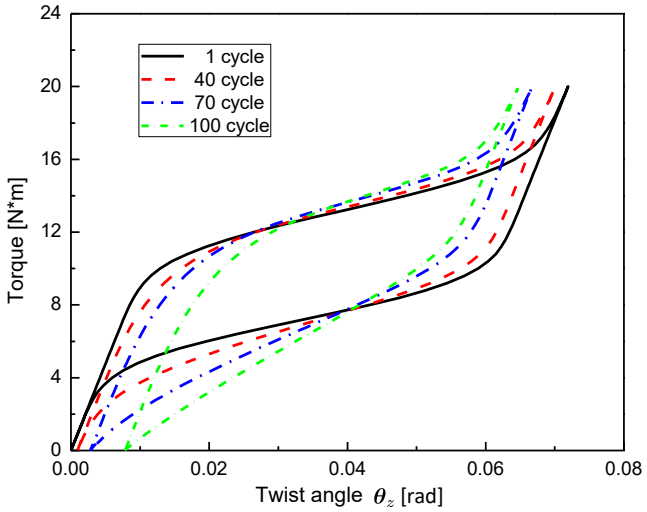

Figure 3.16: The cyclic load-displacement curve predicted by the infinitesimal strain model using Abaqus nonlinear geometry option on for an SMA tube under isothermal condition (from Figure 10 of [121], © 2019 by IOP Publishing, with permission of IOP Publishing, DOI:10.1088/1361-665x/ab1acb).

3.6.4 SMA tube under isobaric loading

In order to test the capability of the proposed model to predict the thermally-induced phase transformation in SMAs, a three-dimensional cylindrical SMA tube is studied under cyclic isobaric torsional loading, i.e., subjected to a constant torsion load with temperature variation cycles. The SMA torque tubes has been investigated as rotational actuators to realize a morphing wing during the plane take-off and cruise regime [86, 62, 16, 38]. The design and optimization of such SMA-based morphing structure requires a thorough understanding on the response of SMA torque tubes subjected to cyclic isobaric loading. To that end, the SMA tube component is analyzed under cyclic isobaric loading conditions. The model has the same geometry and material information as the tube simulation in section 3.6.3. The loading condition is as follows, a 3 N·m torque load is applied to the tube right end and the temperature varies between 250 K and 390 K for 100 cycles. Cyclic shear strain-temperature and $\boldsymbol{\theta}_z$-temperature curves are obtained via the proposed model and the Abaqus nonlinear solver. As found in the previous examples, the artificial stress residuals caused by other non-objective rates, *i.e.*, Jaumman rate used in Abaqus nonlinear solver, builds up during the cyclic loading, which in return causes a shifting material and structural response. To demonstrate the effectiveness of the proposed model to eliminate the artificial stress residuals,

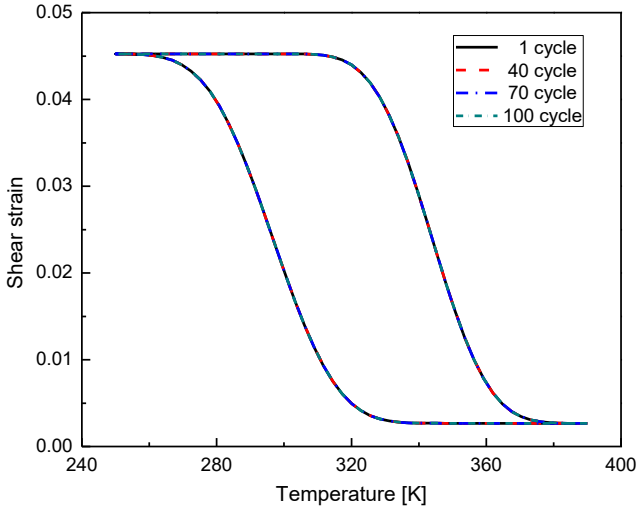

Figure 3.17: The cyclic temperature-shear strain curve predicted by the proposed model for an SMA tube under constant torsion loading condition (from Figure 11 of [121], © 2019 by IOP Publishing, with permission of IOP Publishing, DOI:10.1088/1361-665x/ab1acb).

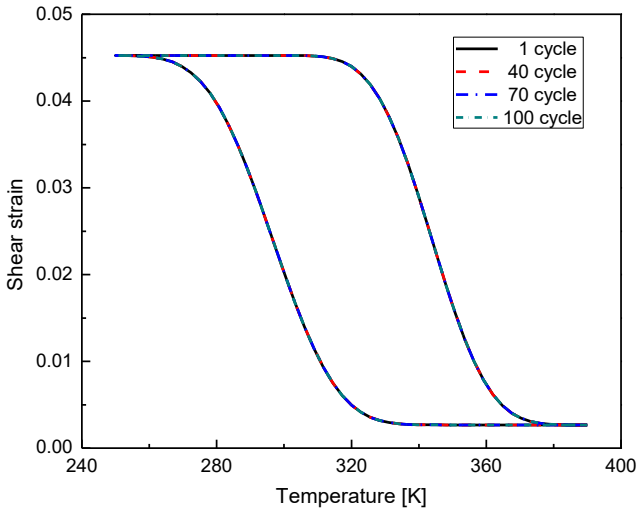

Figure 3.18: The cyclic temperature-shear strain curve predicted by the infinitesimal strain model using Abaqus nonlinear solver for an SMA tube under constant torsion loading condition (from Figure 11 of [121], © 2019 by IOP Publishing, with permission of IOP Publishing, DOI:10.1088/1361-665x/ab1acb).

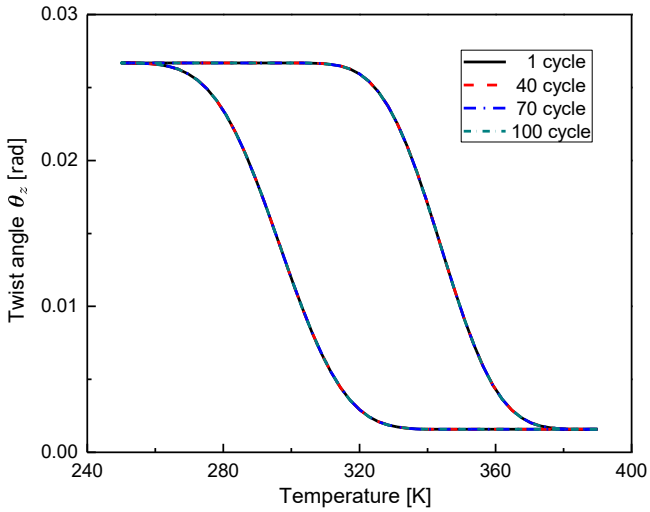

Figure 3.19: The cyclic temperature-θ_z curve predicted by the proposed model for an SMA tube under constant torsion loading condition (from Figure 12 of [121], © 2019 by IOP Publishing, with permission of IOP Publishing, DOI:10.1088/1361-665x/ab1acb).

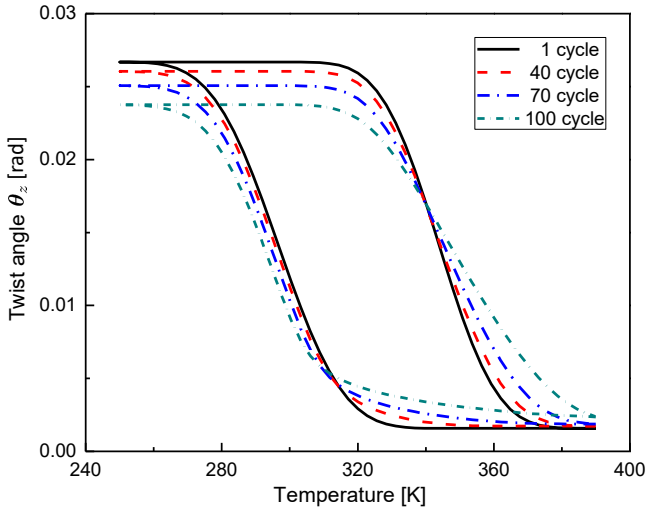

Figure 3.20: The cyclic temperature-θ_z curve predicted by the infinitesimal strain model using Abaqus nonlinear solver for an SMA tube under constant torsion loading condition (from Figure 12 of [121], © 2019 by IOP Publishing, with permission of IOP Publishing, DOI:10.1088/1361-665x/ab1acb).

As it is shown in Figure 3.17, a stable cyclic shear strain-temperature response for the tube is predicted by the proposed model. In contrast, a shifting cyclic strain-temperature response is predicted by using the Abaqus nonlinear solver shown in Figure 3.18. More specifically, it can be seen that the isobaric response drifts downwards at $T = 240$ K and is lifted up at $T = 390$ K from cycle to cycle due to the stress error accumulation. Similar to the observation on the strain-temperature response, the cyclic $\boldsymbol{\theta}_z$-temperature response is stable in the case of proposed model, and it is a shifting response predicted by the Abaqus nonlinear solver. The comparison on $\boldsymbol{\theta}_z$-temperature response is plotted in Figure 3.19 and Figure 3.20. Based upon the analysis of SMA tube subjected to thermal loading cycles, it is shown that the accumulated stress errors from Abaqus nonlinear solver result in an shifting cyclic isobaric response, and such artificial stress errors can be eliminated by using the proposed model.

Table 3.5: Calibrated material parameters for NiTi (50.8 at.% Ni), adapted from [47].

Type	Parameter	Value	Parameter[4]	Value
Key material parameters 12	E_A	32.5 [GPa]	C_A	3.5 [MPa/K]
	E_M	23.0 [GPa]	C_M	3.5 [MPa/K]
	$\nu_A = \nu_M$	0.3	M_s	264 [K]
	$\alpha_A = \alpha_M$	2.2×10^{-5} [K^{-1}]	M_f	160 [K]
	H^{max}	3.3%	A_s	217 [K]
	k_t	N/A	A_f	290 [K]
Smooth hardening parameters 4	n_1	0.17	n_3	0.25
	n_2	0.27	n_4	0.35

[4]The values of transformation temperatures (M_s, M_f, A_s, A_f) are referenced from [65] in order to realize the self-expanding process within human body environment, the rest of values of the material parameters are taken from [47] as they are not provided from [65].

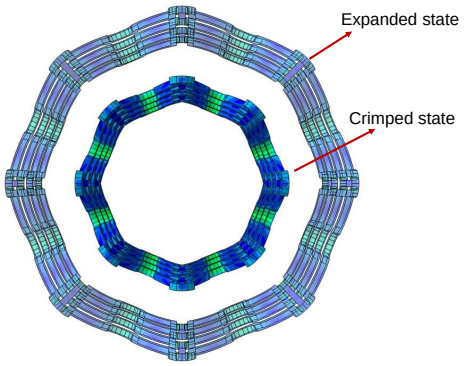

(a) The expanded and crimped state for the flexible structure

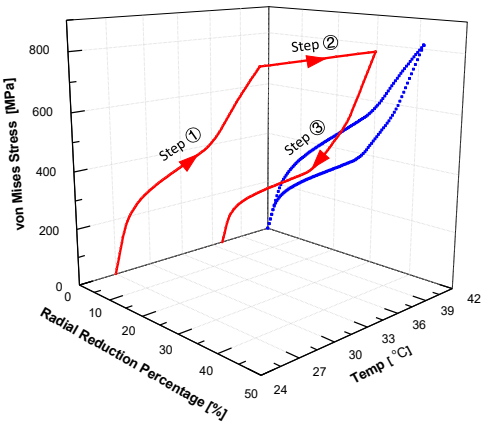

(b) Loading path of the flexible structure

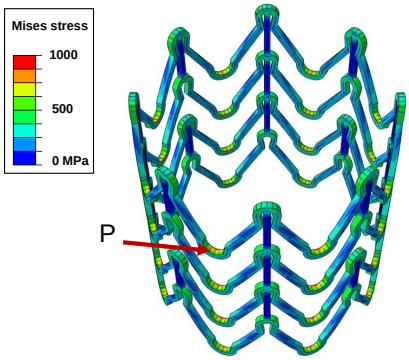

(c) von Mises stress

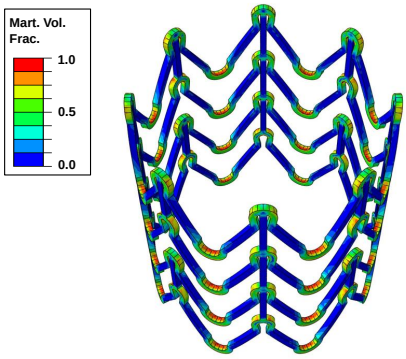

(d) Martensitic volume fraction

Figure 3.21: The expanded and crimped shapes, loading path, von Mises stress distribution and martensitic volume fraction contour of the SMA flexible structure during the self-expanding analysis (from Figure 13 of [121], © 2019 by IOP Publishing, with permission of IOP Publishing, DOI:10.1088/1361-665x/ab1acb).

3.6.5 3-D analysis of a flexible SMA structure

In this section, a 3-D solid SMA flexible structure is studied to demonstrate that the proposed model can be used as a 3-D structural design tool. This SMA flexible struc-

ture can be used as a stent to provide a less invasive method for administering support to diseased arteries, veins or other vessels in the human body. They are crimped into a smaller shape outside the body then inserted into the diseased artery. After being delivered into the desired position, the flexible structure expands automatically by using the phase transformation of SMAs [42]. The loading path of this self-expanding structure can be described with three steps, i.e., 1) The flexure is firstly crimped outside the body by external constraints and attached to a constraint container device called catheter or cannula. 2) The flexure is inserted into the body while the temperature increases from the room temperature to the body temperature. 3) The structure recovers its original shape when the constraint is removed [95, 44, 61]. Although there are analysis for similar type of flexible structure by other researchers [2, 32], among which only a small unit cell of the structure is analyzed. Here a full scale 3-D SMA flexible structure designed for repairing aortic dissection [42, 41] is studied to provide the global response of the structure during the self-expanding process. The structure is 32 (mm) long, 25.4 (mm) in outer diameter with 4 struts and 0.5 (mm) thick in radial direction. Due to the curvature of the structure strut, the SMA flexure experiences large rotation and stress concentrations around the hinge part, which in return results in a complex local non-proportional stress and strain evolutions at the hinge. The loading path of this analysis is indicated by the red curve in Figure 3.21(b). The material parameters used in this simulation are from table 3.5.

The expanded and crimped shapes of the SMA flexure during the analysis are shown in Figure 3.21(a). As illustrated in Figure 3.21(c), stress concentration due to the strut curved part is observed. The von Mises contour indicates that a local non-proportional stress field is evolved at the hinge location during the crimping process. As shown in Figure 3.21(d), while the straight strut part is still in austenitic phase, the stress-induced martensitic phase transformation is activated by the stress concentration at the hinge location subjected to bending. The martensitic volume fraction contour for the flexure during

the crimping process is shown in Figure 3.21(d). The global structural response of the SMA flexure for a material point P (see Figure 3.21(c)) is provided in terms of a 3-D stress-temperature-displacement curve in Figure3.21(b), in which the red curve indicates the actual response while the blue curve is the projection of blue curve on the stress-radial reduction ratio plane. This well captured non-proportional stress evolution and martensitic phase transformation in this example demonstrates that the proposed model can be used as an efficient tool for the 3-D analysis and design of complex SMA-based structures.

3.7 Concluding remarks

Based on the SMA model proposed by Lagoudas and coworkers for small deformation analysis, a three-dimensional constitutive model for martensitic transformation in polycrystalline SMAs accounting for large deformation has been proposed in this work. Three important characteristics in SMA reponse are considered, i.e., the smooth transition during the phase transformation, the stress dependent transformation strain to account for the coexistence of oriented/self-accommodated martensitic variants, and a stress dependent critical driving force to consider the effect of applied stress levels on the size of hysteresis loop. The proposed model is formulated based on the finite deformation framework that utilizes logarithmic strain and rate such that it not only accounts for the large strains and rotations that an SMA component may undertake, but also resolves the artificial stress errors that are caused by using other non-integrable objective rates. The proposed model is able to predict the stress-induced and thermally induced phase transformations in SMAs under general three-dimensional thermomechanical loading. In particular, it was shown in the example of an SMA bar that the proposed model accounts for the geometry nonlinearity induced by large strains, so that it corrects the spurious material softening in the results from its infinitesimal counterpart. In the numerical examples of an SMA beam and an SMA torque tube, it was demonstrated that the proposed model captures

the large rotations that SMA-based components may undertake. By comparing the predicted cyclic response to the results obtained through the Abaqus nonlinear solver, the proposed model demonstrated that it effectively resolves the artificial stress errors. In the end, a 3-D solid flexible structure experiencing local, non-proportional stress and strain evolution was analyzed by the proposed model, which shows the proposed model can be used as an efficient tool for the 3-D analysis and design of complex SMA-based structures. The detailed formulation of the proposed model and its implementation procedures make it readily used by other researchers. The model can be further extended to incorporate additional nonlinear phenomena exhibited by SMAs, such as transformation-induced plasticity, viscoplasticity, and damage evolution.

4. FINITE STRAIN CONSTITUTIVE MODELING OF SHAPE MEMORY ALLOYS CONSIDERING MULTIAXIAL TRANSFORMATION-INDUCED PLASTICITY EVOLUTION AND TWO-WAY SHAPE MEMORY EFFECT

4.1 Introduction

Shape memory alloys (SMAs) represent an active/smart material with the ability to recover their pre-defined shape via a diffusionless phase transformation between its high-symmetry, high-temperature austenitic phase and its low-symmetry, low-temperature martensitic phase. Due to the high output energy density of SMAs compared to other active materials such as shape memory polymers and piezoelectrics, up to 500 MPa actuation stress and 8% recoverable strain [72], their current and potential applications in the biomedical, aerospace, automobile and civil engineering fields are expanding rapidly [33, 40, 75, 92]. SMAs have been extensively researched as solid-state actuators to enable adaptive and morphing structures. For examples, an SMA-based beam component has been used as a bending actuator to morph the engine outer shell geometry so that desired aerodynamic conditions can be achieved during the airplane take-off and cruise regime [33]. SMA-based torque tubes have been used as rotation actuators to deploy and retract solar panels for small satellites [108], and also used as rotational actuators to rotate the trailing edge wing flap during an airplane on-fly test [62, 16].

The majority of engineering applications require SMAs experiencing a large number of loading cycles involving repeated phase transformations, which brings the increasing necessity to understand the material response of SMAs subjected to cyclic thermomechanical loading. Many experimental results [97, 98, 49, 50, 110] indicate that SMAs exhibit an evolving rather than stable material response under cyclic loading. More specifically, transformation characteristics of SMAs, e.g., the shape of stress/thermal hysteresis, trans-

formation temperatures, transformation strain magnitude, usually shift from one cycle to another, and large irrecoverable plastic strains are accumulated as shown in Figure 4.1. Such irrecoverable strains, often called TRIP, are caused by the distortion as a result of the crystallographic misfit at the austenite-martensite interfaces and grain boundaries induced by the repeated phase transformation. This distortion-driven activity results in an observable macroscopic plastic strain, which occurs at an effective stress level much lower than the conventional plastic yielding point [50]. In addition, TRIP strain evolves with different rates throughout the entire material fatigue life state. It is shown in the SMA fatigue test results, the TRIP strain grows drastically during the very first hundreds loading cycles then tends to increase in a stabilized trend until the material failing point at the very end. As the most of engineering applications require actuators functioning in stable material behavior, SMAs are usually subjected to a training process, i.e., repeated thermal/stress cycling, to stabilize their behaviors before being used as actuation components. Many modeling efforts have been devoted to predicting the evolving characteristics of SMAs incorporating the irrecoverable strains under cyclic thermomechanical loading.

A large number of legacy models have been proposed to predict the stable SMA material response. A thorough review of these works can be found from literature [54, 10, 73, 103, 74, 125, 48, 2, 47, 106]. In general, SMA models considering irrecoverable strains can be categorized into two types, one type of SMA models describe conventional plasticity due to the activation of slip systems at sufficiently high-stress levels in either pure austenite or martensite phase, modeling efforts fall into this type can be obtained from [107, 30, 43]. As discussed in the previous paragraph to some extent, the other type of models concerns irrecoverable strains as TRIP caused by repeated phase transformations with the stress levels much below yielding stress. It is noted that the focus of this work falls into the second type. Many commonly cited SMA models are proposed to capture the evolving response feature, and a subset of them are briefly reviewed here. The ear-

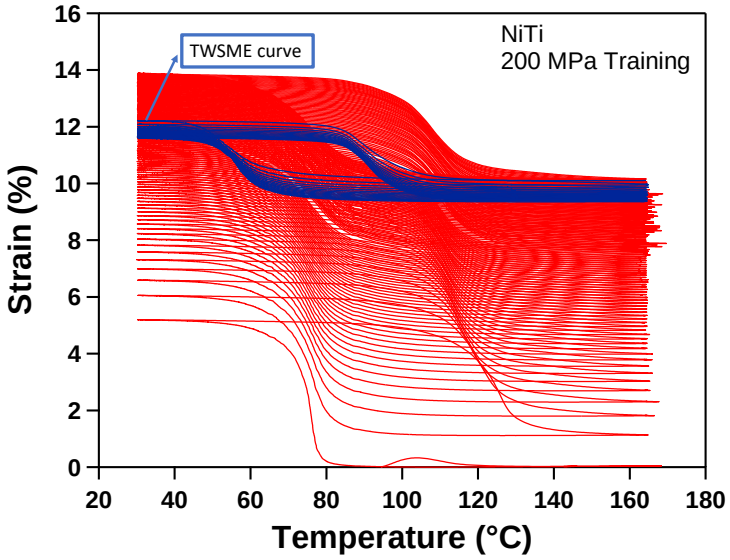

Figure 4.1: Experimental result shows the TWSME at load-free condition for a NiTi material after 100 thermal training cycles under a constant load. The red curve is the response under bias load, and the blude curve indicates the TWSME reponse under load-free condition, adapted from [3].

liest models dealing with TRIP were presented by Lim and McDowell [60], and Tanaka et al. [101] to capture the cyclic loading effect on the SMA phase transformation characteristics. Based on the micromechanics averaging method on a representative volume element with an infinitesimal increment of martensite, Bo and Lagoudas [8, 9] proposed a model accounting for one-dimensional TRIP strain accumulation and the generation of TWSME under cyclic actuation loading. Lexcellent et al. [59] further extended their early SMA model describing stable material response [55] to consider the irrecoverable strains by introducing two additional internal state variables, i.e., the volume fraction of self-accommodated and oriented martensite. Later on, [50] proposed a model accounting for TRIP during stress-induced phase transformation, as well as the shape and size of the hysteresis under transformation cycling. Also, Zaki and Moumni [125] proposed a model considering the TRIP in the case of cyclic pseudoelastic loading by virtue of

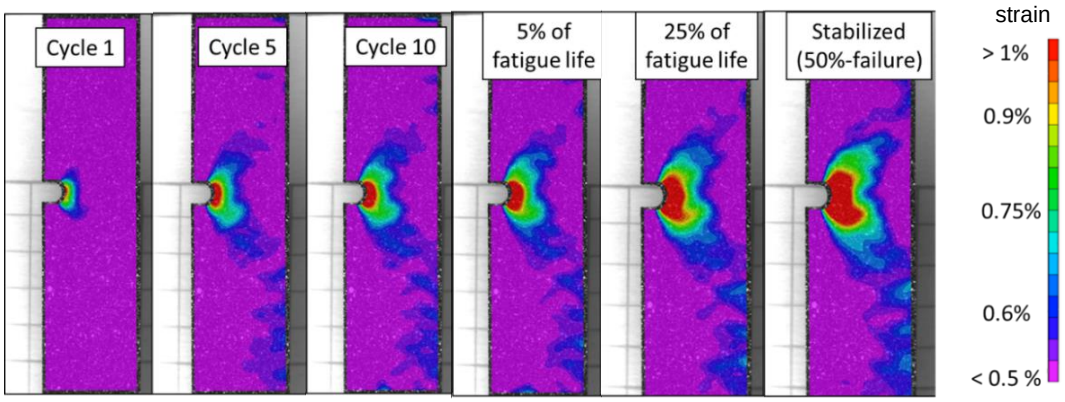

Figure 4.2: Evolution of transformation and TRIP strain in the loading direction for a notched NiTi plate under thermal cycling with constant load, adapted from [109].

additional internal state variables, such as internal stress, TRIP strain, and accumulated martensite volume fraction. Other similar and recent modeling efforts can also be found from [4, 85, 6, 122].

Although many of the proposed models have enabled researchers to study the evolving material behaviors of SMAs, the majority of them are insufficient in their capacity to consider the following critical features. (i) The first feature of currently available models in need of improvement is their small deformation assumption based on infinitesimal strain theory. This assumption may be acceptable for SMA material systems, such as Ni-rich or NiTiHf SMAs, where the total deformation strain regime, including elastic strain, transformation strain, and TRIP strain, is below 3%. However, it has been reported that nearly 30% or even higher TRIP strains are observed during the lifetime of near equiatomic NiTi SMA-based actuators [110]. In the presence of such large strain, a finite strain model is needed to account for the exhibited large strains to provide an accurate structural response of SMA-based functional components. (ii) The second important aspect of many current models in need of improvement is the TWSME characteristic exhibited by trained SMAs

at load-free conditions. Because of the required training process to stabilize the response of as-received SMAs before used as actuators, permanent changes such as dislocation bands, accumulated defects/damage, and retained martensite variants are introduced in the microstructure of the material, which then results in the generation of an oriented internal stress field. The generated internal stresses oriented in the same direction as the applied load are subsequently able to induce the oriented phase transformation under thermal cycling without applying any pre-loading, i.e., the TWSME, see Figure 4.1. The TWSME property allows for mounting and dismounting of SMA-based connectors and couplers in an easy procedure by just heating and cooling those components without pre-stressing [70, 100]. In addition, (iii) the majority of applications require the functionality of actuators under multiaxial stress state originated from geometry complexities or installment required discontinuities, such as notches and holes. TRIP strain under such multiaxial stress state evolves quite differently compared to that in the uniaxial loading case. Refer to Figure 4.2, Digital Image Correlation (DIC) results of transformation and TRIP strain for a notched NiTi plate revealed that the TRIP strain evolved with a larger rate at the stress concentration region over the part under uniform stress state throughout the SMA entire fatigue life. Despite the importance of the fact that multiaxial stress state significantly affecting the evolution of TRIP strain, it has rarely been addressed among existing models described in the literature.

In order to address the three aforementioned critical features, a three-dimensional finite strain constitutive model accounting for multiaxial TRIP evolution and TWSME for SMAs is proposed in this work. This presented modeling effort is developed based on the legacy SMA model [10, 47, 121] and largely inspired by its continuous development considering TRIP [9, 50, 122]. By using the martensitic volume fraction, transformation strain, internal stress, and TRIP strain tensors as internal state variables, the model is able to capture the TRIP evolution in SMAs subjected to multiaxial stress state during cyclic

thermomechanical loading, and the TWSME due to the generation of internal stresses exhibited by trained SMAs without pre-loading.

In summary, this chapter is organized as follows. In Section 4.2, preliminaries regarding kinematics used in the model formulation are presented. Section 4.3 concentrates on the model development that incorporates the three features as mentioned earlier to improve the model capability. In section 4.4, the consistent tangent stiffness and thermal matrix are provided. A detailed calibration for the material parameters is presented in section 4.5. In section 4.6, the detailed implementation procedure for the proposed model is described by using a user-defined material subroutine (UMAT) through the numerical environment Abaqus. Numerical examples are studied to demonstrate the capability of the proposed model in Section 4.7. Conclusions are summarized in Section 4.8.

4.2 Preliminary

4.2.1 Logarithmic rate and Logarithmic spin

Two kinematic assumptions, i.e., the multiplicative decomposition of deformation gradient $\mathbf{F}$ and the additive decomposition of the rate of deformation tensor $\mathbf{D}$, are usually used in finite deformation theory. Hyperelastic constitutive relation is often used in multiplicative models while hypoelastic constitutive equation is utilized for additive models. For a long time, the rate form hypoelastic constitutive theory has been criticized for its failure to be fully integrable to describe a simple recoverable elastic behavior. Many spurious phenomenons, such as shear stress oscillation, dissipation or stress errors are observed in simple elastic deformation using hypoelastic theory with objective rates including many well-known objective rates such as Zaremba-Jaumann rate, Green-Naghdi rate, and Truesdell rate, etc.[116]. However, such aforementioned issues regarding objective rates are resolved via the logarithmic rate proposed by [112, 113, 116, 13, 14, 15, 66, 67]. As proved in their work, the logarithmic rate of the logarithmic strain $\mathbf{h}$ expressed in its

Eulerian type is identical with the rate of deformation tensor $\mathbf{D}$, by which a hypoelastic model can be exactly integrated into an finite strain elastic model ([112]). This unique relationship between logarithmic strain $\mathbf{h}$ and the rate of deformation tensor $\mathbf{D}$ can be expressed as,

$$\mathring{\mathbf{h}}^{log} = \dot{\mathbf{h}} + \mathbf{h}\boldsymbol{\Omega}^{log} - \boldsymbol{\Omega}^{log}\mathbf{h} = \mathbf{D} \tag{4.1}$$

where $\boldsymbol{\Omega}^{log}$ is the logarithmic spin introduced by [112] as,

$$\boldsymbol{\Omega}^{log} = \mathbf{W} + \sum_{i \neq j}^{n} \Big(\frac{1 + (\lambda_i/\lambda_j)}{1 - (\lambda_i/\lambda_j)} + \frac{2}{\ln(\lambda_i/\lambda_j)}\Big)\mathbf{b}_i\mathbf{D}\mathbf{b}_j \tag{4.2}$$

in which $\lambda_{i,j}(i, j = 1, 2, 3)$ are the eigenvalues of left Cauchy-Green tensor $\mathbf{B}$, $\mathbf{b}_i, \mathbf{b}_j$ are the corresponding subordinate eigenprojections. Additionally, the second-order rotation tensor $\mathbf{R}^{log}$ can be obtained using the logarithmic spin tensor $\boldsymbol{\Omega}^{log}$ by solving the following differential equation. In general, $\mathbf{R}^{log}|_{t=0} = \mathbf{I}$ is assumed.

$$\boldsymbol{\Omega}^{log} = \dot{\mathbf{R}}^{log}(\mathbf{R}^{log})^T \tag{4.3}$$

Furthermore, assuming the initial condition $\mathbf{h}|_{t=0} = \mathbf{0}$, equation (4.1) can be integrated to the following equation through the corotational integration scheme ([45]),

$$\mathbf{h} = \int_{\text{corot.}} \mathbf{D}\, \mathrm{d}t = (\mathbf{R}^{log})^T \bigg(\int_0^t \mathbf{R}^{log}\mathbf{D}^e(\mathbf{R}^{log})^T \mathrm{d}t' \bigg) \mathbf{R}^{log} \tag{4.4}$$

4.2.2 Additive decomposition of logarithmic strain

This part address the kinematic assumption of additive decomposition of logarithmic strain. First, the rate of deformation tensor $\mathbf{D}$ is additively decomposed into three parts, i.e., an elastic part, a transformation part plus a TRIP part. From energy point of view, additive decomposition of $\mathbf{D}$ can be interpreted as the total outside stress power is split into

an elastic part stored inside the material, a dissipative part associated with phase transformation process, and another dissipative part related to transformation-induced plasticity mechanism.

$$\mathbf{D} = \mathbf{D}^{e} + \mathbf{D}^{tr} + \mathbf{D}^{tp} \tag{4.5}$$

Based on equation (4.1), the elastic part $\mathbf{D}^{e}$, transformation part $\mathbf{D}^{tr}$ and plastic part $\mathbf{D}^{tp}$ can be rewritten as $\mathring{\mathbf{h}}^{e\_log}$, $\mathring{\mathbf{h}}^{tr\_log}$ and $\mathring{\mathbf{h}}^{tp\_log}$ respectively,

$$\mathring{\mathbf{h}}^{e\_log} = \mathbf{D}^{e};\;\; \mathring{\mathbf{h}}^{tr\_log} = \mathbf{D}^{tr};\;\; \mathring{\mathbf{h}}^{tp\_log} = \mathbf{D}^{tp} \tag{4.6}$$

the following equation can be obtained by combining equations (4.1), (4.5) and (4.6),

$$\mathring{\mathbf{h}}^{log} = \mathring{\mathbf{h}}^{e\_log} + \mathring{\mathbf{h}}^{tr\_log} + \mathring{\mathbf{h}}^{tp\_log} \tag{4.7}$$

Applying corotational integration on equation (4.7) as follows,

$$\mathbf{h}^{e} = \int_{\text{corot.}} \mathbf{D}^{e}\ \mathrm{d}t = (\mathbf{R}^{log})^{T}\left(\int_{0}^{\tau} \mathbf{R}^{log}\mathbf{D}^{e}(\mathbf{R}^{log})^{T}\mathrm{d}\tau\right)\mathbf{R}^{log} \tag{4.8a}$$

$$\mathbf{h}^{tr} = \int_{\text{corot.}} \mathbf{D}^{tr}\ \mathrm{d}t = (\mathbf{R}^{log})^{T}\left(\int_{0}^{\tau} \mathbf{R}^{log}\mathbf{D}^{tr}(\mathbf{R}^{log})^{T}\mathrm{d}\tau\right)\mathbf{R}^{log} \tag{4.8b}$$

$$\mathbf{h}^{tp} = \int_{\text{corot.}} \mathbf{D}^{tp}\ \mathrm{d}t = (\mathbf{R}^{log})^{T}\left(\int_{0}^{\tau} \mathbf{R}^{log}\mathbf{D}^{tp}(\mathbf{R}^{log})^{T}\mathrm{d}\tau\right)\mathbf{R}^{log} \tag{4.8c}$$

Combing equations (4.4), (4.5), (4.7) and (4.8), the following kinematic equation on total logarithmic strain can be received. Namely, the total logarithmic strain is additively split into an elastic part, a transformation part, as well as a TRIP part

$$\mathbf{h} = \mathbf{h}^{e} + \mathbf{h}^{tr} + \mathbf{h}^{tp} \tag{4.9}$$

4.3 Model formulation

4.3.1 Thermodynamic potential

Based on the classical thermodynamic framework for dissipative materials, the formulation of the proposed model starts with the development of an explicit thermodynamic potential. To that end, a quadratic form Gibbs free energy is proposed as a continuous function of Kirchhoff stress tensor $\boldsymbol{\tau}$, temperature T, and a set of internal state variables $\boldsymbol{\Upsilon} = \{\xi, \mathbf{h}^{tr}, \mathbf{h}^{tp}, \boldsymbol{\beta}\}$, in which they are martensitic volume fraction ξ, transformation strain tensor $\mathbf{h}^{tr}$, TRIP strain tensor $\mathbf{h}^{tp}$, and internal stress tensor $\boldsymbol{\beta}$. The martensitic volume fraction ξ ranging $0 \leqslant \xi \leqslant 1$ is used for differentiating the two material phases of SMA. Specifically, $\xi = 0$ represents pure austenitic phase while $\xi = 1$ indicates pure martensitic phase. The $\mathbf{h}^{tr}$ accounts for the inelastic yet recoverable strain associated with the phase transformation, $\mathbf{h}^{tp}$ is used to represent the irrecoverable transformation-induced plastic strain, and $\boldsymbol{\beta}$ is used to consider the internal stress field generated inside the material as a result of the training process. The following explicit Gibbs free energy expression for G is given as,

$$\begin{aligned} G = -\frac{1}{2\rho_0}\boldsymbol{\tau} : \mathcal{S}\boldsymbol{\tau} - \frac{1}{\rho_0}\boldsymbol{\tau} : [\, \boldsymbol{\alpha}(T - T_0) + \mathbf{h}^{tr} + \mathbf{h}^{tp}] - \frac{1}{\rho_0}\int_0^{\xi} (\boldsymbol{\beta} : \frac{\partial \mathbf{h}^{tr}}{\partial \tau}) d\tau \\ + c\Big[(T - T_0) - T\ln(\frac{T}{T_0})\Big] - s_0 T + u_0 + \frac{1}{\rho_0} f(\xi) \end{aligned} \tag{4.10}$$

In which, $\mathcal{S}$ is the fourth-order effective compliance tensor that can be calculated by using the rule of mixture as equation (3.30), $\mathcal{S}^A$ is the compliance tensor for austenitic phase while $\mathcal{S}^M$ is for martensitic phase, $\Delta\mathcal{S}$ represents the phase difference of the compliance tensor. Additionally, the effective stiffness tensor $\mathcal{C}$ can be obtained by taking the inverse of the above effective compliance tensor, i.e., $\mathcal{C} = \mathcal{S}^{-1}$. $\boldsymbol{\alpha}$ is the second-order thermoelastic expansion tensor, c is the effective specific heat, s_0 and u_0 are the effec-

tive specific entropy and effective specific internal energy at the reference state. All the aforementioned effective variables are determined by the rule of mixture the same way as they were in Chapter 3. T represents the temperature at current state, while T_0 is the temperature at reference state.

A smooth hardening function $f(\xi)$ is included in the Gibbs free energy expression to account for the part due to hardening effects in polycrystalline SMAs, such as interactions between different phase variants, imperfections located at the grain boundaries, and the presence of nano-precipitates ([48]). Three intermediate material parameters (a_1, a_2, a_3) are introduced in this hardening function, they can be determined by using known material parameters as shown in section 4.5. Besides, four other smoothing parameters (n_1, n_2, n_3, n_4) are introduced to better treat the smooth transition characteristics at the initiation and completion during phase transformation.

$$f(\xi) = \begin{cases} \frac{1}{2}\, a_1 \Big(\xi + \frac{\xi^{n_1+1}}{n_1+1} + \frac{(1-\xi)^{n_2+1}}{n_2+1} \Big) + a_3 \xi \ , \ \dot{\xi} > 0, \\ \frac{1}{2}\, a_2 \Big(\xi + \frac{\xi^{n_3+1}}{n_3+1} + \frac{(1-\xi)^{n_4+1}}{n_4+1} \Big) - a_3 \xi \ , \ \dot{\xi} < 0 \end{cases} \tag{4.11}$$

On basis of the proposed Gibbs free energy, following classic thermodynamic principles and standard Coleman-Noll procedure, the constitutive relationship between stress and strain can be obtained as equation (4.12), and the constitutive relationship between entropy and temperature obtained as equation (4.13),

$$\mathbf{h} = -\rho_0 \frac{\partial G}{\partial \boldsymbol{\tau}} = \mathcal{S}\boldsymbol{\tau} + \boldsymbol{\alpha}(T - T_0) + \mathbf{h}^{tr} + \mathbf{h}^{tp} \tag{4.12}$$

$$s = -\rho_0 \frac{\partial G}{\partial T} = \frac{1}{\rho_0} \boldsymbol{\tau} : \boldsymbol{\alpha} + c \ln(\frac{T}{T_0}) - s_0 \tag{4.13}$$

The following reduced form of dissipation inequality (4.14) can be derived by substi-

tution of the aboved two constitutive relationships into Clausius-Planck inequality,

$$-\rho_0 \frac{\partial G}{\partial \mathbf{h}^{tr}} : \mathring{\mathbf{h}}^{tr} - \rho_0 \frac{\partial G}{\partial \mathbf{h}^{tp}} : \mathring{\mathbf{h}}^{tp} - \rho_0 \frac{\partial G}{\partial \xi}\dot{\xi} \geqslant 0 \tag{4.14}$$

4.3.2 Evolution law for transformation strain

This part focuse on the evolution law for transformation strain. Following the maximum dissipation principle, the evolution of transformation strain dissipating the most energy among all the admissible thermodynamic paths is chosen during the entire phase transformation process ([10], [79]). Therefore, it is assumed that the rate change of transformation strain is proportional to the rate change of the martensitic volume fraction ξ, and the direction of which is along the deviatoric direction of the current stress state. Be noted that in the following evolution law the rate applied on top of the transformation strain is the logarithmic rate in order to account for finite deformation. Finally, the explicit evolution law for transformation strain is described as follows,

$$\mathring{\mathbf{h}}^{tr} = \mathbf{\Lambda}\dot{\xi}, \;\; \mathbf{\Lambda} = \begin{cases} \mathbf{\Lambda}_{fwd}, \; \dot{\xi} > 0, \\ \\ \mathbf{\Lambda}_{rev}, \; \dot{\xi} < 0, \end{cases} \tag{4.15}$$

where, $\mathbf{\Lambda}_{fwd}$ is the forward transformation direction tensor, while $\mathbf{\Lambda}_{rev}$ is the reverse transformation direction tensor. They are defined as follows,

$$\mathbf{\Lambda}_{fwd} = \frac{3}{2} H^{cur} \frac{\boldsymbol{\tau}^{\text{eff}'}}{\bar{\tau}^{\text{eff}}}; \quad \Lambda^{rev} = \frac{\mathbf{h}^{tr\text{-}r}}{\xi^r}. \tag{4.16}$$

in the above equations, $\boldsymbol{\tau}^{\text{eff}}$ is the effective stress tensor defined as equation (4.17) using the summation of current stress and internal stress. The main difference in this equation compared to that in the SMA modeling only concerning stable material response is the

using of the effective stress tensor, which means the oriented phase transformation can happen under the condition that even there is no external mechanical load being applied. The evolution law for internal stress tensor $\boldsymbol{\beta}$ is introduced in the later context shortly.

$$\boldsymbol{\tau}^{\text{eff}} = \boldsymbol{\tau} + \boldsymbol{\beta} \tag{4.17}$$

$\boldsymbol{\tau}^{'\text{eff}}$ is the deviatoric part of effective stress tensor defined as $\boldsymbol{\tau}^{'\text{eff}} = \boldsymbol{\tau}^{\text{eff}} - \frac{1}{3}\text{tr}(\boldsymbol{\tau}^{\text{eff}})\ \mathbf{1}$, where $\mathbf{1}$ is the second order identity tensor. The Mises equivalent effective stress $\bar{\boldsymbol{\tau}}^{\text{eff}}$ is calculated as follows,

$$\bar{\boldsymbol{\tau}}^{\text{eff}} = \sqrt{\frac{3}{2}\boldsymbol{\tau}^{'\text{eff}} : \boldsymbol{\tau}^{'\text{eff}}} \tag{4.18}$$

It is common in many of the available models that the magnitude of the inelastic recoverable transformation strain is assumed the same under any stress levels. Such consideration is valid when the applied stress levels are high enough to generate fully oriented martensitic variants. However, self-accommodated martensitic variants are generated when the stress levels are not sufficiently high, which renders the value of transformation strain to be stress dependent. Therefore, the following exponential H^{cur} function based on current effective stress levels is introduced to calculate the value of current transformation strain given an effective stress state, where H^{max} is the maximum (or saturated) value of transformation strain, H^{min} corresponds to an observable TWSME strain for pre-trained SMAs or some SMAs experiencing particular production process such as extrusion and aging under stress. Besides, τ_{crit} denotes a critical stress value below which $H^{cur} = H^{min}$, and k_t is a curve-fitting material parameter.

$$H^{\text{cur}}(\bar{\boldsymbol{\tau}}^{\text{eff}}) = \begin{cases} H^{min} + (H^{max} - H^{min})(1 - e^{-\text{k}_t(\bar{\boldsymbol{\tau}}^{\text{eff}} - \tau_{\text{crit}})}); & \bar{\boldsymbol{\tau}}^{\text{eff}} > \tau_{\text{crit}}, \\ H^{min}; & \bar{\boldsymbol{\tau}}^{\text{eff}} < \tau_{\text{crit}}, \end{cases} \tag{4.19}$$

It is also seen from experimental results that a degradation exists for the value of maximum transformation strain as a result of the accumulation of retained martensite. In order to extend the model capability to capture this phenomenon, a degradation law is proposed for the maximum transformation strain as the following equation, where H_i^{max} and H_f^{max} represent the value of H^{max} before and after the cyclic loading. In addition, λ_1 is a material parameter governing the degradation trend of H^{max}, and ζ^d called the accumulation of orientated martensitic volume fraction is introduced shortly in the later subsection.

$$H^{max} = H_f^{max} + (H_i^{max} - H_f^{max})e^{-\lambda_1 \zeta^d} \tag{4.20}$$

4.3.3 Evolution law for TRIP strain

An evolution law for the TRIP strain is proposed in this subsection in order for the model to capture the irrecoverable strain exhibited by SMAs under cyclic thermomechanical loading. Before the detailed formulation is presented, a major assumption is postulated, i.e., among the total martensitic phase transformation, only the oriented transformation portion contributes to the generation of TRIP. This assumption is built upon the observation on the experimental results that no macroscopic irrecoverable deformations are perceived for untrained SMAs under load-free thermal cycling. An early one-dimensional form of TRIP evolution law was suggested in the work of [9], and a three-dimensional form was proposed by [50]. As it was discussed in the introduction, the generation of TRIP strain is highly affected by the multiaxial stress state, and is quite different from that subjected to uniform stress condition. However, none of the above TRIP evolution laws have addressed this critical feature. Therefore, one of the major contributions of this work is to address the effect of stress multiaxiality on the generation of TRIP. To that end,

the following TRIP evolution law is suggested,

$$\mathring{\mathbf{h}}^{tp} = \mathbf{\Lambda}^{tp}\dot{\xi}, \;\; \mathbf{\Lambda}^{tp} = \begin{cases} \mathbf{\Lambda}^{tp}_{fwd}, & \dot{\xi} > 0, \\ \mathbf{\Lambda}^{tp}_{rev}, & \dot{\xi} < 0, \end{cases} \tag{4.21}$$

in the above equation, $\mathbf{\Lambda}^{p}_{fwd}$ is the forward TRIP direction tensor, and $\mathbf{\Lambda}^{p}_{rev}$ is the reverse one. They have explicit definitions in equation (4.22). Note that the rate applied on top of $\mathbf{h}^{tp}$ is the logarithmic rate in order to consider the finite deformation in the presence of large strains and large rotations.

$$\mathbf{\Lambda}^{tp}_{fwd} = \frac{3}{2}(\frac{H^{cur}}{H^{max}})^2 \frac{\boldsymbol{\tau}'^{\text{eff}}}{\bar{\boldsymbol{\tau}}^{\text{eff}}} \frac{C^p_1 C^p_2}{1 + C^p_2 \zeta^d}; \qquad \mathbf{\Lambda}^{tp}_{rev} = -(\frac{H^{cur}}{H^{max}})^2 \frac{\mathbf{h}^{tr-r}}{\xi^r} \frac{C^p_1 C^p_2}{1 + C^p_2 \zeta^d} \tag{4.22}$$

As a result of its association with the phase transformation, the TRIP strain is proposed to evolve along the same deviatoric direction of the effective stress as the transformation strain. Material parameters C^p_1 and C^p_2 are used to dictate the envolving trend and magnitude for TRIP strain during the cyclic loading. The purpose of using the accumulation of oriented martensitic volume fraction ζ^d is to satisfy the assumption that only the oriented phase transformation contributes to the generation of TRIP strain. The rate form equation (4.21) can be integrated to be expressed as the following explicit form using a logarithmic function,

$$\mathbf{h}^{tp} = \frac{3}{2} \frac{H^{cur}}{H^{max}} C^p_1 \, \frac{\boldsymbol{\tau}'^{\text{eff}}}{\bar{\boldsymbol{\tau}}^{\text{eff}}} \ln\left(1 + C^p_2 \zeta^d\right) \tag{4.23}$$

As it can be seen from this relation, by multiplying C^p_1 with the ratio (H^{cur}/H^{max}) the stress dependent effect is incorporated in these material parameters. As it is shown in the latter results section, utilization of (H^{cur}/H^{max}) and ζ^d in the TRIP evolution law can enable the model to capture the multiaxial TRIP strain evolution under non-uniform stress

condition. Besides, another important quantity ζ^d in this equation is defined as follows,

$$\zeta^d = \int_0^t |\dot{\xi}^d(t)| dt \tag{4.24}$$

in which the oriented martensitic volume fraction ξ^d is calculated as,

$$\xi^d = \frac{H^{cur}}{H^{max}} \xi \tag{4.25}$$

the relation between accumulation of oriented martensitic volume fraction ζ^d and accumulation of total martensitic volume fraction ζ is obtained as follow,

$$\zeta^d = \frac{H^{cur}}{H^{max}} \zeta \tag{4.26}$$

4.3.4 Evolution law for internal stress

In order to meet the proposed goal of capturing the TWSME of trained SMAs under load-free condition, a second-order internal stress term is introduced in this model. As discussed to some extents in the introduction section, during cyclic thermomechanical loading SMAs experience microstructure changes at a stress level below the yielding point, such as pileup of transformation-driven dislocation bands, initiation and growth of micro-voids and micro-cracks, and damage accumulation. These microstructure changes then gradually introduce a local stress field inside the SMA materials, which is effectively described by an internal stress tensor in this model. It is also reasonably assumed the internal stress may never go beyond the material yielding point, thus its magnitude is saturated at a maximum point. Additionally, the evolution direction is determined next. Because the microstructure changes are induced under the external bias mechanical load, the internal stress are assumed being generated in the same direction as the applied stress

field. On the basis of the above discussions, an exponential evolution law is proposed for the internal stress to account for the TWSME as follows,

$$\boldsymbol{\beta} = \sigma_b \, \frac{H^{cur}}{H^{max}} \frac{\boldsymbol{\tau}^{\text{eff}}}{\bar{\boldsymbol{\tau}}^{\text{eff}}} (1 - e^{-\lambda_1 \zeta^d}) \tag{4.27}$$

in which, σ_b is a material parameter representing the maximum (or saturated) magnitude of the internal stress. Similar as the TRIP strain evolution law, the ratio (H^{cur}/H^{max}) and ζ^d are included here to consider the stress multiaxiality effect, and λ_1 is a material parameter controlling the evolution trend.

4.3.5 Transformation function

In this subsection, a transformation function and an associated transformation criterion are defined, upon which the initiation and completion of phase transformation can be determined. By substitution of the evolution law for transformation strain (4.16) and TRIP strain (4.21) into the reduced form of dissipation inequality 4.14, the following equation is obtained,

$$\big(\boldsymbol{\tau} : \boldsymbol{\Lambda} + \boldsymbol{\beta} : \boldsymbol{\Lambda} + \boldsymbol{\tau} : \boldsymbol{\Lambda}^{tp} - \rho_0 \frac{\partial G}{\partial \xi}\big)\dot{\xi} = \pi \dot{\xi} \geqslant 0 \tag{4.28}$$

in which the quantity π is called the general thermodynamic driving force conjugated to ξ in the proposed model. The product by substitution of Gibbs free energy (4.10) into the above equation (4.28) yields the explicit expression for π, where $\Delta\mathcal{S}, \Delta\boldsymbol{\alpha}, \Delta c, \Delta s_0, \Delta u_0$ represent the phase differences between martenstie and austenite of that material property.

$$\begin{aligned} \pi = (\boldsymbol{\tau} + \boldsymbol{\beta}) : \boldsymbol{\Lambda} + \boldsymbol{\tau} : \boldsymbol{\Lambda}^{tp} + \frac{1}{2}\boldsymbol{\tau} : \Delta\mathcal{S}\boldsymbol{\tau} + \boldsymbol{\tau} : \Delta\boldsymbol{\alpha}(T - T_0) + \rho\Delta s_0 T \\ -\rho\Delta c\big[T - T_0 - T\ln(\frac{T}{T_0})\big] - \rho\Delta u_0 - \frac{\partial f}{\partial \xi} \end{aligned} \tag{4.29}$$

Following the model development in [10, 50], it is assumed that the forward (reverse) phase transformation initiates whenever the thermodynamic driving force π $(-\pi)$ reaches a critical value Y $(-Y)$, and π $(-\pi)$ is always below such critical value as long as the forward (reverse) phase transformation is not completed, based on which the following transformation function Φ is defined,

$$\Phi = \begin{cases} \pi - Y, \ \dot{\xi} > 0, \\ \\ -\pi - Y, \ \dot{\xi} < 0, \end{cases} \tag{4.30}$$

A further improvement in the critical value Y is suggested from [47], see equation (4.31), in which Y is constructed to be stress-dependent where a reference critical value Y_0 and an additional parameter D are introduced. Such consideration enables the model to predict different size of hysteresis loops when SMA materials are subjected to various applied stress levels. This capability is provided through capturing the different slopes C_A, C_M in the effective stress-temperature phase diagram.

$$Y(\boldsymbol{\sigma}) = \begin{cases} Y_0 + D\boldsymbol{\sigma} : \boldsymbol{\Lambda}_{\mathit{fwd}}, \ \dot{\xi} > 0, \\ \\ Y_0 + D\boldsymbol{\sigma} : \boldsymbol{\Lambda}_{\mathit{rev}}, \ \dot{\xi} < 0, \end{cases} \tag{4.31}$$

In order for the defined transformation functions and the corresponding transformation criteria to satisfy the principle of maximum dissipation, the following Kuhn-Tucker constraint conditions have to be met,

$$\begin{aligned} \dot{\xi} \geqslant 0; \quad \Phi(\boldsymbol{\tau}, T, \xi) = \ \pi - Y \leqslant 0; \quad \Phi\dot{\xi} = 0; \\ \dot{\xi} \leqslant 0; \quad \Phi(\boldsymbol{\tau}, T, \xi) = -\pi - Y \leqslant 0; \quad \Phi\dot{\xi} = 0; \end{aligned} \tag{4.32}$$

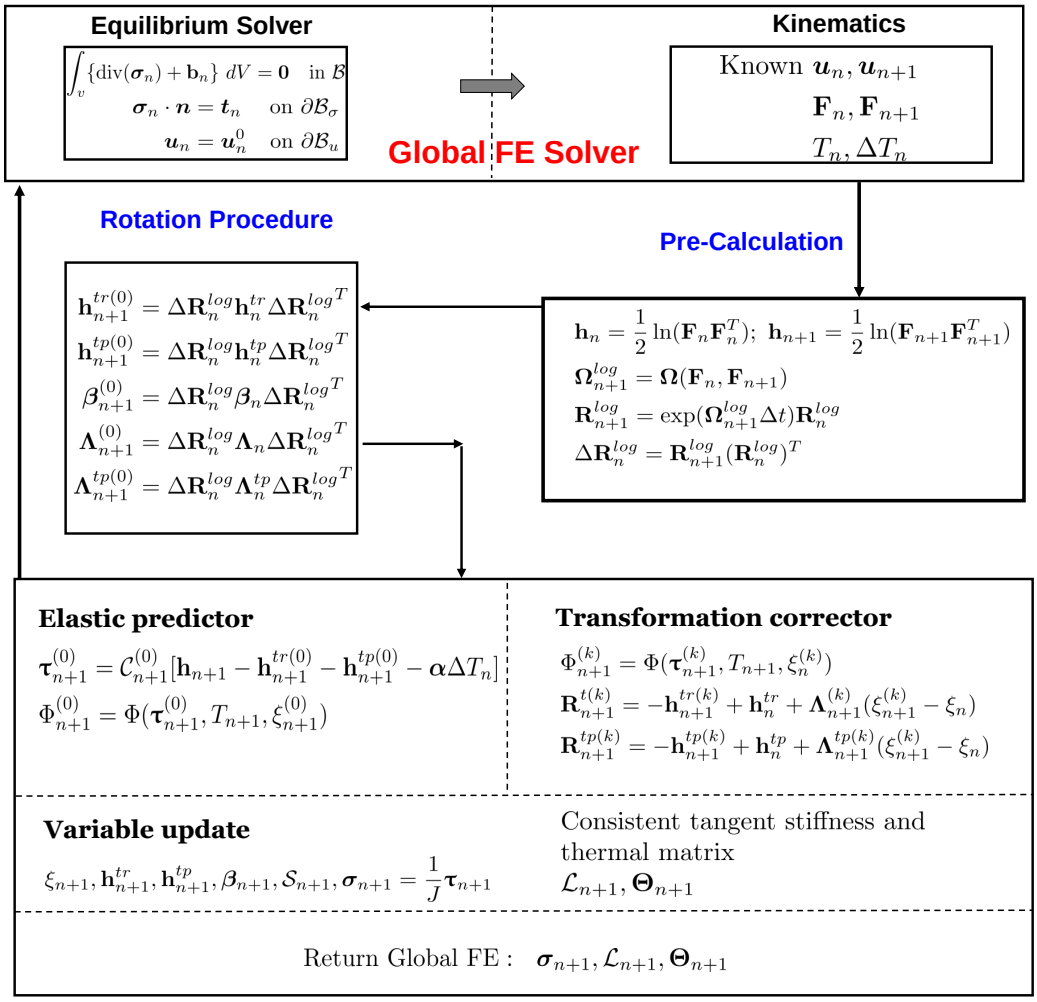

Figure 4.3: Flowchart for the variables used in UMAT integration with the finite element solver.

4.4 Consistent tangent stiffness and thermal matrix

In order for the displacement-based numerical finite element solver to obtain an accurate solutions for the global equilibrium equations using Newton's method with acceptable convergence iterations, the so-called consistent tangent matrices are often required to be provided from the UMAT. A detailed derivation of the consistent tangent stiffness

matrix and the thermal matrix is provided in this section to complete the proposed model. In general, consistent tangent matrices can be formulated in the rate form as equation (4.33), where $\mathcal{L}$ is called the consistent tangent stiffness matrix and Θ is the consistent thermal matrix.

$$\mathring{\boldsymbol{\tau}} = \mathcal{L}\mathring{\mathbf{h}} + \Theta\dot{T} \tag{4.33}$$

applying the logarithmic rate on constitutive equation (4.12) yields,

$$\mathring{\boldsymbol{\tau}} = \mathcal{C}\,[\mathring{\mathbf{h}} - \boldsymbol{\alpha}\dot{T} - (\Delta\mathcal{S}\boldsymbol{\tau} + \Delta\boldsymbol{\alpha}\Delta T + \boldsymbol{\Lambda} + \boldsymbol{\Lambda}^{tp})\dot{\xi}\,] \tag{4.34}$$

taking chain rule differentiation on the transformation function equation (4.30) results in,

$$\dot{\Phi} = \partial_{\boldsymbol{\tau}}\Phi : \mathring{\boldsymbol{\tau}} + \partial_T\Phi\dot{T} + \partial_\xi\Phi\dot{\xi} = 0 \tag{4.35}$$

Upon substituting equation (4.34) into equation (4.35) to eliminate $\mathring{\boldsymbol{\tau}}$ and solving it for $\dot{\xi}$, the following expression for $\dot{\xi}$ can be obtained,

$$\dot{\xi} = -\frac{\partial_{\boldsymbol{\tau}}\Phi : \mathcal{C}\mathring{\mathbf{h}} + (\partial_T\Phi - \partial_{\boldsymbol{\tau}}\Phi : \mathcal{C}\boldsymbol{\alpha})\dot{T}}{\partial_\xi\Phi - \partial_{\boldsymbol{\tau}}\Phi : \mathcal{C}(\Delta\mathcal{S}\boldsymbol{\tau} + \boldsymbol{\Lambda} + \boldsymbol{\Lambda}^{tp} + \Delta\boldsymbol{\alpha}\Delta T)} \tag{4.36}$$

The phase difference of thermal expansion coefficients $\Delta\boldsymbol{\alpha}$ between martensite and austenite phase is negligible, for the sake of brevity, it is neglected. After substituting equation(4.36) back into the rate form constitutive equation(4.34) to eliminate $\dot{\xi}$, the final explicit expression corresponding to equation (4.33) can be obtained as follows,

$$\begin{aligned}\mathring{\boldsymbol{\tau}} \quad = \quad & \Big[\mathcal{C} + \frac{[\mathcal{C}(\Delta\mathcal{S}\boldsymbol{\tau} + \boldsymbol{\Lambda} + \boldsymbol{\Lambda}^{tp})] \otimes [\mathcal{C}\partial_{\boldsymbol{\tau}}\Phi]}{\partial_\xi\Phi - \partial_{\boldsymbol{\tau}}\Phi : \mathcal{C}(\Delta\mathcal{S}\boldsymbol{\tau} + \boldsymbol{\Lambda} + \boldsymbol{\Lambda}^{tp})}\Big]\mathring{\mathbf{h}} \quad + \\ & \Big[-\mathcal{C}\boldsymbol{\alpha} + \frac{\mathcal{C}(\Delta\mathcal{S}\boldsymbol{\tau} + \boldsymbol{\Lambda} + \boldsymbol{\Lambda}^{tp})(\partial_T\Phi - \partial_{\boldsymbol{\tau}}\Phi : \mathcal{C}\boldsymbol{\alpha})}{\partial_\xi\Phi - \partial_{\boldsymbol{\tau}}\Phi : \mathcal{C}(\Delta\mathcal{S}\boldsymbol{\tau} + \boldsymbol{\Lambda} + \boldsymbol{\Lambda}^{tp})}\Big]\dot{T}\end{aligned} \tag{4.37}$$

in which the consistent tangent stiffness matrix $\mathcal{L}$ is,

$$\mathcal{L} = \mathcal{C} + \frac{[\mathcal{C}(\Delta\mathcal{S}\boldsymbol{\tau} + \boldsymbol{\Lambda} + \boldsymbol{\Lambda}^{tp})] \otimes [\mathcal{C}\partial_{\boldsymbol{\tau}}\Phi]}{\partial_{\xi}\Phi - \partial_{\boldsymbol{\tau}}\Phi : \mathcal{C}(\Delta\mathcal{S}\boldsymbol{\tau} + \boldsymbol{\Lambda} + \boldsymbol{\Lambda}^{tp})} \tag{4.38}$$

and the consistent thermal matrix Θ is,

$$\Theta = \frac{\mathcal{C}(\Delta\mathcal{S}\boldsymbol{\tau} + \boldsymbol{\Lambda} + \boldsymbol{\Lambda}^{tp})(\partial_T\Phi - \partial_{\boldsymbol{\tau}}\Phi : \mathcal{C}\boldsymbol{\alpha})}{\partial_{\xi}\Phi - \partial_{\boldsymbol{\tau}}\Phi : \mathcal{C}(\Delta\mathcal{S}\boldsymbol{\tau} + \boldsymbol{\Lambda} + \boldsymbol{\Lambda}^{tp})} - \mathcal{C}\boldsymbol{\alpha} \tag{4.39}$$

In order to fully determine the explicit values for $\mathcal{L}$ and Θ during the implementation section for the proposed model, the explicit expressions of the following terms $\partial_{\boldsymbol{\tau}}\Phi$, $\partial_{\xi}\Phi$, $\partial_T\Phi$ used in above equations can be calculated by using the symbolic calculation toolbox provided in MATLAB.

4.5 Model calibration

In this section, the material parameters utilized in this proposed model are identified from a set of calibration experiments, which in general can be categorized into three groups, i.e., the key material parameters, smooth hardening parameters, and TRIP and internal stresses parameters. Note that the strain measure used here is true (or logarithmic) strain rather than engineering (or infinitesimal) strain.

First, material constants such as the elastic modulus (E_A, E_M) of austenite and martensite can be obtained by calculating the slopes at martensitic phase and austenite phase from uniaxial mechanical loading-unloading experiment, i.e., pseudoelastic response see Figure 4.4(a). Poisson's ratios ν_A and ν_B are usually assumed as 0.33 for metallic materials. In order to construct the phase diagram, thermal cycling of the material under constant uniaxial tensile stress, i.e., actuation response see Figure 4.4(b), is performed, by which critical transformation temperatures (M_s^{τ}, M_f^{τ}, A_s^{τ}, A_f^{τ}) and transformation strain $H^{cur}(\tau)$ at current stress level are measured. Three such experiments at different stress

levels (τ_1, τ_2, τ_3) are performed. By using these collected temperature and transformation strain information, the phase diagram and the H^{cur} curve can be constructed, see Figure 4.5. Therefore, phase diagram related stress influence coefficients (C_A, C_M), phase transformation temperatures (M_s, M_f, A_s, A_f) at zero stresses, are determined. In addition, material parameters related to H^{cur} curve $(H^{min}, H^{max}, k_t, \tau_{\text{crit}})$ are also obtained. Secondly, the smooth hardening related coefficients (n_1, n_2, n_3, n_4) are determined by best matching the smoothness corner at the initiation and completion during phase transformation. Thermal expansion coefficients assuming no phase differences ,i.e., $\alpha_A = \alpha_M$ can be calibrated through an actuation response.

In order to calibrate TRIP material parameters (C_1^p, C_2^p), cyclic actuation response at a saturation stress level is performed, see Figure 4.6(a). TRIP strain with respect to the number of loading cycle is measured. By integrating the rate form TRIP strain evolution equation (4.22), the algebraic form can be obtained as equation (4.40). The ratio term H^{cur}/H^{max} is presented to incorporate the stress dependency effect on TRIP parameters (C_1^p, C_2^p). As the austenite phase is fully transformed into oriented martensite phase under the saturation stress value, the value of ratio is $H^{cur}/H^{max} = 1$, and the accumulation of orientated martensitic volume fraction equals to the total one $\zeta^d = \zeta$.

$$h^{tp} = \frac{H^{cur}}{H^{max}} C_1^p \ln(1 + C_2^p \zeta^d) \tag{4.40}$$

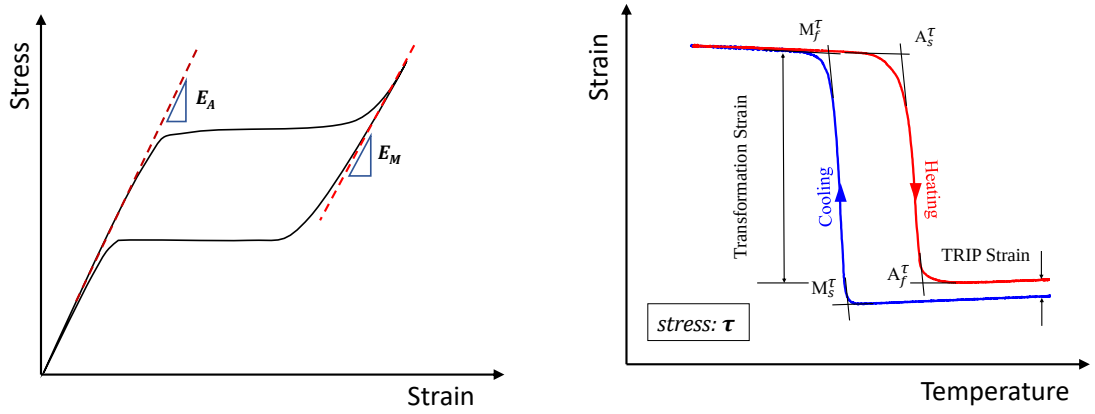

(a) (b)

Figure 4.4: Experiments utilized for the calibration of model parameters. (a) Calibration of elastic modulus for austenite and martensite from uniaxial pseudoelastic experiment. (b) Calibration of phase diagram from uniaxial actuation experiment.

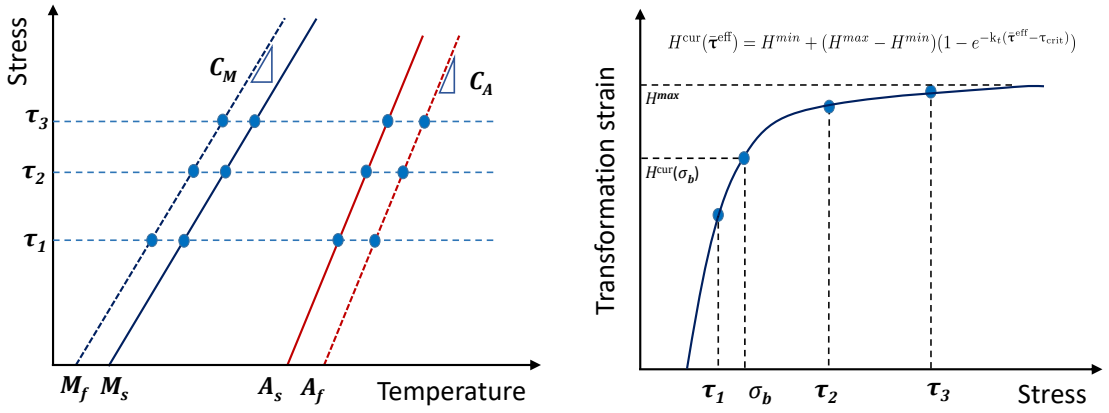

(a) (b)

Figure 4.5: Calibration of material parameters governing stable material response. (a) Phase diagram using actuation experiments at three different stress levels. (b) H^{cur} curve.

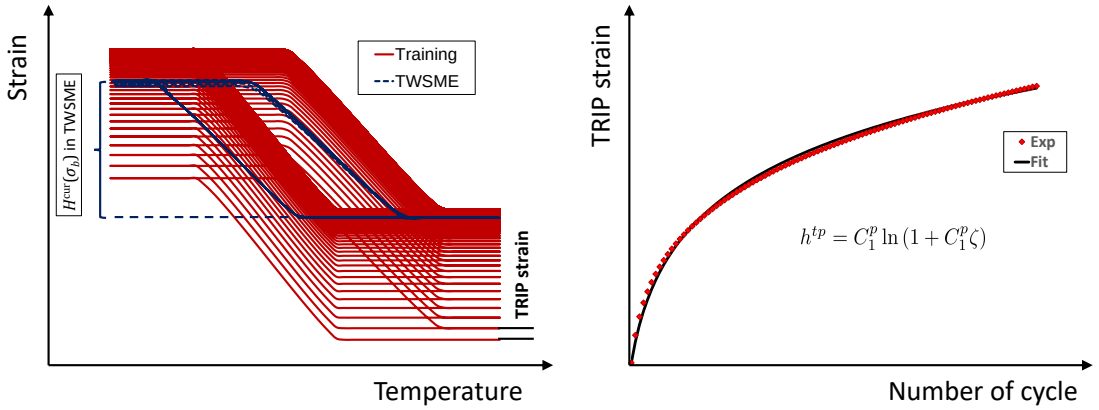

(a) (b)

Figure 4.6: Calibration of material parameters governing TRIP and TWSME features. (a) Cyclic actuation response with TWSME curve at load-free condition. (b) Calibration of TRIP parameters based on TRIP strain accumulation with respect to number of loading cycle.

Therefore, equation (4.40) can be further reduced into equation (4.41). Material parameters related to TRIP (C_1^p, C_2^p) can thus be calibrated by best fitting the TRIP strain accumulation curve in Figure 4.6(b).

$$h^{tp} = C_1^p \ln(1 + C_2^p \zeta) \tag{4.41}$$

Next, internal stress related material parameters (σ_b, λ_1) are calibrated from the TWSME response. The internal stress is response for the generation of TWSME at load-free condition. For example, TWSME transformation strain $H^{cur}(\sigma_b)$ is generated after the thermal cycling training procedure in Figure 4.6(a). Based on the H^{cur} curve from Figure 4.5(b), the effective stress value of τ^{eff} is required in order to produce this transformation strain. At load-free condition, $\tau^{\text{eff}} = \sigma_b$. Thus the value of σ_b can be obtained by using the

following condition,

$$H^{\text{cur}}(\sigma_b) = H^{min} + (H^{max} - H^{min})(1 - e^{-k_t(\sigma_b - \tau_{\text{crit}})}) \tag{4.42}$$

The explicit calculation of σ_b is as follow,

$$\sigma_b = \tau_{\text{crit}} + \frac{1}{k_t} \ln \big(\frac{H^{max} - H^{min}}{H^{max} - H^{cur}(\sigma_b)}\big) \tag{4.43}$$

Parameter λ_1 controls the evolving trend of internal stress into its saturation value. Usually, $\lambda_1 = 0.01 \sim 1$ is acceptable, $\lambda_1 = 0.1$ is used in the current work.

There are also seven intermediate material parameters $(\rho_0\Delta s_0, \rho_0\Delta u_0, a_1, a_2, a_3, Y_0, D)$ utilized in the proposed model, which can be calculated based on the above known parameters. Their detailed derivations are provided in [47, 121], here they are reviewed to complete the model calibration.

$$\begin{cases} a_1 = \rho_0\Delta s_0(M_f - M_s); \\ a_2 = \rho_0\Delta s_0(A_s - A_f) \\ a_3 = \dfrac{1}{4}\, a_2(1 + \dfrac{1}{n_3 + 1}) - \dfrac{1}{4}\, a_1(1 + \dfrac{1}{n_1 + 1}) \\ \rho_0\Delta u_0 = \dfrac{1}{2}\rho\Delta s_0(M_s + A_f) \\ Y_0 = \dfrac{1}{2}\rho_0\Delta s_0(M_s - A_f) - a_3 \\ D = \dfrac{(C_M - C_A)\big[H^{cur} + \tau\partial_\tau H^{cur} + \tau\Delta\mathcal{S}\big] + +(C_M + C_A)(\Lambda^{tp} + \tau\partial_\tau\Lambda^{tp})}{(C_M + C_A)(H^{cur} + \tau\partial_\tau H^{cur})} \\ \rho_0\Delta s_0 = -\dfrac{2C_M C_A\big[H^{cur} + \tau\partial_\tau H^{cur} + \tau\Delta\mathcal{S}\big]}{C_M + C_A} \end{cases} \tag{4.44}$$

4.6 Implementation

This section discusses the implementation of the above proposed model into a numerical environment using an user-defined material subroutine (UMAT) for solving boundary value problems. The used variables in the UMAT is presented as a flowchart in Figure 4.3. This implementation procedure follows the knowledge of return mapping algorithm (RMA) presented in the available publications ([78, 48]). In general, the goal of the UMAT is, given an increment of strain and temperature from the numerical solver, using the constitutive relationships (4.12) and (4.13) to calculate a stress output under the condition that the internal state variables conform with the Kuhn-Tucker consistency constraints (4.32). The implementation of constitutive models consists of two major procedures towards this goal, one is called Thermoelastic-predictor, and the other is Transformation-corrector. It is worthy to point out that the input variables used for this implementation from the finite element solver are only the temperature and its increment (T_n, ΔT_n), and deformation gradients at current and next step ($\mathbf{F}_n$, $\mathbf{F}_{n+1}$). As it was discussed in [121], such considerations allow the model to account for the finite deformations in SMA components, at the same time enable the model to get rid of the accumulated stress errors as a result of using other non-integrable objective rates. The effects of such accumulated stress errors on the cyclic response of SMAs is discussed in detail by [121].

A Pre-calculation and a rotation procedure are employed before calling the thermoelastic prediction and transformation correction steps. In the Pre-calculation procedure, the total strain at current and next step ($\mathbf{h}_n$, $\mathbf{h}_{n+1}$) are calculated based on ($\mathbf{F}_n$, $\mathbf{F}_{n+1}$) using equation (3.8). The incremental rotation tensor $\Delta\mathbf{R}_n^{log}$ based on the logarithmic rate can be calculated by using the exponential map scheme described in [90]. In the rotation procedure, the tensorial variables stored as solution-dependent quantities including $\mathbf{h}_n$, $\mathbf{h}_n^{tr}$, $\mathbf{h}_n^{tp}$, $\boldsymbol{\beta}_n$, $\boldsymbol{\Lambda}_n$, and $\boldsymbol{\Lambda}_n^{tp}$ are rotated from previous n^{th} configuration to cur-

rent $n+1^{th}$ configuration using $\Delta\mathbf{R}_n^{log}$, thus, to preserve the so-called principle of objectivity. To proceed with the thermoelastic-predictor step, the internal state variables $\boldsymbol{\Upsilon}_{n+1}^{(0)} = \{\mathbf{h}_{n+1}^{tr(0)}, \mathbf{h}_{n+1}^{tp(0)}, \boldsymbol{\beta}_{n+1}^{(0)}, \xi_{n+1}^{(0)}\}$[1] at $(n+1)^{th}$ step are assumed the same as $\boldsymbol{\Upsilon}_n$ for the initial thermoelastic evaluation. In the case that the Kuhn-Tucker consistency condition is violated, i.e., $\Phi_{n+1}^{(0)} \geqslant 0$, the transformation correction procedure is initiated to attain updated internal state variables to regain consistency. Otherwise, the current n+1 step is detected as a thermoelastic response, i.e., $\boldsymbol{\Upsilon}_{n+1} = \boldsymbol{\Upsilon}_{n+1}^{(0)}$, the UMAT skips the transformation correction step and continues the rest procedures. A detailed description of implementation is presented in the following context.

4.6.1 Thermoelastic prediction

This part is a detailed description of the thermoelastic prediction. Take $(n+1)^{th}$ step as an example for illustration. The total strain $\mathbf{h}_{n+1}$ and temperature T_{n+1} are obtained from the pre-calculation procedure, and the initial internal state variables $\boldsymbol{\Upsilon}_{n+1}^{(0)}$ are assumed the same as $\boldsymbol{\Upsilon}_n$ for the initial consistency evaluation, i.e.,

$$\mathbf{h}_{n+1}^{tr(0)} = \mathbf{h}_n^{tr}; \quad \mathbf{h}_{n+1}^{tp(0)} = \mathbf{h}_n^{tp}; \quad \boldsymbol{\beta}_{n+1}^{(0)} = \boldsymbol{\beta}_n; \quad \xi_{n+1}^{(0)} = \xi_n \tag{4.45}$$

on the basis of the above information, the guessed stress value $\boldsymbol{\tau}_{n+1}^{(0)}$ is calculated through the constitutive equation (4.12),

$$\boldsymbol{\tau}_{n+1}^{(0)} = \mathcal{C}_{n+1}^{(0)}\Big[\mathbf{h}_{n+1} - \mathbf{h}_{n+1}^{tr(0)} - \mathbf{h}_{n+1}^{tp(0)} - \boldsymbol{\alpha}_{n+1}^{(0)}(T_{n+1} - T_0)\Big] \tag{4.46}$$

[1] $(\cdot)^{(k)}$ represent the local value of that variable at the k^{th} iteration in transformation correction procedure, here $k = 0$ means that this is an initial guess value in thermoelastic prediction procedure.

the initial value of transformation function $\Phi_{n+1}^{(0)}$ in thermoelastic procedure can be evaluated base on equations (4.29) and (4.30) as follow,

$$\Phi_{n+1}^{(0)} = \Phi(\boldsymbol{\tau}_{n+1}^{(0)}, T_{n+1}, \boldsymbol{\Upsilon}_{n+1}^{(0)}) \tag{4.47}$$

If the transformation consistency constraints are preserved, i.e., the initial value of transformation function $\Phi_{n+1}^{(0)} \leqslant 0$ [2], no phase transformation happens in the materials at the current state, and the current step is detected as a thermoelastic step. If the transformation criterion is violated, i.e. $\Phi_{n+1}^{(0)} \geqslant 0$, transformation corrector procedure is activated in order to restore the transformation constraints (4.32) via seeking updated internal state variables $\boldsymbol{\Upsilon}_{n+1}^{(k)}$.

4.6.2 Transformation correction

This part focuses on the iterative transformation correction procedure seeking a set of updated internal state variables to regain the transformation consistency conditions, i.e., $\Phi_{n+1}^{(k)} \leqslant 0$. Take the k^{th} iteration as an example, the objective is to solve the system of nonlinear equations summarized in equations (4.48), (4.49) and (4.50), where the residuals in those rate form evolution equations for transformation strain (4.15) and TRIP strain (4.21) can be reformulated using the discretized linearization as equations (4.49) and (4.50),

$$\Phi_{n+1}^{(k)} \;=\; \Phi(\boldsymbol{\tau}_{n+1}^{(k)}, T_{n+1}, \xi_{n+1}^{(k)}) \tag{4.48}$$

$$\mathbf{R}_{n+1}^{tr(k)} = -\mathbf{h}_{n+1}^{tr(k)} + \mathbf{h}_{n}^{tr} + \boldsymbol{\Lambda}_{n+1}^{(k)}(\xi_{n+1}^{(k)} - \xi_n) \tag{4.49}$$

$$\mathbf{R}_{n+1}^{tp(k)} = -\mathbf{h}_{n+1}^{tp(k)} + \mathbf{h}_{n}^{tp} + \boldsymbol{\Lambda}_{n+1}^{tp(k)}(\xi_{n+1}^{(k)} - \xi_n) \tag{4.50}$$

[2] Usually a small value 'tol' is used for $\Phi_{n+1}^{(0)} \leqslant$ 'tol' evaluation, 'tol' is acceptable to be 10^{-6} or a even smaller value.

The goal, i.e., regaining the consistency condition, then becomes to satisfy the following convergence inequalities, in which 'tol' means a small convergence value such as 10^{-6}.

$$|\xi_{n+1}^{(k)} - \xi_n| \leqslant \text{tol} \; ; \; |\mathbf{h}_{n+1}^{tr(k)} - \mathbf{h}_{n+1}^{tr}| \leqslant \text{tol} \; ; \; |\mathbf{h}_{n+1}^{tp(k)} - \mathbf{h}_{n+1}^{tp}| \leqslant \text{tol} \tag{4.51}$$

A standard Newton-Raphson iteration procedure can be utilized to solve the above non-linear system of equations as follows, the first term in the right-hand side of this set of equations is the inverse of the Jacobian matrix,

$$\begin{bmatrix} \Delta\xi_{n+1}^{(k)} \\ \Delta\mathbf{h}_{n+1}^{tr(k)} \\ \Delta\mathbf{h}_{n+1}^{tp(k)} \end{bmatrix} = - \begin{bmatrix} \frac{\partial\Phi_{n+1}^{(k)}}{\partial\xi} & \frac{\partial\Phi_{n+1}^{(k)}}{\partial\mathbf{h}^{tr}} & \frac{\partial\Phi_{n+1}^{(k)}}{\partial\mathbf{h}^{tp}} \\ \frac{\partial\mathbf{R}_{n+1}^{tr(k)}}{\partial\xi} & \frac{\partial\mathbf{R}_{n+1}^{tr(k)}}{\partial\mathbf{h}^{tr}} & \frac{\partial\mathbf{R}_{n+1}^{tr(k)}}{\partial\mathbf{h}^{tp}} \\ \frac{\partial\mathbf{R}_{n+1}^{tp(k)}}{\partial\xi} & \frac{\partial\mathbf{R}_{n+1}^{tp(k)}}{\partial\mathbf{h}^{tr}} & \frac{\partial\mathbf{R}_{n+1}^{tp(k)}}{\partial\mathbf{h}^{tp}} \end{bmatrix}^{-1} \begin{bmatrix} \Phi_{n+1}^{(k)} \\ \mathbf{R}_{n+1}^{tr(k)} \\ \mathbf{R}_{n+1}^{tp(k)} \end{bmatrix} \tag{4.52}$$

During each k^{th} iteration of the Newton-Raphson precedure, the following updated values for next $k + 1^{th}$ iteration are obtained for the internal state variables,

$$\begin{bmatrix} \xi_{n+1}^{(k+1)} \\ \mathbf{h}_{n+1}^{tr(k+1)} \\ \mathbf{h}_{n+1}^{tp(k+1)} \end{bmatrix} = \begin{bmatrix} \xi_{n+1}^{(k)} \\ \mathbf{h}_{n+1}^{tr(k)} \\ \mathbf{h}_{n+1}^{tp(k)} \end{bmatrix} + \begin{bmatrix} \Delta\xi_{n+1}^{(k)} \\ \Delta\mathbf{h}_{n+1}^{tr(k)} \\ \Delta\mathbf{h}_{n+1}^{tp(k)} \end{bmatrix} \tag{4.53}$$

The Newton-Raphson procedure iterates a maximum number of iterations until the convergence criterion in equation (4.51) is satisfied. Otherwise, it exits with an error message and the current finite element increment step stops, which indicates a further check on the Jacobian matrix is needed. Once the converged values at k^{th} iteration $\{\mathbf{h}_{n+1}^{tr(k+1)}, \mathbf{h}_{n+1}^{tp(k+1)}, \xi_{n+1}^{(k+1)}\}$ are accepted as the final value for the current material state, the current transformation corrector step is detected as finished.

4.7 Results and discussions

In this section, several BVPs are analyzed to test the proposed model capabilities under both pseudoelastic and actuation loading conditions over a wide range of SMA material systems. The first BVP is a $Ni_{40}Ti_{50}Cu_{10}$ (at.%) SMA under uniaxial cyclic pseudoelastic loading, in which the accumulation of TRIP strain with respect to number of loading cycle and stress levels required to initiate phase transformation are analyzed. The second BVP includes a $Ni_{49.9}Ti_{50.1}$ (at.%) and a $Ni_{50.3}Ti_{29.7}Hf_{20}$ (at%) SMA under uniaxial cyclic actuation loading wherein the load-free TWSME for both material systems after training is simulated. Finally, a $Ni_{60}Ti_{40}$ (wt.%) plate actuator with a centric hole is chosen to test the model capability to capture the multiaxial TRIP evolution under non-uniform stress state. The simulation results for these BVPs are obtained through the commercial finite element software Abaqus, into which the constitutive response of SMAs described above is implemented as a UMAT.

Table 4.1: Summary of closest point return mapping algorithm.

1.*Initialization*

- Conduct pre-calculation and rotation procedures.
- $k=0; \xi_{n+1}^{(0)}=\xi_n; \mathbf{h}_{n+1}^{tr(0)}=\mathbf{h}_n^{tr}; \mathbf{h}_{n+1}^{tp(0)}=\mathbf{h}_n^{tp}; \boldsymbol{\beta}_{n+1}^{(0)}=\boldsymbol{\beta}_n$

2.*Thermoelastic predictor*

- $\boldsymbol{\tau}_{n+1}^{(0)}=\mathcal{C}_{n+1}^{(0)}[\mathbf{h}_{n+1}-\mathbf{h}_{n+1}^{tr(0)}-\mathbf{h}_{n+1}^{tp(0)}-\boldsymbol{\alpha}(T_{n+1}-T_0)]$
- Calculate $\Phi_{n+1}^{(k)}$.
- IF $\Phi_{n+1}^{(0)} \leqslant tol$, GOTO 4 (thermoelastic response).
- IF $\Phi_{n+1}^{(0)} > tol$, GOTO 3 (transformation happens).

3.*Transformation Corrector*

- Calculate residual matrix

  $\mathbf{R}_{n+1}^{tr(k)}=-\mathbf{h}_{n+1}^{tr(k)}+\mathbf{h}_n^{tr}+\boldsymbol{\Lambda}_{n+1}^{(k)}(\xi_{n+1}^{(k)}-\xi_n)$
  $\mathbf{R}_{n+1}^{tp(k)}=-\mathbf{h}_{n+1}^{tp(k)}+\mathbf{h}_n^{tp}+\boldsymbol{\Lambda}_{n+1}^{tp(k)}(\xi_{n+1}^{(k)}-\xi_n)$
  $\Phi_{n+1}^{(k)} \ =\Phi(\boldsymbol{\tau}_{n+1}^{(k)}, T_{n+1}, \xi_{n+1}^{(k)})$
- Perform Newton-Raphson iterations in equation (4.52) to obtain $\Delta\xi_{n+1}^{(k)}, \Delta\mathbf{h}_{n+1}^{tr(k)}, \Delta\mathbf{h}_{n+1}^{tp(k)}$.
- Update variables $\xi_{n+1}^{(k+1)}, \mathbf{h}_{n+1}^{tr(k+1)}, \mathbf{h}_{n+1}^{tp(k+1)}, \mathcal{S}_{n+1}^{(k+1)}$

  $\xi_{n+1}^{(k+1)}=\xi_{n+1}^{(k)}+\Delta\xi_{n+1}^{(k)}$
  $\mathbf{h}_{n+1}^{tr(k+1)}=\mathbf{h}_{n+1}^{tr(k)}+\Delta\mathbf{h}_{n+1}^{tr(k)}$
  $\mathbf{h}_{n+1}^{tp(k+1)}=\mathbf{h}_{n+1}^{tp(k)}+\Delta\mathbf{h}_{n+1}^{tp(k)}$
  $\mathcal{S}_{n+1}^{(k+1)}=\mathcal{S}^A+\xi_{n+1}^{(k+1)}\Delta\mathcal{S}$
- IF $\Phi_{n+1}^{(k+1)} \geqslant tol$, GOTO step 3, next local iteration $k=k+1$.

  ELSE GOTO step 4, EXIT

4.*Calculate consistent stiffness matrix $\mathcal{L}$ and thermal matrix $\boldsymbol{\Theta}$.*

- $\mathcal{L}=\mathcal{C}+\dfrac{[\mathcal{C}(\Delta\mathcal{S}\boldsymbol{\tau}+\boldsymbol{\Lambda}+\boldsymbol{\Lambda}^{tp})]\otimes[\mathcal{C}\partial_{\boldsymbol{\tau}}\Phi]}{\partial_\xi\Phi-\partial_{\boldsymbol{\tau}}\Phi:\mathcal{C}(\Delta\mathcal{S}\boldsymbol{\tau}+\boldsymbol{\Lambda}+\boldsymbol{\Lambda}^{tp})}$
- $\boldsymbol{\Theta}=\dfrac{\mathcal{C}(\Delta\mathcal{S}\boldsymbol{\tau}+\boldsymbol{\Lambda}+\boldsymbol{\Lambda}^{tp})(\partial_T\Phi-\partial_{\boldsymbol{\tau}}\Phi:\mathcal{C}\boldsymbol{\alpha})}{\partial_\xi\Phi-\partial_{\boldsymbol{\tau}}\Phi:\mathcal{C}(\Delta\mathcal{S}\boldsymbol{\tau}+\boldsymbol{\Lambda}+\boldsymbol{\Lambda}^{tp})}-\mathcal{C}\boldsymbol{\alpha}$

5.*Update* ζ_{n+1}^d and $\boldsymbol{\beta}_{n+1}$

- $\zeta_{n+1}^d=\zeta_n^d+\dfrac{H_{n+1}^{cur}}{H^{max}}|\xi_{n+1}-\xi_n|$
- $\boldsymbol{\beta}_{n+1}=\sigma_b\dfrac{\boldsymbol{\tau}_{n+1}^{\text{eff}}}{\bar{\boldsymbol{\tau}}_{n+1}^{\text{eff}}}(1-e^{-\lambda_1\zeta_{n+1}^d})$

6.Exit UMAT and proceed to the global FE solver for the next increment

Table 4.2: Material parameters for NiTiCu SMA in uniaxial cyclic pseudoelastic loading.

Type	Parameter	Value	Parameter	Value
Key material parameters 15	E_A	41 [GPa]	C_A	5.5 [MPa/K]
	E_M	22 [GPa]	C_M	5.5 [MPa/K]
	$\nu_A = \nu_M$	0.33	M_s	237 [K]
	$\alpha_A = \alpha_M$	1.0×10^{-5} [K^{-1}]	M_f	217.5 [K]
	$H_i^{\max}$	3.8%	A_s	254 [K]
	$H_f^{\max}$	3.8%	A_f	282 [K]
	$H^{\min}$	0%	k_t	N/A
	τ_{crit}	0 [MPa]		
Smooth hardening parameters 4	n_1	0.15	n_3	0.25
	n_2	0.17	n_4	0.15
TRIP parameters 4	σ_b	100 [MPa]	λ_1	0.25
	C_1^p	2.1×10^{-2}		
	C_2^p	0.17		

4.7.1 Uniaxial pseudoelastic loading case

The first BVP describes a $Ni_{40}Ti_{50}Cu_{10}$ (at.%) SMA wire under uniaxial pseudoelastic cyclic loading. A bias mechanical load is applied in the longitudinal wire direction from 0 MPa up to a maximum value of 550 MPa then unloaded, during which the temperature is kept constant at 360 K. Such loading path is repeated for 50 cycles. The NiTiCu SMA wire experiences a stress-induced forward phase transformation during the loading regime followed by a reverse phase transformation at the unloading. The material parameters used in this simulation are listed in table 4.2 based on the calibration on experimental data.

The cyclic stress-strain curve acquired by the proposed model is compared against the available experimental data reported in [96]. As shown in Figure 4.7, the NiTiCu SMA accumulates a large amount of irrecoverable TRIP strain from the 1^{st} cycle to the

50^{th} cycle, the TRIP strain result is plotted with respect to the number of loading cycle in Figure 4.8. It can be seen that the TRIP strain grows drastically within the initial 30 loading cycles then stabilizes in a stationary increasing trend thereafter. The accumulated TRIP strain in the 1^{st} cycle is about 0.6% and grows to around 6% after 30 cycles. The predicted TRIP accumulation result is shown in good agreement with the experimental data. Apart from the irrecoverable TRIP strain, the model is also able to capture the experimentally observed decreasing stress levels at which the forward phase transformation initiates. This model capability is achieved by introducing the internal stress in the model formulation. Refer to its evolution law in equation (4.27), as the internal stress is accumulated with an exponential manner with respect to the number of loading cycle, and the required effective stress level $\boldsymbol{\tau}^{\text{eff}}$ is the same, the accumulated internal stress then decreases the needed external stress level to start the phase transformation. It is shown in this BVP that the proposed model not only predicted the TRIP strain accumulation in good agreement with the experimental result, but also captured the intrinsic feature that the stress level needed to initiate the phase transformation decreases with respect to the number of loading cycle.

4.7.2 Uniaxial actuation loading case

In this section, BVPs for two SMA material compositions, i.e., $Ni_{49.9}Ti_{50.1}$ (at%) and $Ni_{50.3}Ti_{29.7}Hf_{20}$ (at%), subjected to uniaxial cyclic actuation loading are analyzed. Among these two BVPs the NiTi is a classical type of SMA material system having their critical phase transforming temperatures close to room temperature range, while NiTiHf belongs to the so-called high-temperature SMA category with their phase transformation around 100 °C that can function under very extreme environments. These two BVPs are chosen to check the fidelity of model over different SMA material system. Recall one of the proposed capabilities of the presented model is to capture the TWSME for trained

SMAs, the load-free thermal cycling response of the SMAs after thermomechancial training in these two BVPs are also examined and compared to available experimental data.

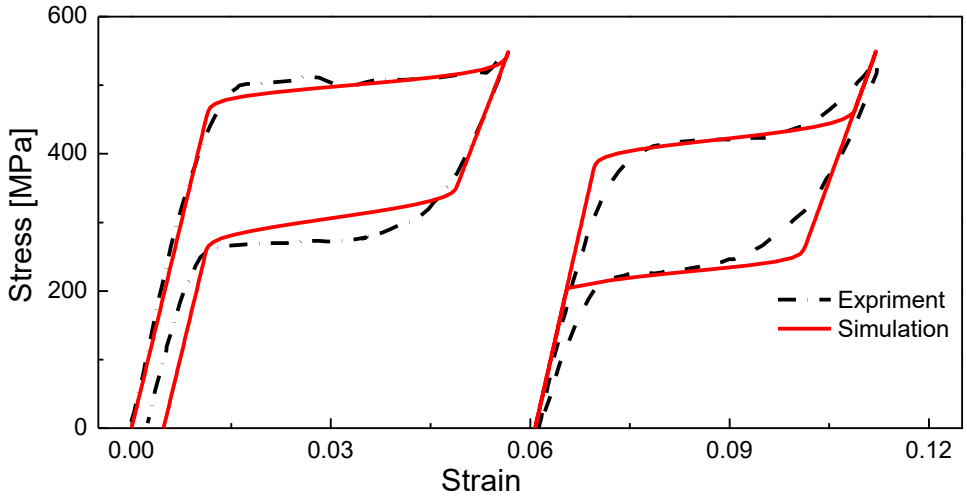

Figure 4.7: The 1^{st} and 50^{th} pseudoelastic loading cycle of a NiTi SMA wire subjected to a unaxial tensile stress up tp 550 MPa.

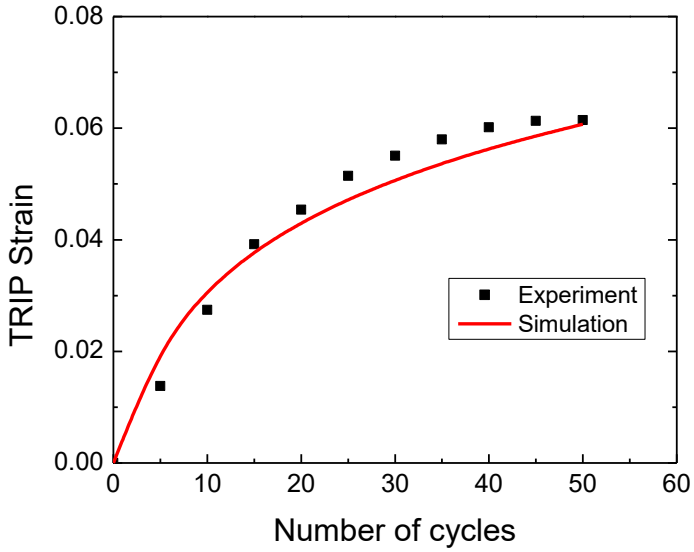

Figure 4.8: Accumulation of transformation-induced plastic strain for NiTi with 50 cycles

In the NiTi case, the SMA dogbone specimen was subjected to a 100 thermal cycling between 310 K and 440 K under a constant 200 MPa mechanical load. After the 100 training cycles, the bias load was removed, and the final thermal cycling was performed to check the TWSME response under load-free condition. The material parameters used by the proposed model to simulate this experiment are listed in table 4.3. Similar to the experimental procedure in the case of NiTi, the NiTiHf dogbone specimen was loaded under 200 MPa and experienced a 100 thermal cycling between 310 K and 580 K. The load-free TWSME was also checked after the thermomechanical training cycles. The material parameters used to simulate the NiTiHf actuation response are listed in table 4.4. The experimental data used for comparison in this section were initially reported in [3].

The simulated cyclic actuation response by the proposed model are summarized in Figure 4.9 for NiTi SMA and in Figure 4.10 for NiTiHf SMA. In the NiTi case, the results for specific training cycle 1, cycle 10, cycle 20, cycle 40, cycle 70, and cycle 100 are selected and compared to the experiment results. It is shown that the transformation characteristics in these selected training cycles, including transformation temperatures, transformation train magnitude, and TRIP strain accumulation, predicted by the model are in good agreement with the experiment data. More specifically, the NiTi SMA accumulating about 11% TRIP strain after the 100 thermal training cycle is predicted. Additionally, by introducing the internal stress into the model formulation, the predicted NiTi SMA load-free TWSME curve also correlates well with the experimental one. In the case of NiTIHf, it can be seen that the high-temperature SMA material system shows a quite different actuation response compared to that of NiTi. Specifically, the phase transformation temperatures are much higher, but much less TRIP strain is accumulated in the end. Although the phase transformation characteristics of NiTiHf are quite different compared to NiTi, the simulated results by the proposed model also agree with the experimental data quite well, which demonstrates the excellent fidelity of the model over multiple SMA ma-

terial systems. Moreover, it is shown that the proposed model is enabled to capture the load-free TWSME response for trained SMAs by introducing the internal stress term into the model formulation.

4.7.3 Multiaxial actuation loading case

After the analysis of BVPs under uniaxial stress state, this part analyzes the BVP subjected to non-uniform stress state. As it was mentioned in the introduction, the majority of applications require the functionality of SMA-based components under multiaxial stress state that are originated from curvatures and discontinuities, such as notches and holes coming from installment requirements, it is imperative to understand the SMA cyclic response under such loading conditions. However, the irrecoverable TRIP strains evolves differently in the multiaxial stress state compared to that in the uniaxial one. In order to study the effect of the stress multiaxiality, a plate actuator with a centric hole made from $Ni_{60}Ti_{40}$ (wt.%) is chosen as the BVP subjected to cyclic actuation loading. The geometry of the plate actuator is shown in Figure 4.11, which has 100 mm in the length, 10 mm in the width, and 0.5 mm in the thickness. The centric hole has a diameter of 2 mm. In the experiment, a nominal load of 136 MPa was applied in the longitudinal direction of the plate, thereafter it was subjected to a thermal cycling between 280 K and 400 K for 100 times while the bias load was maintained constant. The TRIP strain in the longitudinal direction was recorded at the end of each thermal cycling by using the DIC technique. In order to test the capability of the proposed model to predict the multiaxial TRIP evolution for SMA-based structural components under non-uniform stress field, the plate actuator simulation is performed wherein the loading conditions are the same as the experiment. The material parameters used in this simulation are listed in table 4.5 which are calibrated from the uniaxial dogbone specimen experiments.

Table 4.3: Material parameters for NiTi SMA under uniaxial cyclic actuation loading.

Type	Parameter	Value	Parameter	Value
Key material parameters 15	E_A	24.15 [GPa]	C_A	15 [MPa/K]
	E_M	24.15 [GPa]	C_M	8 [MPa/K]
	$\nu_A = \nu_M$	0.33	M_s	330 [K]
	$\alpha_A = \alpha_M$	1.0×10^{-5} [K^{-1}]	M_f	300 [K]
	$H_i^{\max}$	4%	A_s	351 [K]
	$H_f^{\max}$	3.17%	A_f	375 [K]
	$H^{\min}$	0%	k_t	0.045
	τ_{crit}	0 [MPa]		
Smooth hardening parameters 4	n_1	0.5	n_3	0.5
	n_2	0.5	n_4	0.5
TRIP parameters 4	σ_b	80 [MPa]	λ_1	0.1
	C_1^p	2.6×10^{-2}		
	C_2^p	0.18		

Table 4.4: Material parameters for NiTiHf SMA under uniaxial cyclic actuation loading.

Type	Parameter	Value	Parameter	Value
Key material parameters 15	E_A	70 [GPa]	C_A	12.5 [MPa/K]
	E_M	70 [GPa]	C_M	11.9 [MPa/K]
	$\nu_A = \nu_M$	0.33	M_s	441 [K]
	$\alpha_A = \alpha_M$	1.0×10^{-5} [K^{-1}]	M_f	430 [K]
	$H_i^{\max}$	3.15%	A_s	460 [K]
	$H_f^{\max}$	3.15%	A_f	466 [K]
	$H^{\min}$	0.7%	k_t	0.007
	τ_{crit}	0 [MPa]		
Smooth hardening parameters 4	n_1	0.06	n_3	0.06
	n_2	0.06	n_4	0.06
TRIP parameters 4	σ_b	35 [MPa]	λ_1	0.1
	C_1^p	5×10^{-4}		
	C_2^p	0.3		

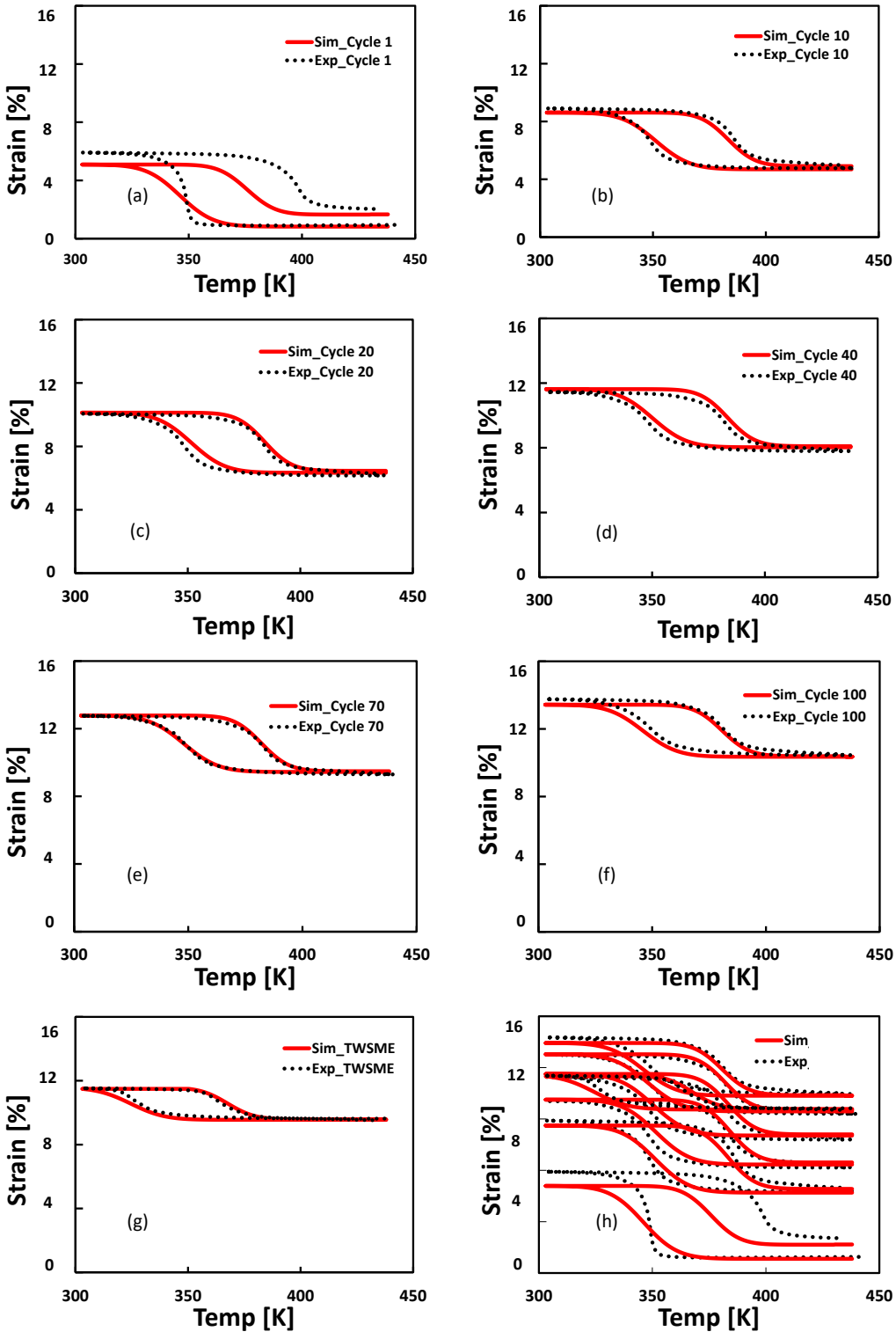

Figure 4.9: Selected thermal training cycling response under constant load 200 MPa and the load-free TWSME response of NiTi SMA. (a) Cycle 1, (b) Cycle 10, (c) Cycle 20, (d) Cycle 40, (e) Cycle 70, (f) Cycle 100, (g) TWSME cycle, (h) Combined.

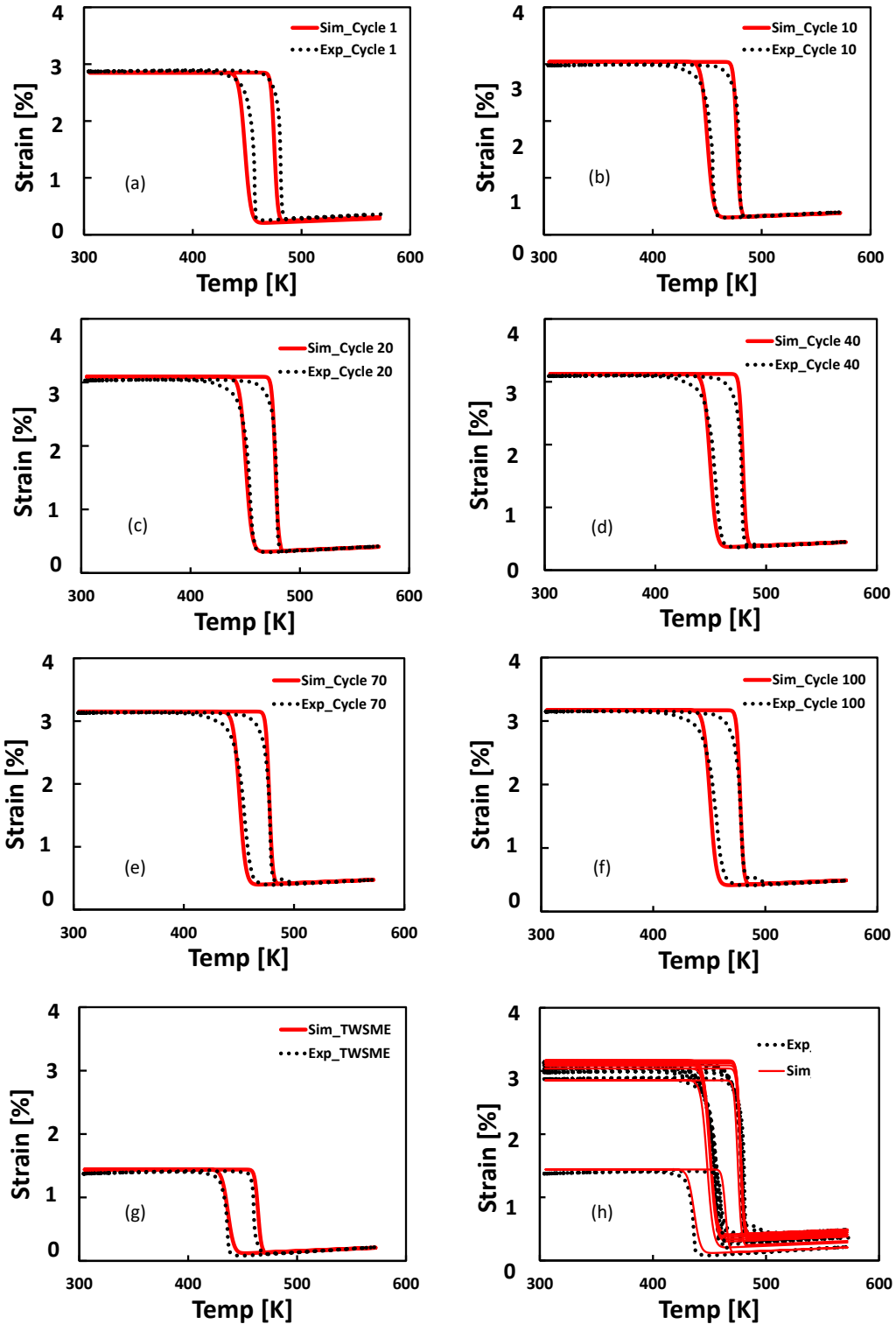

Figure 4.10: Selected thermal training cycling response under constant load 200 MPa and the load-free TWSME response of NiTiHf SMA. (a) Cycle 1, (b) Cycle 10, (c) Cycle 20, (d) Cycle 40, (e) Cycle 70, (f) Cycle 100, (g) TWSME cycle, (h) Combined.

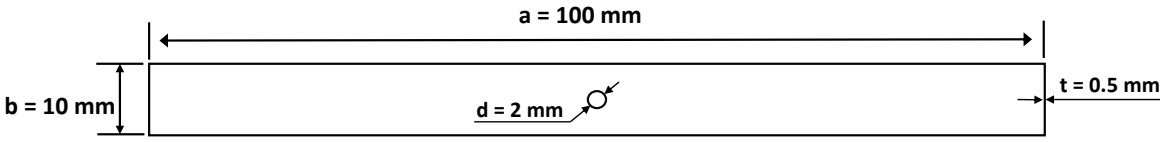

Figure 4.11: The geometry of the $Ni_{60}Ti_{40}$ (wt.%) plate actuator with a centric hole.

Table 4.5: Material parameters used for the $Ni_{60}Ti_{40}$ (wt.%) plate actuator with centric hole under multiaxial stress state.

Type	Parameter	Value	Parameter	Value
Key material parameters 12	E_A	70 [GPa]	C_A	22 [MPa/K]
	E_M	70 [GPa]	C_M	22 [MPa/K]
	$\nu_A = \nu_M$	0.33	M_s	318 [K]
	$\alpha_A = \alpha_M$	1.0×10^{-5} [K^{-1}]	M_f	298 [K]
	$H_i^{\max}$	1.5%	A_s	332 [K]
	$H_f^{\max}$	1.5%	A_f	352 [K]
	$H^{\min}$	0%	k_t	0.01
	τ_{crit}	0 [MPa]		
Smooth hardening parameters 4	n_1	0.5	n_3	0.5
	n_2	0.5	n_4	0.5
TRIP parameters 4	σ_b	0 [MPa]	λ_1	N/A
	C_1^p	5.73×10^{-3}		
	C_2^p	1.972		

As it can be seen from Figure 4.12(a) showing the principal stress contour, an non-uniform stress field is caused in the plate actuator due to the presence of the discontinuity hole, a larger stress field around 400 MPa is present as the stress concentrated part while a much smaller stress field is shown as the less stress concentrated region. As a result of this stress concentration, the phase transformation of the plate actuator is largely redistributed.

As it is shown Figure 4.12 (b), the stress concentrated part starts the phase transformation earlier while the less stressed part is later initiated. Refer to Figure 4.13 for the TRIP strain evolution results, the experimental DIC result is indicated in the bottom row while the prediction results by the proposed model is listed in the upper row. The experimental results show that the multiaxial stress state has a significant effect on the TRIP strain accumulation from cycle to cycle. Specifically, the TRIP strain accumulates much faster in the stress concentrated part than the less stress concentrated part. In cycle 10, There is around 0.17% TRIP strain accumulated in the stress concentration part while the rest of the plate actuator is much less than 0.15%. In cycle 100, there is 0.32% TRIP strain accumulated in the stress concentrated region while the less stress concentrated part is stil well beyond 0.15%, the other plate part under uniform stress field accumulates TRIP strain around 0.25%. The observation on these results can be explained by the following. Based on the stress-dependent transformation strain function H^{cur} in equation 4.19, a larger stress state always generates a greater transformation strain value unless the stress is beyond the saturation point, which means the stress concentrated part can induce more oriented martensitic variants than the less stress concentrated region. Assuming only oriented phase transformation contributes to the generation of TRIP, it is conceivable that stress concentrated region tends to create more TRIP strain compared to the rest part of the plate. Although this phenomenon looks very complex, it can be seen from the simulation results that not only the overall multiaxiality of TRIP generation is captured, but also the TRIP strain magnitude for the whole plate actuator is well predicted by the proposed model. By using the newly proposed multiaxial evolution law for TRIP strain, the proposed model is demonstrated to have the capability to capture the effect of stress multiaxiality on the TRIP strain generation.

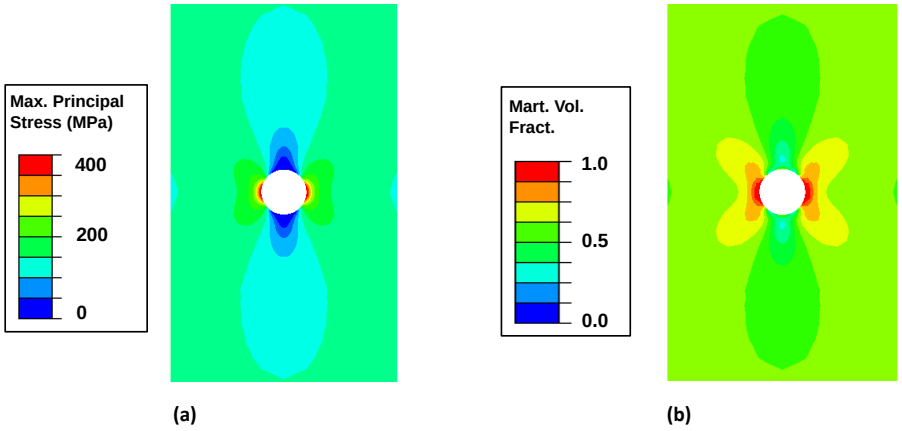

Figure 4.12: Stress and martensitic volume fraction distribution contour for the $Ni_{60}Ti_{40}$ (wt.%) plate actuator with a centric hole predicted by the proposed model. (a) Maximum principal stress contour, (b) martensitic volume fraction contour.

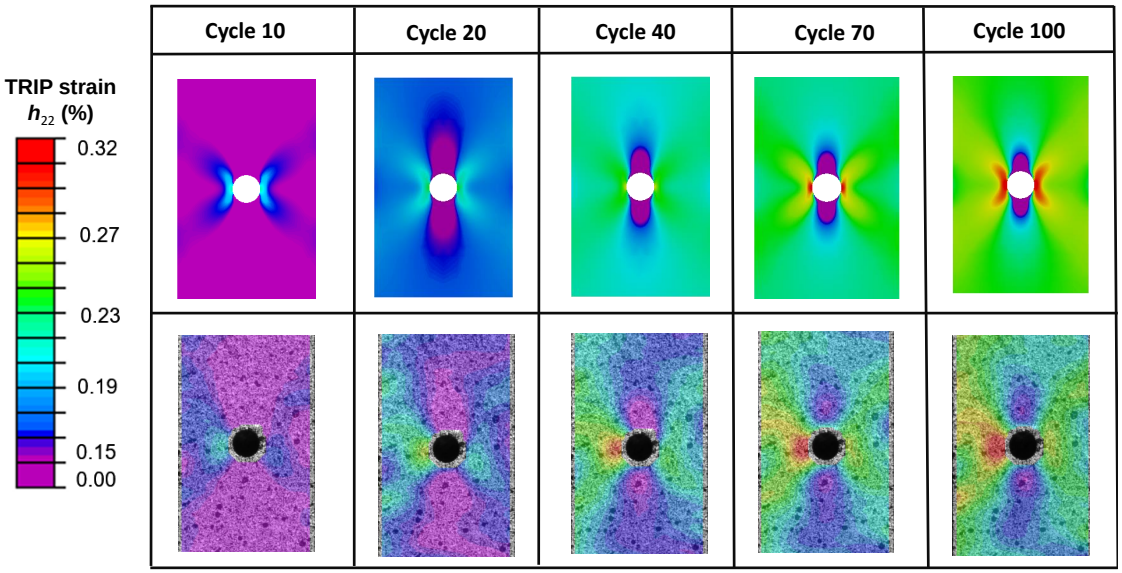

Figure 4.13: TRIP strain evolution contour for the $Ni_{60}Ti_{40}$ (wt.%) plate actuator with a centric hole experiencing a stress concentration subjected to cyclic thermomehcanical loading. The first row is simulation results by the proposed model while the second row is experimental DIC result.

4.8 Conclusion

By using the general thermodynamic framework for dissipative material, a three-dimensional finite strain constitutive model for SMAs considering multiaxial TRIP evolution as well as TWSME due to the introduction of an oriented internal stress field after training is presented in current work. This model is developed based on the early work by [47], and its large deformation formulation [121], as well as its early extensions considering TRIP [9, 50]. By virtue of the martensitic volume fraction, transformation strain, internal stress, and TRIP strain tensors used as internal state variables, the model is enabled to capture the following important characteristics of SMAs: (1) The model formulated based on a finite deformation theory is inherently able to capture the large strains and rotations exhibited by SMAs under cyclic thermomechanical loading. (2) Through the introduction of internal stress tensor accumulated with respect to loading cycles, the model is capable of predicting the TWSME at the load-free condition due to the generation of an oriented internal stress field after training procedure. (3) By proposing a multiaxial TRIP strain evolution law, the model considered the effect of multiaxial stress state on the TRIP strain evolution when SMAs experience a non-uniform stress field. A detailed implementation procedure of the proposed model is presented through a user-defined material subroutine within a numerical environment allowing for solving complex BVPs. Comprehensive instruction on calibrating the material parameters, as well as the derivation of consistent tangent stiffness and thermal matrices are also provided. Simulation results in uniaxial cases predicted by the proposed model showed a very close agreement with experimental results validating the capability of the model to capture the TWSME material response. The predicted multiaxial TRIP strain results of an SMA plate with centric hole experiencing stress concentrations correlated well with the observed experimental DIC results, which demonstrates the ability of the model considering the effect of stress

multiaxiality on TRIP strain evolution. The fidelity of the model shown by results comparison between predictions and experimental results demonstrates the proposed model and its implementation schemes can be used as an efficient design and analysis tool for the future applications of SMA-based functional components.

5. SUMMARY AND PROPOSED FUTURE WORK

5.1 Summary and conclusions

Many engineering applications require SMA-based functional components experiencing large deformations subjected to cyclic thermomechanical loading. The majority of available constitutive models for SMAs are developed based on small deformation theory despite the fact that SMAs can reversibly deform to a relatively large strain regime up to 8% (within the finite strain regime). Besides, repeated phase transformations during cyclic loading cause permanent deformations as a result of the TRIP generated at an effective stress level much lower than the material plastic yielding point. Moreover, realistic applications also require the functionality of SMA-based actuators under multiaxial stress state originated from geometry complexities or installment required discontinuities, such as notches and holes, in which the non-uniform stress state has a significant impact on the TRIP strain generation. In order to address these modeling challenges to facilitate a reliable and efficient design for SMA-based actuators, the finite strain constitutive model for SMAs in the framework of large deformations is required to provide an accurate prediction on the material response considering multiaxial TRIP evolution. To that end, a three-dimensional finite strain constitutive model is proposed for polycrystalline SMAs under large deformation as a starting step in this dissertation. Second, based on the model developed in the first step, a three-dimensional finite strain constitutive model for SMAs incorporating multiaxial TRIP strain evolution and the TWSME is proposed. A detailed implementation of the proposed models is presented through user-defined material subroutines within a numerical environment for solving different bound value problems. The predicted cyclic thermomechanical responses for a wide range of SMA material systems under both uniaxial and multiaxial loading conditions are compared against experimental

results to validate the modeling capabilities.

5.1.1 Finite strain constitutive modeling for SMAs

In order to account for the large deformations exhibited by SMA-based functional components, the first contribution of this work is the proposition of the three-dimensional finite strain constitutive modeling of martensitic transformation for polycrystalline SMAs. The model is developed based on the early classic SMA model proposed by Lagoudas and coworkers for small deformation analysis. Three important characteristics commonly shown in SMA responses are considered, i.e., 1) the smooth transition during the phase transformation, 2) the stress-dependent transformation strain to account for the coexistence of oriented/self-accommodated martensitic variants, and 3) a stress-dependent critical driving force to consider the effect of applied stress levels on the size of the hysteresis loop. The proposed model is formulated based on the finite deformation framework that utilizes logarithmic strain and rate such that it not only accounts for the large strains and rotations but also resolves the residual stress errors that are caused by using other non-integrable objective rates. The proposed model is able to predict the stress-induced and thermally induced phase transformations in SMAs under general three-dimensional thermomechanical loading. In particular, it was shown in the example of an SMA bar that the proposed model accounts for the geometry nonlinearity induced by large strains so that it corrects the spurious material softening in the results from its infinitesimal counterpart. In the numerical examples of an SMA beam and an SMA torque tube, it was demonstrated that the proposed model captures the large rotations that SMA-based components may undertake. By comparing the predicted cyclic response to the results obtained through the Abaqus nonlinear solver, the proposed model demonstrated that it can effectively resolve the residual stress errors. The numerical analysis of a 3-D solid flexible structure experiencing local, non-proportional stress and strain evolution shows that the proposed

model can be used as a simulation tool for the analysis of complex SMA-based structures. The detailed formulation of the proposed model and its implementation procedures laid a solid foundation for the further extension of the model to incorporate TRIP and damage evolution experienced by SMAs under cyclic loading.

5.1.2 Modeling of multiaxial TRIP evolution and TWSME

The second major contribution of this work is the formulation of a three-dimensional finite strain constitutive model for SMAs considering multiaxial TRIP evolution as well as the TWSME after stress or thermally training procedure. By virtue of the martensitic volume fraction, transformation strain, internal stress, and TRIP strain tensors used as internal state variables, along with the general thermodynamic framework for dissipative material, the proposed model is enabled to capture the following important characteristics shown by the material response of SMAs. First, the model formulated based on a finite deformation theory is inherently able to capture the large strains and rotations exhibited by SMAs under cyclic thermomechanical loading. Second, through the introduction of internal stress tensor accumulated with respect to loading cycles, the model is capable of predicting the TWSME at the load-free condition due to the generation of an oriented internal stress field after training procedure. Finally, by proposing a multiaxial TRIP strain evolution law, the model considered the effect of multiaxial stress state on the TRIP strain evolution when SMAs experience a non-uniform stress field. Numerical simulation results in the case of uniaxial cases showed a good agreement with experimental results which validates the capability of the model to capture the TRIP generation and TWSME. The predicted multiaxial TRIP strain results of an SMA plate with centric hole experiencing stress concentrations correlated well with the observed experimental DIC results, which demonstrates the ability of the model considering the effect of stress multiaxiality on TRIP strain evolution. The fidelity of the model shown by results com-

parison between predictions and experimental results demonstrates the proposed model and its implementation schemes can be used as an efficient design and analysis tool for the future applications of SMA-based functional components.

5.2 Proposed future works

Based on the proposed models and its implementation schemes presented in this dissertation, the following pertaining research areas can be further explored as potential future works.

- The evolving cyclic thermomechanical response of an SMA representative volume element (RVE) considering nano-precipitates can be obtained by taking advantage of the proposed model. It has been experimentally demonstrated that an appropriate aging procedure on the as-received SMAs can significantly reduce the amount of TRIP strain generated during cyclic thermomechanical loading. Such heat treatment leads to the formation of nano-precipitates, serving as elastically deformed second-phase particles, inside SMAs when the matrix material undergoing the repeated phase transformations. From a computational micromechanics point of view, the effects of these nano-precipitates on the generation of plastic strain have rarely been explored. Thus, the first advancement can aim at creating a finite element RVE model along with the proposed modeling accounting for TRIP, to provide a fundamental understanding of the interaction between the presence of precipitates and the generation of TRIP strain for aged SMAs.

- Incorporating the accumulation of damage along with the TRIP generation through a unified modeling framework for the prediction of the cyclic thermomechanical response of SMAs is another potential critical advancement for this work. The micro-tomography results computed based on X-ray images have indicated that internal damage evolves in a quite unique manner to SMAs. Specifically, internal damage

is observed to nucleate drastically during initial actuation cycling, followed by a stabilized growth rate and then heads into an exponentially increasing manner till the end [77]. This trend is strongly correlated with the manner of how the TRIP strain accumulates. Due to the intrinsic nature of the interaction between TRIP and damage evolution, it is important to couple these two features via a unified modeling framework, therefore to better understand and analyze the cyclic response, to provide a fatigue and safety design guidance for SMA-based actuators.

- Tension-compression asymmetry should also be incorporated into the unified modeling framework towards designing real actuators that are subjected to non-uniform, multiaxial, tensile-compressive loading. Experimental results for SMA-based beam components subjected to cyclic actuation loading show that there is a significant tension-compression asymmetry exhibited in the tension side of the beam compared to the compression counterpart. Furthermore, the results also show that there is a strain neutral axis (where the strain value is zero) shift due to the phase transformation asymmetry, and such shift continues to grow in the actuation cycles as a consequence of the accumulation of TRIP strain. Therefore, constitutive modeling for SMAs considering TRIP as well as the asymmetric phase transformation characteristics is needed in order to provide an accurate prediction for SMA-based actuators subjected to non-uniform stress state during cyclic deformations.

REFERENCES

[1] Abaqus. 6.14 documentation. *Dassault Systemes Simulia Corporation*, 651, 2014.

[2] J. Arghavani, F. Auricchio, and R. Naghdabadi. A finite strain kinematic hardening constitutive model based on hencky strain: general framework, solution algorithm and application to shape memory alloys. *International Journal of Plasticity*, 27(6):940–961, 2011.

[3] K. Atli, I. Karaman, R. Noebe, G. Bigelow, and D. Gaydosh. Work production using the two-way shape memory effect in niti and a ni-rich nitihf high-temperature shape memory alloy. *Smart Materials and Structures*, 24(12):125023, 2015.

[4] F. Auricchio, A. Reali, and U. Stefanelli. A three-dimensional model describing stress-induced solid phase transformation with permanent inelasticity. *International Journal of plasticity*, 23(2):207–226, 2007.

[5] F. Auricchio and R. L. Taylor. Shape-memory alloys: modelling and numerical simulations of the finite-strain superelastic behavior. *Computer methods in applied mechanics and engineering*, 143(1):175–194, 1997.

[6] N. Barrera, P. Biscari, and M. F. Urbano. Macroscopic modeling of functional fatigue in shape memory alloys. *European Journal of Mechanics-A/Solids*, 45:101–109, 2014.

[7] V. Birman. Review of mechanics of shape memory alloy structures. *Applied Mechanics Reviews*, 50(11):629–645, 1997.

[8] Z. Bo and D. C. Lagoudas. Thermomechanical modeling of polycrystalline smas under cyclic loading, part i: theoretical derivations. *International Journal of Engineering Science*, 37(9):1089–1140, 1999.

[9] Z. Bo and D. C. Lagoudas. Thermomechanical modeling of polycrystalline smas

under cyclic loading, part iii: Evolution of plastic strains and two-way shape memory effect. *International Journal of Engineering Science*, 37(9):1175–1203, 1999.

[10] J. G. Boyd and D. C. Lagoudas. A thermodynamical constitutive model for shape memory materials. part i. the monolithic shape memory alloy. *International Journal of Plasticity*, 12(6):805–842, 1996.

[11] L. Brinson and R. Lammering. Finite element analysis of the behavior of shape memory alloys and their applications. *International Journal of Solids and Structures*, 30(23):3261–3280, 1993.

[12] L. C. Brinson. One-dimensional constitutive behavior of shape memory alloys: thermomechanical derivation with non-constant material functions and redefined martensite internal variable. *Journal of intelligent material systems and structures*, 4(2):229–242, 1993.

[13] O. Bruhns, H. Xiao, and A. Meyers. Self-consistent eulerian rate type elasto-plasticity models based upon the logarithmic stress rate. *International Journal of Plasticity*, 15(5):479–520, 1999.

[14] O. Bruhns, H. Xiao, and A. Meyers. Large simple shear and torsion problems in kinematic hardening elasto-plasticity with logarithmic rate. *International journal of solids and structures*, 38(48):8701–8722, 2001.

[15] O. Bruhns, H. Xiao, and A. Meyers. A self-consistent eulerian rate type model for finite deformation elastoplasticity with isotropic damage. *International Journal of Solids and Structures*, 38(4):657–683, 2001.

[16] F. Calkins and J. Mabe. Flight test of a shape memory alloy actuated adaptive trailing edge flap. In *ASME 2016 Conference on Smart Materials, Adaptive Structures and Intelligent Systems*, pages V001T04A007–V001T04A007. American Society of Mechanical Engineers, 2016.

[17] Y. Chemisky, A. Duval, E. Patoor, and T. B. Zineb. Constitutive model for shape

memory alloys including phase transformation, martensitic reorientation and twins accommodation. *Mechanics of Materials*, 43(7):361–376, 2011.

[18] L.-Q. Chen. Phase-field models for microstructure evolution. *Annual review of materials research*, 32(1):113–140, 2002.

[19] C. Cisse, W. Zaki, and T. B. Zineb. A review of constitutive models and modeling techniques for shape memory alloys. *International Journal of Plasticity*, 76:244–284, 2016.

[20] B. D. Coleman and M. E. Gurtin. Thermodynamics with internal state variables. *The Journal of Chemical Physics*, 47(2):597–613, 1967.

[21] B. D. Coleman and W. Noll. The thermodynamics of elastic materials with heat conduction and viscosity. In *The Foundations of Mechanics and Thermodynamics*, pages 145–156. Springer, 1974.

[22] A. Damanpack, M. Bodaghi, and W. Liao. A finite-strain constitutive model for anisotropic shape memory alloys. *Mechanics of Materials*, 112:129–142, 2017.

[23] E. A. de Souza Neto, D. Peric, and D. R. Owen. *Computational methods for plasticity: theory and applications*. John Wiley & Sons, 2011.

[24] J. K. Dienes. On the analysis of rotation and stress rate in deforming bodies. *Acta mechanica*, 32(4):217–232, 1979.

[25] V. Evangelista, S. Marfia, and E. Sacco. A 3d sma constitutive model in the framework of finite strain. *International Journal for Numerical Methods in Engineering*, 81(6):761–785, 2010.

[26] M. E. Gurtin. *An introduction to continuum mechanics*, volume 158. Academic press, 1982.

[27] K. Hackl and R. Heinen. A micromechanical model for pretextured polycrystalline shape-memory alloys including elastic anisotropy. *Continuum Mechanics and Thermodynamics*, 19(8):499–510, 2008.

[28] B. Haghgouyan, C. Hayrettin, T. Baxevanis, I. Karaman, and D. C. Lagoudas. Fracture toughness of niti–towards establishing standard test methods for phase transforming materials. *Acta Materialia*, 162:226–238, 2019.

[29] B. Haghgouyan, N. Shafaghi, C. C. Aydıner, and G. Anlas. Experimental and computational investigation of the effect of phase transformation on fracture parameters of an sma. *Smart Materials and Structures*, 25(7):075010, 2016.

[30] D. Hartl and D. Lagoudas. Constitutive modeling and structural analysis considering simultaneous phase transformation and plastic yield in shape memory alloys. *Smart Materials and Structures*, 18(10):104017, 2009.

[31] D. Hartl, J. Mooney, D. Lagoudas, F. Calkins, and J. Mabe. Use of a ni60ti shape memory alloy for active jet engine chevron application: Ii. experimentally validated numerical analysis. *Smart Materials and Structures*, 19(1):015021, 2009.

[32] D. J. Hartl, G. Chatzigeorgiou, and D. C. Lagoudas. Three-dimensional modeling and numerical analysis of rate-dependent irrecoverable deformation in shape memory alloys. *International Journal of Plasticity*, 26(10):1485–1507, 2010.

[33] D. J. Hartl and D. C. Lagoudas. Aerospace applications of shape memory alloys. *Proceedings of the Institution of Mechanical Engineers, Part G: Journal of Aerospace Engineering*, 221(4):535–552, 2007.

[34] R. Hill. A variational principle of maximum plastic work in classical plasticity. *The Quarterly Journal of Mechanics and Applied Mathematics*, 1(1):18–28, 1948.

[35] R. Hill. Aspects of invariance in solid mechanics. In *Advances in applied mechanics*, volume 18, pages 1–75. Elsevier, 1979.

[36] R. Hill. *The mathematical theory of plasticity*, volume 11. Oxford university press, 1998.

[37] G. A. Holzapfel. Nonlinear solid mechanics: a continuum approach for engineering science. *Meccanica*, 37(4):489–490, 2002.

[38] U. Icardi and L. Ferrero. Preliminary study of an adaptive wing with shape memory alloy torsion actuators. *Materials & Design*, 30(10):4200–4210, 2009.

[39] J. M. Jani, M. Leary, A. Subic, and M. A. Gibson. A review of shape memory alloy research, applications and opportunities. *Materials & Design*, 56:1078–1113, 2014.

[40] J. M. Jani, M. Leary, A. Subic, and M. A. Gibson. A review of shape memory alloy research, applications and opportunities. *Materials & Design*, 56:1078–1113, 2014.

[41] R. Jayendiran, B. Nour, and A. Ruimi. Computational fluid–structure interaction analysis of blood flow on patient-specific reconstructed aortic anatomy and aneurysm treatment with dacron graft. *Journal of Fluids and Structures*, 81:693–711, 2018.

[42] R. Jayendiran, B. Nour, and A. Ruimi. Fluid-structure interaction (fsi) analysis of stent-graft for aortic endovascular aneurysm repair (evar): Material and structural considerations. *Journal of the mechanical behavior of biomedical materials*, 87:95–110, 2018.

[43] D. Jiang and C. M. Landis. A constitutive model for isothermal pseudoelasticity coupled with plasticity. *Shape Memory and Superelasticity*, 2(4):360–370, 2016.

[44] D. Kapoor. Nitinol for medical applications: A brief introduction to the properties and processing of nickel titanium shape memory alloys and their use in stents. *Johnson Matthey Technology Review*, 61(1):66–76, 2017.

[45] A. S. Khan and S. Huang. *Continuum theory of plasticity*. John Wiley & Sons, 1995.

[46] J. N. Kudva. Overview of the darpa smart wing project. *Journal of intelligent material systems and structures*, 15(4):261–267, 2004.

[47] D. Lagoudas, D. Hartl, Y. Chemisky, L. Machado, and P. Popov. Constitutive

model for the numerical analysis of phase transformation in polycrystalline shape memory alloys. *International Journal of Plasticity*, 32:155–183, 2012.

[48] D. C. Lagoudas. *Shape memory alloys: modeling and engineering applications*. Springer Science & Business Media, 2008.

[49] D. C. Lagoudas and Z. Bo. Thermomechanical modeling of polycrystalline smas under cyclic loading, part ii: Material characterization and experimental results for a stable transformation cycle. *International Journal of Engineering Science*, 37(9):1141–1173, 1999.

[50] D. C. Lagoudas and P. B. Entchev. Modeling of transformation-induced plasticity and its effect on the behavior of porous shape memory alloys. part i: constitutive model for fully dense smas. *Mechanics of Materials*, 36(9):865–892, 2004.

[51] W. M. Lai, D. H. Rubin, E. Krempl, and D. Rubin. *Introduction to continuum mechanics*. Butterworth-Heinemann, 2009.

[52] D. S. Lazzara, T. Magee, H. Shen, and J. H. Mabe. Off-design sonic boom performance for low-boom aircraft. In *AIAA Scitech 2019 Forum*, page 0606, 2019.

[53] S. Leclercq and C. Lexcellent. A general macroscopic description of the thermomechanical behavior of shape memory alloys. *Journal of the Mechanics and Physics of Solids*, 44(6):953–980, 1996.

[54] S. Leclercq and C. Lexcellent. A general macroscopic description of the thermomechanical behavior of shape memory alloys. *Journal of the Mechanics and Physics of Solids*, 44(6):953–980, 1996.

[55] S. Leclercq and C. Lexcellent. A general macroscopic description of the thermomechanical behavior of shape memory alloys. *Journal of the Mechanics and Physics of Solids*, 44(6):953–980, 1996.

[56] V. I. Levitas. Thermomechanical theory of martensitic phase transformations in inelastic materials. *International Journal of Solids and Structures*, 35(9):889–940,

1998.

[57] V. I. Levitas and D. L. Preston. Three-dimensional landau theory for multivariant stress-induced martensitic phase transformations. i. austenite martensite. *Physical review B*, 66(13):134206, 2002.

[58] C. Lexcellent. *Shape-memory alloys handbook*. John Wiley & Sons, 2013.

[59] C. Lexcellent, S. Leclercq, B. Gabry, and G. Bourbon. The two way shape memory effect of shape memory alloys: an experimental study and a phenomenological model. *International Journal of Plasticity*, 16(10-11):1155–1168, 2000.

[60] J. T. Lim and D. L. McDowell. Degradation of an ni-ti alloy during cyclic loading. In *Smart Structures and Materials 1994: Smart Materials*, volume 2189, pages 326–341. International Society for Optics and Photonics, 1994.

[61] X. Liu, Y. Wang, D. Yang, and M. Qi. The effect of ageing treatment on shape-setting and superelasticity of a nitinol stent. *Materials Characterization*, 59(4):402–406, 2008.

[62] J. Mabe, J. Brown, and F. Calkins. Flight test of a shape memory alloy actuated adaptive trailing edge flap, part 1. In *Proceedings of SMST 2014 the International Conference on Shape Memory and Superelastic Technologies*, 2014.

[63] T. Machairas, A. Solomou, and D. Saravanos. A morphing chevron actuated by shape memory alloy wires for noise reduction. In *las actas, proceedings, de 3AF/CEAS Conference Greener Aviation: Clean Sky Breakthroughs and Worldwide Status*, 2014.

[64] M. Mamivand, M. A. Zaeem, and H. El Kadiri. A review on phase field modeling of martensitic phase transformation. *Computational Materials Science*, 77:304–311, 2013.

[65] J. M. Medical. An overview of nitinol: superelastic and shape memory. *Medical Design Briefs*, 2015.

[66] A. Meyers, H. Xiao, and O. Bruhns. Elastic stress ratcheting and corotational stress rates. *Tech. Mech*, 23:92–102, 2003.

[67] A. Meyers, H. Xiao, and O. Bruhns. Choice of objective rate in single parameter hypoelastic deformation cycles. *Computers & structures*, 84(17):1134–1140, 2006.

[68] C. MIEHE. Exponential map algorithm for stress updates in anisotropic multiplicative elastoplasticity for single crystals. *International Journal for Numerical Methods in Engineering*, 39(19):3367–3390, 1996.

[69] C. Müller and O. Bruhns. A thermodynamic finite-strain model for pseudoelastic shape memory alloys. *International Journal of Plasticity*, 22(9):1658–1682, 2006.

[70] F. Niccoli, C. Garion, C. Maletta, E. Sgambitterra, F. Furgiuele, and P. Chiggiato. Beam-pipe coupling in particle accelerators by shape memory alloy rings. *Materials & Design*, 114:603–611, 2017.

[71] R. W. Ogden. *Non-linear elastic deformations*. Courier Corporation, 1997.

[72] K. Otsuka and C. M. Wayman. *Shape memory materials*. Cambridge university press, 1999.

[73] E. Patoor, A. Eberhardt, and M. Berveiller. Micromechanical modelling of superelasticity in shape memory alloys. *Le Journal de Physique IV*, 6(C1):C1–277, 1996.

[74] E. Patoor, D. C. Lagoudas, P. B. Entchev, L. C. Brinson, and X. Gao. Shape memory alloys, part i: General properties and modeling of single crystals. *Mechanics of materials*, 38(5):391–429, 2006.

[75] E. Peraza-Hernandez, D. Hartl, E. Galvan, and R. Malak. Design and optimization of a shape memory alloy-based self-folding sheet. *Journal of Mechanical Design*, 135(11):111007, 2013.

[76] E. A. Peraza-Hernandez, D. J. Hartl, R. J. Malak Jr, and D. C. Lagoudas. Origami-

inspired active structures: a synthesis and review. *Smart Materials and Structures*, 23(9):094001, 2014.

[77] F. R. Phillips, R. W. Wheeler, A. B. Geltmacher, and D. C. Lagoudas. Evolution of internal damage during actuation fatigue in shape memory alloys. *International Journal of Fatigue*, 124:315–327, 2019.

[78] M. Qidwai and D. Lagoudas. Numerical implementation of a shape memory alloy thermomechanical constitutive model using return mapping algorithms. *International Journal for Numerical Methods in Engineering*, 47(6):1123–1168, 2000.

[79] M. Qidwai and D. Lagoudas. On thermomechanics and transformation surfaces of polycrystalline niti shape memory alloy material. *International Journal of Plasticity*, 16(10):1309–1343, 2000.

[80] B. Raniecki and C. Lexcellent. Thermodynamics of isotropic pseudoelasticity in shape memory alloys. *European Journal of Mechanics-A/Solids*, 17(2):185–205, 1998.

[81] B. Raniecki, C. Lexcellent, and K. Tanaka. Thermodynamic models of pseudoelastic behaviour of shape memory alloys. *Archiv of Mechanics, Archiwum Mechaniki Stosowanej*, 44:261–284, 1992.

[82] S. Reese and D. Christ. Finite deformation pseudo-elasticity of shape memory alloys–constitutive modelling and finite element implementation. *International Journal of Plasticity*, 24(3):455–482, 2008.

[83] X. Ren and K. Otsuka. Universal symmetry property of point defects in crystals. *Physical Review Letters*, 85(5):1016, 2000.

[84] P. Rodriguez and G. Guénin. Stability of the two way memory effect during thermal cycling of a high ms temperature cu-al-ni alloy. In *Materials Science Forum*, volume 56, pages 541–546. Trans Tech Publ, 1990.

[85] L. Saint-Sulpice, S. A. Chirani, and S. Calloch. A 3d super-elastic model for

shape memory alloys taking into account progressive strain under cyclic loadings. *Mechanics of materials*, 41(1):12–26, 2009.

[86] R. Saunders, D. Hartl, J. Herrington, L. Hodge, and J. Mabe. Optimization of a composite morphing wing with shape memory alloy torsional actuators. In *ASME 2014 Conference on Smart Materials, Adaptive Structures and Intelligent Systems*, pages V002T02A014–V002T02A014. American Society of Mechanical Engineers, 2014.

[87] P. Sedlak, M. Frost, B. Benešová, T. B. Zineb, and P. Šittner. Thermomechanical model for niti-based shape memory alloys including r-phase and material anisotropy under multi-axial loadings. *International Journal of Plasticity*, 39:132–151, 2012.

[88] B. Seth. Generalized strain measure with applications to physical problems. Technical report, WISCONSIN UNIV-MADISON MATHEMATICS RESEARCH CENTER, 1961.

[89] J. A. Shaw. Simulations of localized thermo-mechanical behavior in a niti shape memory alloy. *International Journal of Plasticity*, 16(5):541–562, 2000.

[90] J. C. Simo and T. J. Hughes. *Computational inelasticity*, volume 7. Springer Science & Business Media, 2006.

[91] P. Šittner, P. Sedlák, H. Seiner, P. Sedmak, J. Pilch, R. Delville, L. Heller, and L. Kadeřávek. On the coupling between martensitic transformation and plasticity in niti: Experiments and continuum based modelling. *Progress in Materials Science*, 2018.

[92] G. Song, D. Patil, C. Kocurek, and J. Bartos. Applications of shape memory alloys in offshore oil and gas industry: a review. In *Earth and Space 2010: Engineering, Science, Construction, and Operations in Challenging Environments*, pages 1551–1567. 2010.

[93] I. Steinbach and M. Apel. Multi phase field model for solid state transformation with elastic strain. *Physica D: Nonlinear Phenomena*, 217(2):153–160, 2006.

[94] I. Steinbach and F. Pezzolla. A generalized field method for multiphase transformations using interface fields. *Physica D: Nonlinear Phenomena*, 134(4):385–393, 1999.

[95] D. Stoeckel, A. Pelton, and T. Duerig. Self-expanding nitinol stents: material and design considerations. *European radiology*, 14(2):292–301, 2004.

[96] B. Strnadel and S. Miyazaki. Modelling residual strains during cycling of ti–ni and ti–ni–cu shape memory alloys in a pseudoelastic range of behaviour conditions. *Strain*, 47:e457–e466, 2011.

[97] B. Strnadel, S. Ohashi, H. Ohtsuka, T. Ishihara, and S. Miyazaki. Cyclic stress-strain characteristics of ti-ni and ti-ni-cu shape memory alloys. *Materials Science and Engineering: A*, 202(1-2):148–156, 1995.

[98] B. Strnadel, S. Ohashi, H. Ohtsuka, T. Ishihara, and S. Miyazaki. Effect of mechanical cycling on the pseudoelasticity characteristics of ti-ni and ti-ni-cu alloys. *Materials Science and Engineering: A*, 203(1-2):187–196, 1995.

[99] S. Stupkiewicz and H. Petryk. A robust model of pseudoelasticity in shape memory alloys. *International Journal for Numerical Methods in Engineering*, 93(7):747–769, 2013.

[100] M. Tabesh, J. Boyd, K. C. Atli, I. Karaman, and D. Lagoudas. Design, fabrication, and testing of a multiple-actuation shape memory alloy pipe coupler. *Journal of Intelligent Material Systems and Structures*, 29(6):1165–1182, 2018.

[101] K. Tanaka, F. Nishimura, T. Hayashi, H. Tobushi, and C. Lexcellent. Phenomenological analysis on subloops and cyclic behavior in shape memory alloys under mechanical and/or thermal loads. *Mechanics of Materials*, 19(4):281–292, 1995.

[102] J. P. Teeriaho. An extension of a shape memory alloy model for large deformations

based on an exactly integrable eulerian rate formulation with changing elastic properties. *International Journal of Plasticity*, 43:153–176, 2013.

[103] P. Thamburaja and L. Anand. Polycrystalline shape-memory materials: effect of crystallographic texture. *Journal of the Mechanics and Physics of Solids*, 49(4):709–737, 2001.

[104] C. Truesdell and W. Noll. The non-linear field theories of mechanics. In *The non-linear field theories of mechanics*, pages 1–579. Springer, 2004.

[105] J. Wang, Z. Moumni, W. Zhang, Y. Xu, and W. Zaki. A 3d finite-strain-based constitutive model for shape memory alloys accounting for thermomechanical coupling and martensite reorientation. *Smart Materials and Structures*, 26(6):065006, 2017.

[106] J. Wang, Z. Moumni, W. Zhang, and W. Zaki. A thermomechanically coupled finite deformation constitutive model for shape memory alloys based on hencky strain. *International Journal of Engineering Science*, 117:51–77, 2017.

[107] X. Wang, B. Xu, and Z. Yue. Micromechanical modelling of the effect of plastic deformation on the mechanical behaviour in pseudoelastic shape memory alloys. *International Journal of Plasticity*, 24(8):1307–1332, 2008.

[108] R. Wheeler, R. Saunders, K. Pickett, C. Eckert, H. Stroud, T. Fink, K. Gakhar, J. Boyd, and D. Lagoudas. Design of a reconfigurable sma-based solar array deployment mechanism. In *ASME 2015 Conference on Smart Materials, Adaptive Structures and Intelligent Systems*, pages V001T02A010–V001T02A010. American Society of Mechanical Engineers, 2015.

[109] R. W. Wheeler. *Actuation Fatigue Characterization Methods and Lifetime Predictions of Shape Memory Alloy Actuators*. PhD thesis, 2017.

[110] R. W. Wheeler, D. J. Hartl, Y. Chemisky, and D. C. Lagoudas. Characterization and modeling of thermo-mechanical fatigue in equiatomic niti actuators. In

ASME 2014 Conference on Smart Materials, Adaptive Structures and Intelligent Systems, pages V002T02A009–V002T02A009. American Society of Mechanical Engineers, 2014.

[111] H. Xiao. An explicit, straightforward approach to modeling sma pseudoelastic hysteresis. *International Journal of Plasticity*, 53:228–240, 2014.

[112] H. Xiao, I. O. Bruhns, and I. A. Meyers. Logarithmic strain, logarithmic spin and logarithmic rate. *Acta Mechanica*, 124(1-4):89–105, 1997.

[113] H. Xiao, O. Bruhns, and A. Meyers. Hypo-elasticity model based upon the logarithmic stress rate. *Journal of Elasticity*, 47(1):51–68, 1997.

[114] H. Xiao, O. Bruhns, and A. Meyers. Objective corotational rates and unified work-conjugacy relation between eulerian and lagrangean strain and stress measures. *Archives of Mechanics*, 50(6):1015–1045, 1998.

[115] H. Xiao, O. Bruhns, and A. Meyers. Existence and uniqueness of the integrable-exactly hypoelastic equation and its significance to finite inelasticity. *Acta Mechanica*, 138(1):31–50, 1999.

[116] H. Xiao, O. Bruhns, and A. Meyers. Elastoplasticity beyond small deformations. *Acta Mechanica*, 182(1-2):31–111, 2006.

[117] L. Xu, T. Baxevanis, and D. Lagoudas. A finite strain constitutive model considering transformation induced plasticity for shape memory alloys under cyclic loading. In *8th ECCOMAS Thematic Conference on Smart Structures and Materials*, pages 1645–1477, 2017.

[118] L. Xu, T. Baxevanis, and D. Lagoudas. A three-dimensional constitutive model for polycrystalline shape memory alloys under large strains combined with large rotations. In *ASME 2018 Conference on Smart Materials, Adaptive Structures and Intelligent Systems*. American Society of Mechanical Engineers Digital Collection, 2018.

[119] L. Xu, T. Baxevanis, and D. Lagoudas. A three-dimensional constitutive model for polycrystalline shape memory alloys under large strains combined with large rotations. In *ASME 2018 Conference on Smart Materials, Adaptive Structures and Intelligent Systems*, pages V002T02A007–V002T02A007. American Society of Mechanical Engineers, 2018.

[120] L. Xu, T. Baxevanis, and D. C. Lagoudas. A finite strain constitutive model for martensitic transformation in shape memory alloys based on logarithmic strain. In *25th AIAA/AHS Adaptive Structures Conference*, page 0731, 2017.

[121] L. Xu, T. Baxevanis, and D. C. Lagoudas. A three-dimensional constitutive model for the martensitic transformation in polycrystalline shape memory alloys under large deformation. *Smart Materials and Structures*, 28(7):074004, jun 2019.

[122] L. Xu, T. Baxevanis, and D. C. Lagoudas. A three-dimensional constitutive modeling for shape memory alloys considering two-way shape memory effect and transformation-induced plasticity. In *AIAA Scitech 2019 Forum*, page 1195, 2019.

[123] C. Yu, G. Kang, Q. Kan, and D. Song. A micromechanical constitutive model based on crystal plasticity for thermo-mechanical cyclic deformation of niti shape memory alloys. *International Journal of Plasticity*, 44:161–191, 2013.

[124] C. Yu, G. Kang, Q. Kan, and Y. Zhu. Rate-dependent cyclic deformation of super-elastic niti shape memory alloy: thermo-mechanical coupled and physical mechanism-based constitutive model. *International Journal of Plasticity*, 72:60–90, 2015.

[125] W. Zaki and Z. Moumni. A three-dimensional model of the thermomechanical behavior of shape memory alloys. *Journal of the Mechanics and Physics of Solids*, 55(11):2455–2490, 2007.

[126] Y. Zhong and T. Zhu. Phase-field modeling of martensitic microstructure in niti shape memory alloys. *Acta Materialia*, 75:337–347, 2014.

[127] Y. Zhu, G. Kang, Q. Kan, and O. T. Bruhns. Logarithmic stress rate based constitutive model for cyclic loading in finite plasticity. *International Journal of Plasticity*, 54:34–55, 2014.

[128] Y. Zhu, G. Kang, Q. Kan, O. T. Bruhns, and Y. Liu. Thermo-mechanically coupled cyclic elasto-viscoplastic constitutive model of metals: theory and application. *International Journal of Plasticity*, 79:111–152, 2016.

[129] A. Ziolkowski. Three-dimensional phenomenological thermodynamic model of pseudoelasticity of shape memory alloys at finite strains. *Continuum Mechanics and Thermodynamics*, 19(6):379–398, 2007.

APPENDIX A

CALCULATION OF ORTHOGONAL ROTATION MATRIX

A.1 Objective rates and spin tensor

One of the major points to achieve the objective implementation for the rate form constitutive models is to calculate the right rotation matrix. This section presents a detailed calculation procedure for that purpose. Consider $\boldsymbol{\Omega}^*$ to be a second-order anti-symmetric tensor, usually called the spin tensor associated with objective rates, it can define a proper rotation tensor[1] by the following tensorial differential equation,

$$\boldsymbol{\Omega}^* = \dot{\mathbf{R}}^* \, \mathbf{R}^{*T}, \quad \mathbf{R}^*|_{t=0} = \mathbf{I} \tag{A.1}$$

in the above equation, the asterisk symbol $(\cdot)^*$ over the tensor means different rotation tensors for selected objective rates. By using the preceding equation, the following relationship can be obtained for an objective symmetric second-order tensor $\mathbf{A}$,

$$\overline{\mathbf{R}^{*T} \dot{\mathbf{A}} \, \mathbf{R}^*} = \dot{\mathbf{R}}^{*T} \mathbf{A} \, \mathbf{R}^* + \mathbf{R}^{*T} \dot{\mathbf{A}} \, \mathbf{R}^* + \mathbf{R}^{*T} \mathbf{A} \, \dot{\mathbf{R}}^* = \mathbf{R}^{*T} \, \mathring{\mathbf{A}}^* \, \mathbf{R}^* \tag{A.2}$$

where the objective rate of $\mathbf{A}$ is

$$\mathring{\mathbf{A}}^* = \dot{\mathbf{A}} + \mathbf{A}\boldsymbol{\Omega}^* - \boldsymbol{\Omega}^* \mathbf{A} \tag{A.3}$$

Moreover, the rate form equation (A.2) can be reformulated as the following incre-

[1] In many of the published papers by Xiao et al. [116], an orthogonal tensor $\mathbf{Q}$ is more often used. It should be noted the rotation tensor $\mathbf{R}^*$ used here has the following transpose relationship with that orthogonal tensor, $\mathbf{Q} = \mathbf{R}^{*T}$, by using the above relationship equation (A.1) becomes $\dot{\mathbf{Q}} = -\,\mathbf{Q}\,\boldsymbol{\Omega}^*$.

mental form by using the backward integration procedure,

$$(\mathbf{R}^{*T}\mathbf{A}\ \mathbf{R}^{*})_{n+1} - (\mathbf{R}^{*T}\mathbf{A}\ \mathbf{R}^{*})_{n} = (\mathbf{R}^{*T}\ \mathring{\mathbf{A}}^{*}\ \mathbf{R}^{*})_{n+1} \tag{A.4}$$

by rearranging the above equation, the following detailed incremental formulation can be obtained,

$$\mathring{\mathbf{A}}^{*}_{n+1} = \mathbf{A}_{n+1} - (\mathbf{R}^{*}_{n+1}\mathbf{R}^{*T}_{n})\mathbf{A}_{n}\ (\mathbf{R}^{*}{}_{n}\mathbf{R}^{*T}_{n+1}) \tag{A.5}$$

the incremental rotation matrix $\Delta\mathbf{R}_{n+1}$ can thus be obtained as,

$$\Delta\mathbf{R}_{n+1} = \mathbf{R}^{*}_{n+1}\mathbf{R}^{*T}_{n} \tag{A.6}$$

There are many different choices on the objective rates depending on how the spin tensor $\mathbf{\Omega}^{*}$ is defined, a thorough discussion on these objective rates and their associated spin tensor definition can be found from Xiao et al.[112, 114]. One of the most well-known objective rates is Zaremba-Jaumann-Noll rate [24, 104] which is defined as the following equation where the spin tensor is nothing but the vorticity tensor $\mathbf{\Omega}^{*} = \mathbf{W}$,

$$\mathbf{\Omega}^{J} = \mathbf{W} \tag{A.7}$$

Another commonly used objective rate is the Green-Naghdi (or polar) rate where the spin tensor is defined as,

$$\mathbf{\Omega}^{R} = \dot{\mathbf{R}}\mathbf{R}^{T} = \mathbf{W} + \sum_{i\neq j}^{n}\left(\frac{1-\sqrt{\lambda_i/\lambda_j}}{1+\sqrt{\lambda_i/\lambda_j}}\right)\mathbf{b}_i\mathbf{D}\mathbf{b}_j \tag{A.8}$$

the rotation tensor $\mathbf{R}$ in the above equation is the rotation tensor defined in the polar decomposition of the deformation gradient.

In this work, the recently proposed logarithmic rate [112, 113, 114, 115] is the cho-

sen objective rate used in the current formulation for the finite strain constitutive modeling of shape memory alloys, in which the logarithmic spin has the following expression,

$$\boldsymbol{\Omega}^{log} = \mathbf{W} + \mathbf{N}^{log} = \mathbf{W} + \sum_{i \neq j}^{n} \big(\frac{1 + (\lambda_i/\lambda_j)}{1 - (\lambda_i/\lambda_j)} + \frac{2}{\ln(\lambda_i/\lambda_j)}\big)\mathbf{b}_i\mathbf{D}\mathbf{b}_j \tag{A.9}$$

the symbol $\sum_{i\neq j}^{n}$ indicates the summation for $i, j = 1, ..., n$ except for $i = j$. Such summation vanishes in the case of one-dimensional case $n = 1$. $n = 2$ indicates a two-dimensional case, and $n = 3$ means a three-dimensional case. The explicit expression to calculate $\mathbf{N}^{log}$ in the logarithmic spin is the follows,

$$\mathbf{N}^{log} = \begin{cases} \mathbf{0}, & \lambda_1 = \lambda_2 = \lambda_3, \\ v[\mathbf{BD}], & \lambda_1 \neq \lambda_2 = \lambda_3, \\ v_1[\mathbf{BD}] + v_2[\mathbf{B}^2\mathbf{D}] + v_3[\mathbf{B}^2\mathbf{DB}], & \lambda_1 \neq \lambda_2 \neq \lambda_3 \end{cases} \tag{A.10}$$

in the preceding equation, the $[\cdot]$ symbol denotes the following tensorial calculation,

$$[\mathbf{B}^r\mathbf{DB}^s] = \mathbf{B}^r\mathbf{DB}^s - \mathbf{B}^s\mathbf{DB}^r, \qquad r, s = 0, 1, 2 \tag{A.11}$$

also in equation (A.10),

$$v = \frac{1}{\lambda_1 - \lambda_2}\big(\frac{1 + (\lambda_1/\lambda_2)}{1 - (\lambda_1/\lambda_2)} + \frac{2}{\ln(\lambda_1/\lambda_2)}\big) \tag{A.12}$$

and,

$$\begin{cases} v_k = -\frac{1}{\Delta}\sum_{i=1}^{3}(-\lambda_i)^{3-k}\big(\frac{1+z_i}{1-z_i} + \frac{2}{\ln(z_i)}\big), \\ \Delta = (\lambda_1 - \lambda_2)(\lambda_2 - \lambda_3)(\lambda_3 - \lambda_1), \\ z_1 = \lambda_2/\lambda_3,\ z_2 = \lambda_3/\lambda_1,\ z_3 = \lambda_1/\lambda_2 \end{cases} \tag{A.13}$$

A.2 Numerical algorithm to calculate the rotation matrix

In order to get the value of $\mathbf{R}^*$ for each numerical incremental step, a robust and consistent algorithm is needed to solve the tensorial differential equation (A.1). An intuitive approach is to use the finite difference method to discretize the material rate on rotation tensor $\dot{\mathbf{R}}^*$ as $(\mathbf{R}^*_{n+1} - \mathbf{R}^*_{n+1})/\Delta t$. However, such a finite-difference scheme fails to provide accurate solutions because the difference between the two rotation matrix is not orthogonal.

A robust algorithm, called the exponential map scheme [90], is able to transform the anti-symmetric spin tensor $\mathbf{\Omega}$ into the orthogonal matrices via the following equation,

$$\exp(\mathbf{\Omega}) = \sum_{n=0}^{+\infty} \frac{1}{n!}(\mathbf{\Omega})^n \tag{A.14}$$

The following reduced-form can be obtained given $\mathbf{\Omega}$ is anti-symmetric,

$$\exp(\mathbf{\Omega}) = \mathbf{I} + \frac{\sin(||\boldsymbol{\omega}||)}{||\boldsymbol{\omega}||}\mathbf{\Omega} + \frac{1}{2}\Big[\frac{\sin(||\boldsymbol{\omega}/2||)}{||\boldsymbol{\omega}/2||}\Big]^2\mathbf{\Omega}^2 \tag{A.15}$$

in which $||\cdot||$ indicates the norm of the matrix, and $\boldsymbol{\omega}$ is called the spin vector that can be constructed based on $\mathbf{\Omega}$ as follows,

$$\boldsymbol{\omega} = \begin{bmatrix} \omega_1 \\ \omega_2 \\ \omega_3 \end{bmatrix}; \quad \mathbf{\Omega} = \begin{bmatrix} 0 & -\omega_3 & \omega_2 \\ \omega_3 & 0 & -\omega_1 \\ -\omega_2 & \omega_1 & 0 \end{bmatrix} \tag{A.16}$$

With the above knowledge, the incremental form of equation (A.1) can be formulated as the following equation using the backward integration scheme,

$$\mathbf{R}^*_{n+1} = \exp(\mathbf{\Omega^*}_{n+1}\Delta t)\mathbf{R}^*_n \tag{A.17}$$

where $\exp({\boldsymbol{\Omega}^*}_{n+1}\Delta t)$ can be obtained by using equation (A.15) and the logarithmic spin tensor ${\boldsymbol{\Omega}^*}_{n+1}$ can be calculated based on equations from (A.10) to (A.13). A detailed implementation procedure for the mentioned exponential map algorithm is described in table A.1 by using the rotation angle and axis.

Table A.1: Computation algorithm for exponential map, adapted from [90].

1. Compute quaternion parameters based on $\boldsymbol{\Omega}$
   - $q_0 = \cos(||\boldsymbol{\omega}||/2)$
   - $q^* = \sin(||\boldsymbol{\omega}||/2)$
   - IF $|q^*| > \text{tol}$, $q^* = \dfrac{1}{2}\dfrac{\sin(||\boldsymbol{\omega}||/2)}{||\boldsymbol{\omega}||/2}$
     ELSE: $q^* = \dfrac{1}{2}\left[1 - ||\boldsymbol{\omega}||^2/24 + ||\boldsymbol{\omega}||^4/1920 + ...\right]$
   - $\boldsymbol{q} = q^*\boldsymbol{\omega} = \begin{bmatrix} q_1 \\ q_2 \\ q_3 \end{bmatrix}$
2. Compute the tensorial exponential $\exp(\boldsymbol{\Omega})$
   - $\exp(\boldsymbol{\Omega}) = 2\begin{bmatrix} q_0^2 + q_1^2 - \frac{1}{2} & q_1q_2 - q_3q_0 & q_1q_3 + q_2q_0 \\ q_2q_1 + q_3q_0 & q_0^2 + q_2^2 - \frac{1}{2} & q_2q_3 - q_1q_0 \\ q_3q_1 - q_2q_0 & q_3q_2 + q_1q_0 & q_0^2 + q_3^2 - \frac{1}{2} \end{bmatrix}$

APPENDIX B

SUPPLEMENTARY CALCULATION FOR CONSISTENT TANGENT STIFFNESS AND THERMAL MATRIX

The consistent tangent stiffness and thermal matrix are derived in section 3.3.3. In order to determine the explicit values for $\mathcal{L}$ and Θ during the implementation of the proposed model, the explicit expressions of the following terms $\partial_{\boldsymbol{\tau}}\Phi$, $\partial_{\xi}\Phi$, $\partial_{T}\Phi$ used in equation (4.37) are needed. First, the partial derivative of transformation function Φ with respect to stress $\boldsymbol{\tau}$ can be obtained through differentiating equation (4.30) by $\boldsymbol{\tau}$. Utilize the expression for π in equation (4.29), it obtains,

$$\partial_{\boldsymbol{\tau}}\Phi = \begin{cases} \partial_{\boldsymbol{\tau}}\pi - \partial_{\boldsymbol{\tau}}Y, \ \dot{\xi} > 0, \\ -\partial_{\boldsymbol{\tau}}\pi - \partial_{\boldsymbol{\tau}}Y, \ \dot{\xi} < 0 \end{cases} \tag{B.1}$$

where the partial derivative of the thermodynamic driving force π with respect to stress $\boldsymbol{\tau}$ is,

$$\partial_{\boldsymbol{\tau}}\pi = \boldsymbol{\Lambda} + (\partial_{\boldsymbol{\tau}}\boldsymbol{\Lambda})\boldsymbol{\tau} + \Delta\mathcal{S}\boldsymbol{\tau} + \Delta\boldsymbol{\alpha}(T - T_0) \tag{B.2}$$

and the partial derivative of critical driving force value Y with respect to stress $\boldsymbol{\tau}$ is,

$$\partial_{\boldsymbol{\tau}}Y = D\Big[\boldsymbol{\Lambda} + (\partial_{\boldsymbol{\tau}}\boldsymbol{\Lambda})\boldsymbol{\tau}\Big] \tag{B.3}$$

based on the expression for the transformation direction tensor in equation (3.40), the partial derivative of $\boldsymbol{\Lambda}$ with respect to stress $\boldsymbol{\tau}$ are provided for the forward and reverse

transformation cases as follows,

$$\partial_{\boldsymbol{\tau}}\boldsymbol{\Lambda} = \begin{cases} \dfrac{3}{2}\partial_{\boldsymbol{\tau}}H^{cur} \otimes \dfrac{\boldsymbol{\tau}^{'}}{\bar{\boldsymbol{\tau}}} + \dfrac{3}{2}H^{cur}\partial_{\boldsymbol{\tau}}\Big(\dfrac{\boldsymbol{\tau}^{'}}{\bar{\boldsymbol{\tau}}}\Big), & \dot{\xi} > 0, \\ 0, & \dot{\xi} < 0 \end{cases} \tag{B.4}$$

where the partial derivative of the term $\left(\dfrac{\boldsymbol{\tau}^{'}}{\bar{\boldsymbol{\tau}}}\right)$ with respect to stress $\boldsymbol{\tau}$ is provided in the following equation, in which $\mathbf{I}$ is the forth order identity tensor and $\mathbf{1}$ is the second order identity tensor. It can be observed that $\partial_{\boldsymbol{\tau}}\boldsymbol{\Lambda}$ only has value for the forward transformation case while it has value zero for the reverse transformation case.

$$\partial_{\boldsymbol{\tau}}\Big(\frac{\boldsymbol{\tau}^{'}}{\bar{\boldsymbol{\tau}}}\Big) = \frac{1}{\bar{\boldsymbol{\tau}}}\Big(\mathbf{I} - \frac{1}{3}\mathbf{1}\otimes\mathbf{1} - \frac{2}{3}\frac{\boldsymbol{\tau}^{'}}{\bar{\boldsymbol{\tau}}} \otimes \frac{\boldsymbol{\tau}^{'}}{\bar{\boldsymbol{\tau}}}\Big) \tag{B.5}$$

to calculate the partial derivative of the current maximum transformation strain H^{cur} with respect to stress $\boldsymbol{\tau}$, the following result can be obtained based on equation (4.19),

$$\partial_{\boldsymbol{\tau}}H^{cur} = \frac{3}{2}H^{max}k_t e^{-k_t\bar{\boldsymbol{\tau}}}\frac{\boldsymbol{\tau}^{'}}{\bar{\boldsymbol{\tau}}} \tag{B.6}$$

Follow the similar procedure to obtain $\partial_{\boldsymbol{\tau}}\Phi$, the partial derivative of the transformation function Φ with respect to martensitic volume fraction ξ, and the partial derivative of the transformation function Φ with respect to temperature T can be calculated as follows,

$$\partial_{\xi}\Phi = \begin{cases} \dfrac{1}{2}a_1\Big[n_1\xi^{n_1-1} + n_2(1-\xi)^{n_2-1}\Big], & \dot{\xi} > 0, \\ -\dfrac{1}{2}a_2\Big[n_3\xi^{n_3-1} + n_4(1-\xi)^{n_4-1}\Big], & \dot{\xi} < 0 \end{cases} \tag{B.7}$$

$$\partial_T \Phi = \begin{cases} \boldsymbol{\tau} : \Delta\boldsymbol{\alpha} + \rho_0 \Delta c \ln(\frac{T}{T_0}) + \rho_0 \Delta s_0, \quad \dot{\xi} > 0, \\ -\Big[\boldsymbol{\tau} : \Delta\boldsymbol{\alpha} + \rho_0 \Delta c \ln(\frac{T}{T_0}) + \rho_0 \Delta s_0\Big], \ \ \dot{\xi} < 0 \end{cases} \tag{B.8}$$